Norwegian University
of Life Sciences

Master's Thesis 2016 30 ECTS
Department of Mathematical Sciences and Technology

Defect Related Radiative Recombination in Mono-like Crystalline Silicon Wafers

Simen Bergan
Environmental Physics and Renewable Energy

If I have seen further,

it is by standing on shoulders of Giants.

Sir Isaac Newton

Dedicated to

my father, Svein Bergan, who battles the MS disease every day

my mother, Nora Olaug Bergan, owner of the kindest heart

and my friend

Peter Holum Normann

a bright star, too soon your light was darkened.

Abstract

The aim of this work was to investigate defect related luminescence emission in four mono-like silicon wafers. The seed-assisted silicon ingot is built by six Czochralski silicon slabs, with nine seed junctions. The discovered emission signals are due to Shockley-Read-Hall recombination. Each wafer originates from a mono-like silicon ingot grown at the Norwegian University of Science and Technology (NTNU), Trondheim. The master thesis work was conducted at the Norwegian University of Life Sciences (NMBU), Ås.

Hyperspectral imaging has been used in multiple branches like medicine, industry and military purposes. In this investigation hyperspectral imaging is conducted on mono-like silicon wafers. Seed-assisted grown mono-like silicon are produced with the goal of increasing wafer efficiency at lesser cost. Spectrally resolved photoluminescence (SPL) has been used together with multivariate data analysis. This is a non-destructive method to examine defect related luminescence in each mono-like wafers. Each wafer was cooled to 88±2 K before illuminated with an 810 nm laser. The photoluminescence emission from each wafer was captured by an HgCdTe hyperspectral camera.

The individual D1-D4 and band to band PL emission signals were extracted with Multivariate Curve Resolution (MCR) algorithm and found in the seed junctions. It has also been found three other PL emission signals, either in the seed junctions, or from parasitic crystals penetrating into the main wafer ingot. The D07 PL emission signal is restricted to the parasitic crystals and can be related to interstitial iron (Fe_i). A signal at 0.846±0.01 eV, known as D5, has been found as a shoulder of D1 and D2 PL emission signals. These three PL signals have been related to dislocations with oxygen impurities in other studies. A new signal denoted D09 with the energy 0.904±0.01 eV is discovered and is growing in intensity with increased height of the ingot. The signal seems to be centered in the seed junctions and has not been mentioned before.

The D1 PL signal is strong in the A-108 wafer, then decreasing in strength with increasing height. This seems to strengthen the theory of the D1 PL emission signal related to oxygen. The D2 PL signal on the other hand increases in intesity with increased ingot height, and contredicts the oxygen theory.

D3/D4 PL emission signals are found in the seed junctions and can be related to the same spatial position. The PL emission signals increases with ingot height and strengthen the suggestion that D3/D4 PL signals originates from iron-boron (FeB) complexes. The high intensity PL emission signal known as VID3 has not been found in this work.

A tail on the D1 PL signal found at 0.95 eV and 1.00 eV have been discussed in other studies and can be explained by hydrogen-silicon (H-Si) bond.

One parasitic crystal has been found with multiple impurities. That crystal may have another grain boundary and dislocation number than the parasitic crystals with only the D07 PL signal.

Comparing this work with the work done by Ekstrøm et al. [1] has discovered some similarities. It mentions different tilt and misorientation angles in each seed junction. The investigation concluded that misorientation angles in the seed crystal junctions produced tilt around one or several axis, and would play a major part in the bulk lifetime. Comparing to the current work has found that low misorientation angle around the X-axis seems to produce none or weak defect related PL emission signals. Misorientation around Z-axis seems to produce more defect related luminescence. While misorientation around multiple axis seems to create chaotic junctions with high defect related luminescence. The explanation can be the number of vacancies ready for impurities are higher in multiple axis tilts than one single axis tilt.

The conclusion is that the combined strength of SPL and MCR as a method to investigate mono-like silicon wafers has been used with success. The known D1-D4, D5 and D07 PL emission signals was found alongside a new PL emission signal at 0.904 ± 0.01 eV. The PL emission signals are not clearer than the emission signals found in mc-Si wafers, however, the D07 signal has been found separated from the rest of the other DRL signals and this can be a helpful in further experiments. The different PL emission signals are found to vary greatly throughout the ingot and logic answers can be made to explain the results based on known literature. Hyperspectral imaging and Multivariate curve resolution can strengthen and contribute to an increased quality of seed assisted mono-like wafers.

Sammendrag

I denne masteroppgaven har fire "as cut" skiver fra en mono-lik silisiumkrystall blitt undersøkt. Frø assistert mono-lik silisium ingot er en produksjonsmetode for å skape høyeffektivitetsskiver med den rimlige multikrystallinske størkningsprosessen. Prosessen er under utvikling, med mål om å kunne forbedre solcellene i et sluttprodukt. Denne masteroppgaven går ut på å avdekke defekter i disse skivene både i romlig og spektral posisjon.

For å kunne finne defekter i silisiumskivene registreres fotonutslippet til eksiterte elektroner som rekombinerer etter Shockley-Read-Hall metoden. I dette eksperimentet skjer dette ved å la en 810 nm laser belyse hver av de nedkjølte skivene. Skivene er nedkjølt til 88±2 K med flytende nitrogen. Fotonene fra de eksiterte elektronene registreres og fordeles til sine spektrale områder i et HgCdTe hyperspektralt kamera. For å kunne hente ut de interessante defektrelaterte spektrumene brukes Matlab og et statistisk verktøy som heter Multivariate curve resolution (MCR).

I denne oppgaven har alle de fire kjente emisjonslinjene D1, D2, D3 og D4 blitt funnet sammen med bånd til bånd emisjonslinjen. Disse defektrelaterte emisjonslinjene er bare funnet i frøkrystallgrensene, foruten ett sted: En parasittisk krystall nær en av sidekantene. I tillegg er det funnet tre andre emisjonslinjer. Det ene er kalt D5 som ser ut til være en skulder av det sterkere D2 emisjonlinjen med energien 0.846±0.01 eV. Det andre signalet er kalt D09 med energien 0.904±0.01 eV og er funnet sentrert i krystallgrensene. Dette signalet ser ut til utvikle seg fra D2 signalet i A-108 skiven og videre fram til et eget signal i A-45 skiven. Det tredje signalet er et signal nylig publisert som D07 og er bare funnet i parasittiske krystaller som virker å gro inn fra digelkantene. Denne emisjonslinjen kan stamme fra interstitielt jern (Fe_i).

D1 emisjonslinjen har høyest intensitet i nær bunn av ingoten og minsker gradvis i styrke med økende ingot høyde. D2 emisjonslinjen derimot ser ut til styrke seg mot toppen av ingoten og er sterkest i A-45 skiven. Både D1, D2 og D5 er betegnet i litteraturen som å kunne relateres til oksygen. Ut i fra oppførselen til D2 emisjonslinjen, motsier resultatet oksygen teorien, mens D1 og D5 ser ut til forsterke den samme teorien.

D3/D4 emisjonslinjene er funnet i bare ett av frøkrystallgrensene i A-108 skiven. Derimot, i de resterende tre skivene er signalet tilstede i alle frøgrensene. MCR algoritmen betrakter dette signalet som ett signal og styrker ideen om at D3/D4 har samme romlig opprinnelse. D4 emisjonslinjen er nevnt å oppstå fra jern utfellinger fra smeltediglen og ovnen, hvor D3 emisjonslinjen kan være en fononreplica av D4. I denne undersøkelsen øker D3/D4 emisjonslinjene i intensitet med økt ingot høyde. Metallutfellingsteorien ser ut til å holde og kan forklares med feller i båndgapet fra jern-bor (Feb) komplekser. Et signal som er diskutert i litteraturen er en emisjonslinje kalt VID3. Dette signalet er ikke funnet noen steder i noen av skivene undersøkt.

I D1 emisjonslinjen er det funnet en hale som har to toppunkt i området 0.95 eV og 1.00 eV. Disse toppunktene er sett i andre studier av tynnfilm silisium og kan forklares med hydrogen-silisium feller i båndgapet.

I en undersøkelse gjort av Ekstrøm et al. [1] på samme ingot ble det konkludert med at misorienterings- vinkler rundt en eller flere akser hadde stor innvirkning på antall dislokasjoner og levetid over frøkrystallgrensene. I denne undersøkelsen har den konklusjonen blitt undersøkt for å se om mulig korrelasjon kan bekreftes. Når det gjelder emisjonslinjene over frøkrystallgrenser er det funnet klar korrelasjon med misorienteringsvinkel om en eller flere akser. Der det er liten misorientering rundt X-aksen er det ingen eller lite defektrelaterte emisjonslinjer. Ved misorientering om Z-aksen er det mer defektrelatert emisjonslinjer. Ved misorientering i flere akser er det funnet kaotiske frøkrystallgrenser med sterke defektrelaterte emisjonslinjer, selv om vinklene er små. En forklaring på dette er at det er flere ledige områder for urenheter å feste seg i ved misorientering i flere dimensjoner.

Det konkluderes med at et samarbeid med SPL og MCR som en metode for forbedre mono-lik silisium skiver har blitt brukt med suksess. De kjente D1-D4, D5 og D07 emisjonslinjene er funnet sammen med en ny emisjonslinje ved 0.904±0.01 eV. Emisjonslinjene oppfattes ikke klarere enn emisjonslinjer i mc-Si, men D07 emisjonslinjen er funnet separert fra de andre emisjonslinjene. Dette kan være til god hjelp i framtidig forskning. Emisjonslinjene er funnet å variere mye mellom høyden til ingoten og logiske slutninger kan trekkes for å forklare hendelsene basert på kjent litteratur. Hyperspektral bildebehandling sammen med MCR kan styrke og bidra til en økt kvalitet på frø assistert mono-lik silisium skiver.

Contents

Abstract iii

Sammendrag v

List of Figures x

Acknowledgments xi

Abbreviations xiv

1 Introduction 1

2 Theory 3

2.1 Wafer technology . . . 3
2.1.1 Silicon crystal structure . . . 3
2.1.2 Doping . . . 4
2.1.3 Direct and indirect bandgap . . . 5
2.1.4 Mono-like silicon production technology . . . 6
2.2 Recombination methods . . . 7
2.2.1 Direct radiative band to band recombination . . . 7
2.2.2 Shockley-Read-Hall recombination . . . 8
2.2.3 Auger recombination . . . 11
2.2.4 Surface recombination . . . 12
2.3 Defects in mono-like silicon . . . 13
2.3.1 Point defects . . . 13
2.3.2 Dislocations and grain boundaries . . . 14
2.3.3 Defect related luminescence . . . 15
2.4 Diffusion . . . 16
2.5 Hyperspectral imaging . . . 17
2.6 Multivariate curve resolution . . . 18

3 **Experimental and experimental setup** **21**
3.1 Mono-like silicon ingot and its wafers . . . 22
3.2 Cryogenic container and thermometer . . . 23
3.3 Laser . . . 23
3.4 Hyperspectral camera and low-pass filter . . . 23
3.5 Data processing . . . 23

4 **Results and discussions** **25**
4.1 Experimental results from MCR . . . 25
4.1.1 MCR results of SPL of wafers A-108 through to A-45. . . . 25
4.1.1.1 MCR A-108 . . . 26
4.1.1.2 MCR A-80 . . . 26
4.1.1.3 MCR A-78 . . . 27
4.1.1.4 MCR A-45 . . . 28
4.1.2 Section disccussion . . . 28
4.2 Experimental Matlab results . . . 30
4.2.1 Matlab results from SPL of wafers from A-108 through to A-45 . . . 30
4.2.2 Section discussion . . . 35
4.3 Investigation of the mono-seed junctions. . . . 37
4.3.1 A-108 seed junctions . . . 37
4.3.2 A-78 seed junctions . . . 42
4.3.3 A-45 seed junctions . . . 47
4.3.4 Section discussion . . . 58
4.4 D07 PL emission signal . . . 60
4.4.1 Establishment of rogue crystals from the crucible wall and D07 PL emission signal . . . 60
4.4.2 Section discussion . . . 65
4.5 D5 and D09 PL emission signals . . . 66
4.5.1 Section discussion . . . 69
4.6 Error found in MCR and laser intensity . . . 69
4.6.1 Laser intensity . . . 69
4.6.2 Vacancy in MCR score image . . . 70

5 **Conclusion** **73**

6 **Suggestions for future work** **75**

Bibliography **77**

A **MCR loads with all 17 components, 20 components and 5 components** **81**

B **Translation from image spectrum to electronvolt** **85**

C **A-108 to A-45 score images with locked A-45 BB intensity** **89**

D **Tables of DRL evolving through the mono-like silicon crystal and NTNU junction characteristics.** **95**

List of Figures

2.1 Silicon crystal structure 4
2.2 Shift in Fermi level in p-type silicon 5
2.3 Direct and indirect bandgaps 6
2.4 Radiative recombination 7
2.5 Shockley-Read-Hall recombination, bonding and band model 9
2.6 SHR recombination for donor- and acceptor-type 9
2.7 Auger recombination 12
2.8 Surface recombination 13
2.9 Point Defect 13
2.10 Edge dislocation 14
2.11 Screw dislocation 14
2.12 Tilt angle with misorientation 15
2.13 Spectral components 17
2.14 Hyperspectral camera 18
2.15 MCR-ALS algorithm 19

3.1 Schematic representation of the experimental setup 21
3.2 Mono-like wafer 22
3.3 Mono-like ingot 22

4.1 Plots of integrated dataset in Matlab 26
4.2 MCR load plots from A-108 to A-45 27
4.3 Band to band gap emission signal from Matlab of wafer A-108 to A-45 31
4.4 D07 PL emission signal from Matlab of wafer A-108 to A-45 32
4.5 Seed junctions 33
4.6 D1 PL emission signal from Matlab of wafer A-108 to A-45 33
4.7 D2 PL emission signal from Matlab of wafer A-108 to A-45 34
4.8 D3 PL emission signal from Matlab of wafer A-108 to A-45 35
4.9 D4 PL emission signal from Matlab of wafer A-108 to A-45 36
4.10 Seed junctions and their numbers 37
4.11 A-108 seed junction 1.1 38
4.12 A-108 seed junctions 1.1-1.3 39
4.13 A-108 seed junctions 1.4-1.6 40
4.14 A-108 seed junctions 2.Y 41

4.15 A-108 seed junction 2.1 and 2.2 with rosettes 42
4.16 A-78 seed junctions 1.1-1.3 43
4.17 A-78 seed junctions 1.4-1.6 44
4.18 A-78 seed junction 2.Y 45
4.19 A-78 seed junction 2.1 with rosettes 46
4.20 A-78 seed junction 2.2 with rosettes 47
4.21 A-45 seed junction 1.1 48
4.22 A-45 seed junction 1.2 49
4.23 A-45 seed junction 1.3 50
4.24 A-45 seed junction 1.4 51
4.25 A-45 seed junction 1.5 52
4.26 A-45 seed junction 1.6 53
4.27 A-45 seed junction 2.1 54
4.28 A-45 seed junction 2.2 55
4.29 A-45 seed junction 2.3 56
4.30 A-45 seed junction 2.1 with rosettes 57
4.31 A-45 seed junction 2.2 with rosettes 58
4.32 D07 seen first time in A-45 60
4.33 Rogue crystal 1 with D07 61
4.34 Rogue crystal 2 with D07 62
4.35 Rogue crystal 3 with D07 63
4.36 Rogue crystals inside junction 1.6 in wafer A-45 64
4.37 Rogue crystals inside junction 1.6 in wafer A-108 64
4.38 Rogue crystals inside junction 1.6 in wafer A-108 65
4.39 D09 PL emission signal 66
4.40 D09 signal 67
4.41 D5 signal 68
4.42 Laser difference in a image of A-45 wafer 70
4.43 Vacancy in MCR score image 70

A.1 A-108 - A-45 MCR with 17 components 81
A.2 A-108 - A-45 MCR with 20 components 82
A.3 A-108 - A-45 MCR with 5 components 83

C.1 BB in A-108 to A-45 with equal intensity 89
C.2 D07 in A-108 to A-45 with equal intensity 90
C.3 D1 in A-108 to A-45 with equal intensity 91
C.4 D2 in A-108 to A-45 with equal intensity 92
C.5 D3 in A-108 to A-45 with equal intensity 93
C.6 D4 in A-108 to A-45 with equal intensity 94

Acknowledgments

I am grateful for being allowed to conduct such an interesting thesis and be a part of a cooperation between two universities. Solar energy has interested me for some years now and is one of the reasons I started this university degree at adult age. To be a part of an activ research field has been both demanding and highly appreciated. I have grown a lot in the last four months.

My thanks and regards to Marisa Di Sabatino Lundberg and Kai Erik Ekstrøm at NTNU, our mail correspondence has been greatly rewarding. Many thanks to my roommates Tobias Brekke and Fredrik Aulie, we have shared a lot of ups and downs these last couple of months. It is always a pleasure to wake up to bathroom singing Tobias. To Turid Torheim and Knut Kvaal, you always gave me helpful hints. Since I am not the best writer in the world I am greatly thankful of the help Heidi S. Nygård and Espen Steinseth Hamborg have done with the proof reading these last couple of weeks. Thank you Espen for moving to Ås at the right time.

My dear supervisors Espen Olsen and Ingunn Burud, I am greatful that you took a chance on me as your master student. The physics and MCR discussions, as well as your guidence have been much needed and have played an importent part in getting me to where I am today. Then last, but certainly not least my supervisor Torbjørn Mehl. I would not have done this without you and your general guidence, Matlab codes and knowledge. Sharing a semester at the University of Oslo has also been greatly appreciated. The best of luck to all you guys, it was a blast.

Simen Bergan
Norwegian University of Life Science, May 2016.

Abbreviations

Cz-Si	Monocrystalline silicon
mc-Si	Multicrystalline silicon
NMBU	Norwegian University of Life Sciences
NTNU	Norwegian University of Science and Technology
SPL	Spectrally resolved photoluminescence
DRL	Defect related luminescence
BB	Band-to-band
SRH	Shockley-Read-Hall
MCR	Multivariate Curve Resolution
Si	Silicon
ALS	Alternating least squares
LID	Light induced degradation

Chapter 1

Introduction

Silicon wafers have for some time been the backbone of solar cell production with a market share of 80-90 percent of the world's total solar cell module demand [2] [3]. The manufacture of crystalized silicon ingots is divided into two production techniques; monocrystalline silicon (Cz-Si), which is produced by Czochralski process (Cz) [4]. The other is multicrystalline silicon (mc-Si), which is produced by directional solidification [5]. By far, mc-Si has the highest marked share in 2011 with over 80 % of the total solar energy market [2].

The production technique for mc-Si wafers is well known by the industry and the method is less expensive than the Cz process [3] [6]. The main challenge with the directional solidification method is lesser efficiency, in the final solar cell product than the Cz-Si solar cell. The efficiency challenge is mainly located in the solidification process itself. As the crystal solidifies in the crucible, small grains of silicon crystals with different shapes occur through the entire silicon ingot [7] [8]. The different shapes and growth directions of the small crystals inside the ingot are perceived as defects. The high amount of defects in the mc-Si results in a lower efficiency that of the Cz-Si ingot. In the Cz process the silicon crystal grows as one unit making the resulting ingot nearly free of grain boundaries, which will again results in fewer defects.

In the production of mono-like silicon ingots the manufactures combine a few Cz-Si seed crystals with a given length and height placed at the bottom of the crucible. Silicon is then added to the crucible and heated up to its melting point. At the point where the Cz-Si is solid, with the rest of the silicon melted, the heat is turned off and the directional solidification starts. The manufacturer can with this method control the orientation of the solidification after the seed crystal orientation. This technique has the aim of creating better silicon wafers for solar cell production. Mono-like silicon was expected to quickly be preferred as a wafer material, however, challenges such as high amounts of impurities and parasitic crystals were found [9].

This thesis will examine four "as cut" wafers measuring 15.6 cm $\times$ 15.6 cm. These wafers are cut from a mono-like silicon ingot manufactured at the Norwegian University of Science and Technology (NTNU) in Trondheim. The mono-like wafers are cut from different areas throughout the silicon ingot, with number A-108 near the bottom to the A-45 near the top of the ingot. In the experiment done by NTNU, growth of the mono-like crystal in $< 110 >$ direction was successfully controlled [1]. After cutting the ingot into wafers a investigation of low-lifetime occured. Low-lifetime areas was expected and found to be located around the seed junctions [1]. By growing the Si crystal with different gaps between the Cz-Si seed crystals, cluster defects were found with varying properties [1]. Dislocations were found to establish clusters in the $< 111 >$ orientation [1].

In this thesis spectrally resolved photoluminescence (SPL) is used for the first time to

investigate mono-like silicon wafers. The experimental part was performed at the hyperspectral laboratory at the Norwegian University of Life Sciences (NMBU). With the SPL method, defect related luminescence (DRL) and band-to-band (BB) luminescence of radiative Shockley-Read-Hall (SRH) recombination were examined. The SPL method is a non-destructive technique to investigate crystal silicon wafers and has been used with success regarding mc-Si wafers and solar cells [10]. After the SPL method was performed on the mono-like wafers, Multivariate Curve Resolution (MCR) was used to visualize and extract the different luminescence emissions from the mono-like wafer [11]. Three hypotheses are made; First, that the combined strength of SPL and MCR is a importent tool in classifying DRL in mono-like wafers. Second, the emission signal will be clearer visualized in mono-like silicon wafers than mc-Si wafers. This is based on the assumption where orientation of the solidification is successfully controlled. Three, it is expected to find difference in the luminescence emissions throughout the ingot varying from the bottom to the top, based on assumptions of difference in impurities and dislocations.

Chapter 2

Theory

2.1 Wafer technology

In this work four p-type "as cut" wafers are examined and this section will describe mono-like silicon production with the general doping and bandgaps. The physics of solar cells to pn-junctions, solar cell parameters, losses and efficiency limits, designing and fabricating solar cells will not be addressed and the reader is encouraged to look elswhere [2, 12].

2.1.1 Silicon crystal structure

Silicon (Si) has atomic number 14, with four electrons in the third shell called valence electrons. Si atoms in a silicon crystal lattice are bonded with covalent bonds formed by two electrons, meaning a Si atom can be bonded by four other Si atoms [12]. In figure 2.1, a structure part of a silicon crystal is shown. At 0 K all valence electrons lock together in covalent bands and no free electrons are available. At $T > 0$, the chance of covalent bonds breaking increases and electrons can move around in the lattice leaving behind vacancies called holes. Other valence electrons can recombine with the free holes. It seems that the holes are moving in the opposite direction as the electrons, now both electrons and holes are free charge carriers [12]. This is an intrinsic property, meaning that it cannot be avoided. In intrinsic silicon the concentration of holes p equals the concentration of electrons n. At 300 K $n = p = 1.5 * 10^{-3}$cm, which is called the intrinsic carrier concentration n_i at this temperature [12].

The mono-like Si ingot, elaborated further in section 2.1.4, uses monocrystalline silicon as seeds. A brief look into the two most common types of silicon wafers are needed. These two types is multicrystalline silicon (mc-Si), also called polycrystalline silicon and monocrystalline silicon (Cz-Si), also called Czochralski silicon, after the production process [4, 12, 13]. The mc-Si ingot is manufactured by a solidification process where the pure silicon feedstock is melted with the dopants in a crucible and left to solidify without any handling [12]. What characterizes this method is that the low finacial manufacturing costs and low efficiency parts, than the Cz-Si wafers. The monocrystalline Si ingot is manufactured by the Czochralski process, where a seed crystal is lowered into melted silicon feedstock. After the seed has interacted with the melted Si, the seed is hoisted slowly up from the melted feedstock with a rotating motion as the Si solidifies [12]. The Czochralski process is a more expensive manufacturing process, giving higher efficiency wafers than the mc-Si wafers. Note that the Si feedstock used in both processes has to be extremely pure, with a purity of 99.9999 % [12].

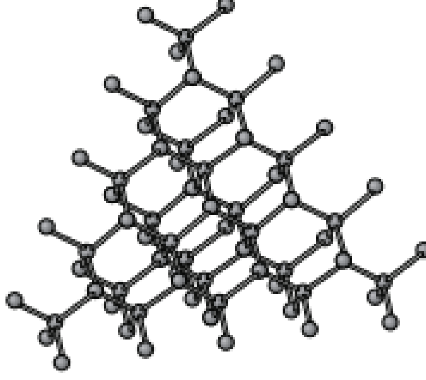

Figure 2.1: A part of a silicon crystal structure [12].

2.1.2 Doping

Doping a lattice means that the silicon (Si) crystal is manipulated with impurities. Doping the pure Si lattice with boron, which is a group three atom with three valence electrons, creates an acceptor semiconductor denoted N_A. If the Si lattice is doped with a group five atom as phosphorus with five valence electrons, a donor semiconductor is created denoted N_D. Meaning the lattice either readily accept a free electron N_A from or discharges an electron N_D to the neighbouring Si-Si bond to fill the valence bond [12]. The doped material maintain its charge neutrality because the bonded sites where the impurity atoms occupy becomes charged. The acceptor atoms are now negatively ionized and the donor atoms are positive ionized. Two types of semiconductor are now established, the p-type with excess holes and n-type with excess electrons. Since the p-type semiconductor has excess holes, they are the majority carriers and the electrons are here the minority carriers. The n-type on the other hand has electrons as majority carriers and holes as minority carriers, this will again control the electrical conductivity [12].

In this thesis a boron doped, p-type mono-like Si ingot has been investigated. At room temperature the energy in the lattice is sufficent to break free electrons that can recombine with holes caused by the boron doping. At equilibrium, assuming the semiconductor is uniformly doped, a carrier and dopant concentration relationship can be established [12]. Another assumption is that at room temperature the dopant atoms are ionized and the local charge density ρ inside a semiconductor is given by

$$\rho = q(p + N_D^+ - n - N_A^-) \tag{2.1}$$

where q is the elementary charge, n and p are the electrons and holes, N_D^+ and N_A^- are the density of the ionized donor and acceptor atoms, respectively. N_D^+ and N_A^- are also an indication of the electron and hole concentration. At equilibrium there is charge neutrality and equation 2.1 can be given as

$$p + N_D^+ - n - N_A^- = 0 \tag{2.2}$$

Since the thermal energy at room temperature is sufficient to ionize near all dopant atoms, it can be assumed that $N_D^+ \approx N_D$ and $N_A^- \approx N_A$ so equation 2.2 is given by

$$p + N_D - n - N_A = 0 \tag{2.3}$$

Since this experiment investigates a p-type semiconductor and the donor atoms are equal to zero, and equation 2.3 is further reduced to

$$p - n - N_A = 0 \tag{2.4}$$

Assuming the $N_A \approx N_A^- \approx p$ it is expected that the number of electrons are less than the number of holes. The concentration of electrons in a p-type is given by

$$n = \frac{n_i^2}{p} \approx \frac{n_i^2}{N_A} \ll p \tag{2.5}$$

Doping the silicon lattice allows levels in the forbidden bandgap E_G. The acceptor atom will be located near the valence band E_A because of the excess holes. The Fermi level E_F will also be influenced and pulled closer to the valence band E_V, as seen in figure 2.2 [12].

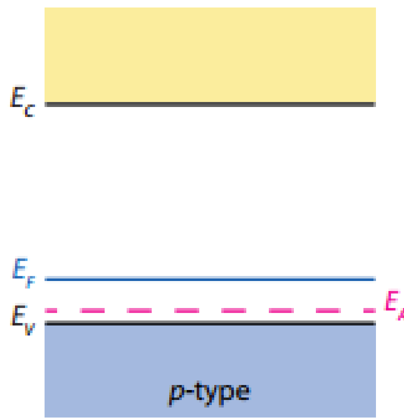

Figure 2.2: A shift in the Fermi energy E_F (blue) can be measured if the acceptor doping establish an acceptor energy level E_A (purple) just outside the valence band $E_V(black)$ [12].

After the semiconductor is doped to a p-type, the new Fermi level E_F position can be determined and given by

$$E_F - E_V = k_B T ln \frac{N_V}{N_A} \tag{2.6}$$

where E_V is the valence band, k_B is the boltzmann's constant, T is the temperature, N_V is the effective densities of the valence band states and N_A is the densities of the ionized acceptor atoms.

2.1.3 Direct and indirect bandgap

A semiconductor has either a direct or indirect bandgap, and is hence called a direct semiconductor or an indirect semiconductor. As seen in figure 2.3 the direct bandgap apex of the valence band E_V is aligned with the inverted apex of the conduction band E_C. A photon can be directly exited from the valence band to the conduction band. An indirect semiconductor such as silicon, has no alignment between the valence band apex and the inverted conduction band apex. A photon is a high energy, and low momentum particle. To reach the conduction band the electron interacts with a phonon. The phonon is a low energy, but high momentum particle. A phonon is released from a vibrating crystal lattice and is the quantified mode of the

lattice vibration. Since silicon is an indirect semiconductor, the electron needs both a photon with enough energy to excite it to the lowest conduction band and a phonon for momentum to reach it. This is seen in the dispersion diagram in figure 2.3.

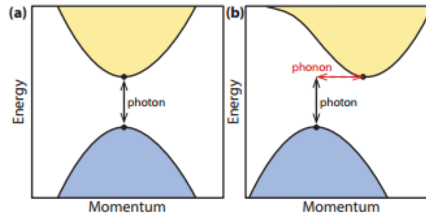

Figure 2.3: a) a direct bandgap where the electron only needs a photon, b) a indirect bandgap where the electron needs both a photon and a electron [12].

2.1.4 Mono-like silicon production technology

In 2014 the work of Guerrero et al. [14] presented pros and cons of mono-like silicon. The paper addressed several topics on the state of mono-like technology and further challenges the manufactures should pursue in the future.

The aim of mono-like silicon products is to achieve near Cz-Si efficiency with mc-Si solidification process, using mono seed crystals with a certain direction at the bottom of the crucible. The melted silicon feedstock can solidify after the direction of the seeds, thus achieving a more cost effective product. The mono-seed direction was normally tested in the $< 100 >$ orientation, later as given by Ekstrøm et al. [1], $< 110 >$ was attempted [14]. A higher oxygen impurity level was expected to establish in mono-like silicon than mc-Si, since Cz-Si was used as seed base. Another topic was the challenge of controlling the Cz-Si seeds from melting with the rest of the silicon feedstock. A solution to the seed melting was to control the crucible bottom with external cooling, while the rest of the crucible was heated [14]. Optimized furnace, named software approach and/or adapting the graphite hot zone, named the hardware approach, was mentioned in the paper by Guerrero et al. [14] as solutions to overcome these challenges. It was also noticed that placing the mono seeds in the right way and preparing the surfaces of the seeds could be an important issue to achieve a proper end result [14] this was confirmed by Ekstrøm et al. [1].

When investigating the mono-like ingots after solidification, undesirable traits of low-lifetime and low performance were detected near the top and bottom of the ingot [14]. Multiple degradation situations occured when recycling the seeds was conducted; lifetime degradation near the crucible base, curved melting in front of the seed, low-lifetime near the top of the seed and low-lifetime seed junctions. These problems were explained by defects due to impurities from the crucible and thermal stress leading to networks of dislocations [14].

A number of suggestions for further research is mentioned in the paper by Guerrero et al. [14]; control of melting and best possible surface preparation, obtained control of thermal fluxes on the sides avoiding stress, using several small mono-seed crystals, using crucibles with low iron content, different seed orientation and optimization of texture processes at solar cell level. The work by Guerrero et al. [14] express the need to implement techniques for mass production of Cz-Si more cost effective, recycling seed crystals and enhance and specialize the crucible and improved furnace technology are topics mentioned with a need to be addressed in the future .

Gu et al. [9] investigated and found that using small seed crystals and alkaline texturing the efficiency increased to 17.3 %. This was considered 1 % better than mc-Si. Lower Light induced

degradation (LID) was also achieved, but parasitic crystals from the side of the crucible was still mentioned as a problem.

Recently a paper from Ekstrøm et al. [1] discussed the solidifacation of a p-type, mono-like silicon ingot in $< 110 >$ direction where less rooftop growth was found. Investigation on the seed crystal junctions was conducted and the current work is in collaboration with NTNU.

2.2 Recombination methods

In this section different recombination methods will be addressed. Mainly two types are found in silicon semiconductor, intrinsic and extrinsic recombinations. Intrinsic recombination occurs naturally and cannot be avoided. Extrinsic recombination can occur in crystal defects or in the lattice, where impurities have entered and function as traps in the forbidden bandgap [12, 15].

2.2.1 Direct radiative band to band recombination

The radiative recombination is an intrinsic trait of a direct bandgap semiconductor. One hole from the valence band and one electron from the conduction band recombine. At the moment the electron-hole pair recombine a photon is emitted. As given, this is an intrinsic trait in the direct bandgap. As phonons freezes out, the radiative recombination in indirect bandgaps can be investigated. The direct recombination is shown in figure 2.4.

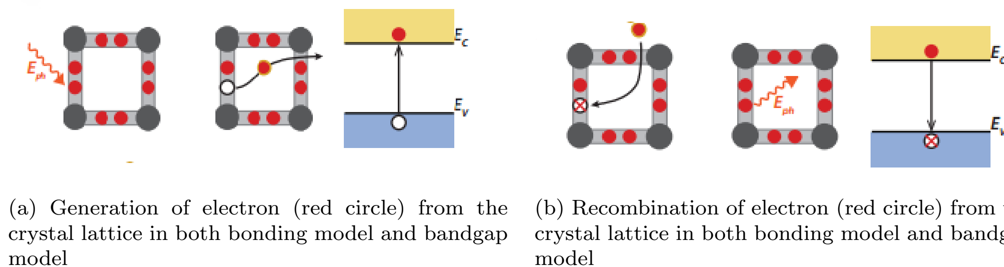

(a) Generation of electron (red circle) from the crystal lattice in both bonding model and bandgap model

(b) Recombination of electron (red circle) from the crystal lattice in both bonding model and bandgap model

Figure 2.4: a) A photon with energy E_{ph} excites an electron (red) to the conduction band. b) The electron (red) recombines with a hole (red cross) back to the valence band emitting a photon [12].

At thermal equilibrium the concentrations of electrons n and holes p must be equal to the intrinsic carrier concentration squared n_i^2, as given by

$$np = n_i^2 \tag{2.7}$$

It can be assumed that the recombination and generation rates are equal. The recombination at thermal equilibrium is given by

$$G_{th} = R_{th} = \beta n_0 p_0 \tag{2.8}$$

where G_{th} is the thermal generation of electron-hole pairs, R_{th} is the thermal recombination rate, β is a proportionality factor, n_0 and p_0 are the electron and hole equilibrium concentrations, respectively. When the sample is illuminated, a constant generation rate G_L will be present, more free electrons and holes will be available and the recombination activity will increase. Reaching

a steady state situation the total recombination R^* and generation G of electrons and holes are given as

$$R^* = \beta np = \beta(n_0 + \Delta n)(p_0 + \Delta p) \tag{2.9}$$

and

$$G = G_{th} + G_L \tag{2.10}$$

where G_L is the constant generation rate, R_{th} is the thermal recombination rate, Δn and Δp are the excess electrons and holes, n and p are the free electrons and holes, β is a proportionality factor, n_0 and p_0 are the electron and hole equilibrium concentrations, respectively, Δn and Δp are given by

$$\Delta n = n - n_0 \tag{2.11}$$

$$\Delta p = p - p_0 \tag{2.12}$$

In steady state R^* equals G and net recombination is found by

$$R_d = R^* - G_{th} = G_L \tag{2.13}$$

where R_d is the net radiative recombination rate. By substitution, the constant generation rate G_L is given by

$$G_L = R_d = \beta(np - n_0p_0) \tag{2.14}$$

Since the experiment is done with a p-type wafer assuming low level injection $\Delta p \ll p$ and $n \ll p$ the net radiation recombination rate is given by

$$R_d \approx \beta p_0(n - n_0) = \frac{n - n_0}{\tau_{nd}} \tag{2.15}$$

where τ_{nd} is the electron lifetime and is related to

$$\tau_{nd} = \frac{1}{\beta p_0} \tag{2.16}$$

If the generation and recombination are occurring at more than one place at the same time, the total generation and recombination can be summed up. This applies for the total lifetime as well.

2.2.2 Shockley-Read-Hall recombination

In 1952 two papers published by Shockley et al. [16] and Hall et al. [15] stated that recombinations could occur by traps in the forbidden band gap. Shockley-Read-Hall (SRH) recombination is an extrinsic property occurring from an impurity atom or lattice defect in the silicon lattice, where the number of impurities $\ll$ acceptor or donor atoms. Investigating the band gap, different impurities or lattice defects cause different trap-states, which suddenly are allowed energy levels E_T inside the forbidden band gap of the silicon crystal. A donor-type trap is neutral with an electron or positive charged without an electron, as for the acceptor-type trap, it is negative charged with an electron or neutral without an electron. The SRH recombination is shown in figures 2.5 and 2.6.

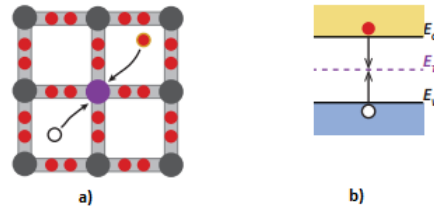

Figure 2.5: a) a electron (red) or a hole (white) recombinate at the trap state (purple). b) the same is shown in a energy band model [12].

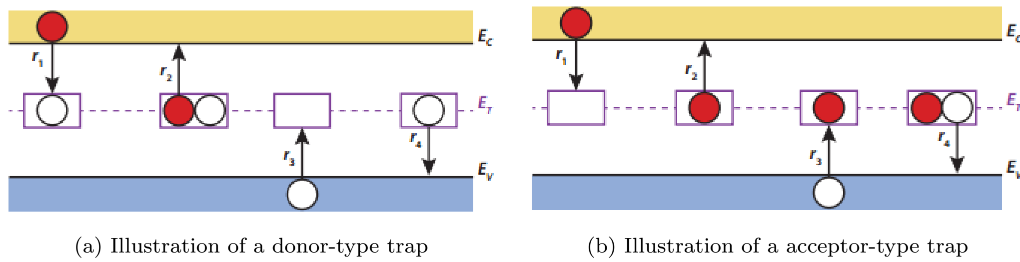

(a) Illustration of a donor-type trap

(b) Illustration of a acceptor-type trap

Figure 2.6: a) the electron (red) recombine with a hole (white) in the donor-trap (purple square) (r_1), an electron exites back to the conduction band E_C (r_2), a hole is captured by a trap from valence band E_V (r_3), a hole falls back to the valence band E_V (r_4) b) the same occures, but this time in a acceptor-type [12].

The thermal velocity related to both holes and electrons is the average velocity of the electrons and holes due to thermal movement. In silicon the value is 10^7 cm/s and is assumed to be identical for holes and electrons. In SRH recombination, Fermi-Dirac statistics states that in a semiconductor at thermal equilibrium, the carrier distribution depends on the chemical potential of the carriers represented as the Fermi level E_F. Note, in non-equilibrium, illuminated or applied by a forward bias, the holes and electrons tend to a quasi-Fermi energy level, E_{Fn} and E_{Fp} respectively. The general expressions for free electrons and holes concentration denoted n and p are both at equilibrium or non-equilibrium given by

$$n = N_C \exp(\frac{E_{Fn} - E_C}{k_B T}) \tag{2.17}$$

and

$$p = N_V \exp(\frac{E_V - E_{Fp}}{k_B T}) \tag{2.18}$$

where N_C and N_V are the effective densities of state of the conduction and valence band, E_C and E_V are the conduction and valence band energies, k_B is the boltzmann's constant and T is temperature.

The occupation function $f(E_T)$ from the Fermi-Dirac statistics at thermal equilibrium is given by

$$f(E_T) = \frac{1}{1 + \exp(\frac{E_T - E_F}{k_B T})} \tag{2.19}$$

No net recombination occurs at thermal equilibrium, so $r_1 = r_2$ and $r_3 = r_4$. Hence the rate equations from figure 2.1 and 2.2 are used as a substitute, the emission coefficients e_n and e_p are

found as

$$e_n = v_{th}\sigma_n N_C \exp(\frac{E_T - E_C}{k_B T}) \tag{2.20}$$

and

$$e_p = v_{th}\sigma_p N_V \exp(\frac{E_V - E_T}{k_B T}) \tag{2.21}$$

where v_{th} is the thermal velocity related to holes and electrons, σ_n and σ_p are the electron and hole capture cross section related to the efficiency of the trap to capture the free charge carriers and E_T is the trap energy inside the forbidden band gap. If the N_C and N_V are substituted by the intrinsic carrier concentration, n_i multiplied by an exponential given as

$$n_i = N_C \exp(\frac{E_{Fi} - E_C}{k_B T}) = N_V \exp(\frac{E_V - E_{Fi}}{k_B T}) \tag{2.22}$$

where E_{Fi} is the Fermi level in the intrinsic material two new emission coefficients are found by

$$e_n = v_{th}\sigma_n n_i \exp(\frac{E_T - E_{Fi}}{k_B T}) \tag{2.23}$$

and

$$e_p = v_{th}\sigma_p n_i \exp(\frac{E_{Fi} - E_T}{k_B T}) \tag{2.24}$$

Each recombination claims one hole and one electron. At steady state recombination rate R_{SRH} is equal to

$$R_{SRH} = \frac{dn}{dt} = \frac{dp}{dt} = r_1 - r_2 = r_3 - r_4 \tag{2.25}$$

where $\frac{dn}{dt}$ is the rate that electrons leave the conduction band E_C. At steady state this equals the rate of holes $\frac{dp}{dt}$ leaving the valence band E_V. The electron/hole emission and capture r_1, r_2, r_3 and r_4 is shown in the table 2.1 and 2.2.

Table 2.1: Rates and trapping processes of electron and holes in donor-like traps

Donor-like traps

	Process	Rates
r_1	electron capture	$nv_{th}\sigma_n^+ N_T(1-f)$
r_2	electron emission	$e_n^0 N_T f$
r_3	hole capture	$pv_{th}\sigma_n^0 N_T f$
r_4	hole emission	$e_p^+ N_T(1-f)$

Table 2.2: Rates and trapping processes of electron and holes in acceptor-like traps

Acceptor-like traps

	Process	Rates
r_1	electron capture	$nv_{th}\sigma_n^0 N_T(1-f)$
r_2	electron emission	$e_n^- N_T f$
r_3	hole capture	$pv_{th}\sigma_p^- N_T f$
r_4	hole emission	$e_p^0 N_T(1-f)$

If the rates given in table 2.1 and 2.2 is substituted into equation 2.25, the steady-state occupation $f(E_T)$ is given by

$$f(E_T) = \frac{v_{th}\sigma_n n + e_p}{v_{th}\sigma_n n + v_{th}\sigma_p p + e_n + e_p} \tag{2.26}$$

where v_{th} is the thermal velocity related to holes and electrons, σ_n and σ_p is the electron and hole capture cross section related to the efficiency of the trap to capture the free charge carriers, n and p are electrons and holes, e_n and e_p is the emission coefficients of electrons and holes. A new equation of the SRH recombination rate R_{SRH} is found by substituting 2.25 into 2.26, which yields

$$R_{SRH} = v_{th}^2 \sigma_p \sigma_n N_T \frac{np - n_i^2}{v_{th}\sigma_n n + v_{th}\sigma_p p + e_n + e_p} \tag{2.27}$$

where N_T is the trap density, n_i is the intrinsic carrier concentration. By further simplification of equation 2.27, assuming the capture cross-section is the same for both holes and electrons $\sigma_n = \sigma_p \equiv \sigma_0$, the result is given by

$$e_n + e_p = 2v_{th}\sigma_0 n_i cosh\frac{E_T - E_{Fi}}{k_B T} \tag{2.28}$$

where σ_0 is the new capture cross-section and E_{Fi} is the Fermi level in the intrinsic material. Equation 2.28 can be derived into a less complex recombination rate equation given by

$$R_{SRH} = v_{th}\sigma N_T \frac{np - n_i^2}{n + p + 2n_i cosh(\frac{E_T - E_{Fi}}{k_B T})} \tag{2.29}$$

If assumed a p-type semiconductor with low injection rate where $p \approx p_0$ and $p \gg n$ the recombination rate R_{SRH} is given by

$$R_{SRH} = v_{th}\sigma N_T \frac{n - n_0}{1 + 2\frac{n_i}{p_0} cosh(\frac{E_T - E_{Fi}}{k_B T})} = c_n N_T (n - n_0) = \frac{n - n_0}{\tau_{n,SRH}} \tag{2.30}$$

where c_n is the electron captured coefficient and $\tau_{n,SRH}$ is the electron lifetime. The lifetime is related to capture coefficient given by

$$\tau_{n,SRH} = \frac{1}{c_n N_T} \tag{2.31}$$

where N_T is the trap density. It is seen that minority carriers lifetime is indirectly proportional to the N_T. The aim of the wafer manufacturer is to keep N_T low, as the lifetime should be around tens of ms to have an effective collection of photo-generated carriers [12].

2.2.3 Auger recombination

The third recombination process addressed is the Auger recombination, which highlights a different topic of photon energy transaction. In Auger recombination, energy and momentum is transferred from a recombining electron/hole to another charge carrier. This means that instead of radiation of photons the excess energy is lost as heat inside the crystal lattice, called thermalisation. This recombination method is the most important in indirect bandgap semiconductors. Energy and momentum is given either to excite another electron higher up in the conduction band E_C, or to a hole exited deeper into the valence band E_C as given by figure 2.7 page 12 [12].

As the Auger recombination is a three particle process, it is heavily dependent on the charge carrier densities n electrons and p holes. The recombination rates of electron-electron-hole R_{eeh} are dominant when electrons are the majority charge carriers and electron-hole-hole R_{ehh} are dominant when holes are the majority charge carriers, as given by

$$R_{eeh} = C_n n^2 p \tag{2.32}$$

and

$$R_{ehh} = C_p n p^2 \tag{2.33}$$

where C_n and C_p is the proportionality constants for electrons and holes. The C_n and C_p are strongly dependent on temperature in the sample. The total Auger recombination rate R_{Aug} is given by

$$R_{Aug} = R_{eeh} + R_{ehh} = C_n n^2 p + C_p n p^2 \tag{2.34}$$

If the p-type acceptor is heavily doped under low level injection, it can be assumed that $p \approx N_A$. This gives a new electron-electron-hole recombination rate, given by

$$R_{ehh} = C_p N_A^2 n \tag{2.35}$$

The lifetime τ_{ehh} is given by

$$\tau_{ehh} = \frac{1}{C_p N_A^2} \tag{2.36}$$

where C_p is the proportionality constant for holes and N_A is the acceptor concentration.

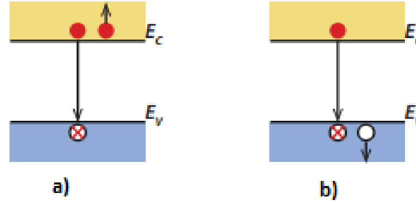

Figure 2.7: a) an electron recombines with a hole in the valens band and exites a neighbor electron further up in the conduction band, with corresponding release of excess energy to the crystal lattice. b) an electron recombines with a hole in the valence band, but exites a hole further into the valence band [12].

2.2.4 Surface recombination

All the recombinations addressed so far are bulk recombination mechanisms, meaning the situation is taking place inside the silicon crystal. As the wafers in the current work are "as cut", the chance of surface recombination occurring at the edge is present. Surface recombination, called dangling bonds, as shown in figure 2.8, it is related to loose ends from the Si-atoms at the edges of the crystal lattice. These loose ends create a vast number of traps inside the forbidden bandgap. The surface recombination rate R_s is given by

$$R_s = v_{th} \sigma_n N_{sT} (n_s - n_0) \tag{2.37}$$

where the v_{th} is the thermal velocity, σ_n is the capture cross section for electrons, N_{sT} is the surface trap density, n_s is the electron concentration at the surface and n_0 is the hole concentration in a p-type semiconductor at equilibrium.

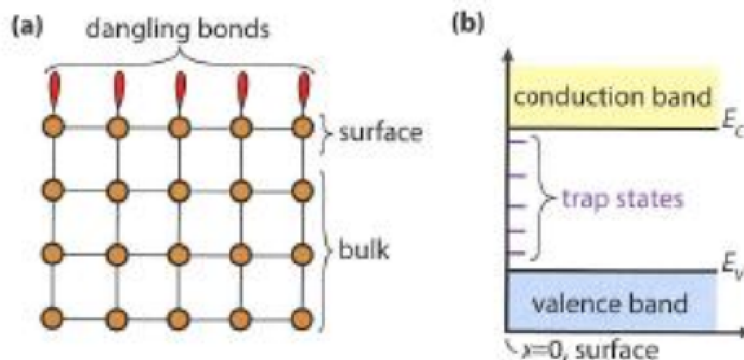

Figure 2.8: In (a) the dangling bonds is seen at the surface of the bulk, allowing different trap states in the forbidden bandgap seen in (b). [12].

2.3 Defects in mono-like silicon

The defects in the mono-like silicon ingot can be related to point defects, dislocations and grain boundaries imperfections.

2.3.1 Point defects

As for the recombination process, there are two types of point defects in semiconductors. They are called intrinsic point defects, natural part of the silicon ingot, and extrinsic point defects that relates to impurities or complexes. In an intrinsic point defect there are two types; Schottky defect and Frenkel defect [17]. In the Schottky defect a Si-atom would leave the lattice structure forming a vacancy and diffuse through the lattice out to the surface [17,18]. In the Frenkel point defect the Si-atom also leaves a vacancy, however, do not diffuse to the surface. Instead the Si atom moves inside the lattice to an interstitial location usually not occupied by an atom and thus becoming an interstitial defect [17]. Both the Schottky and the Frenkel point defects are shown in figure 2.9.

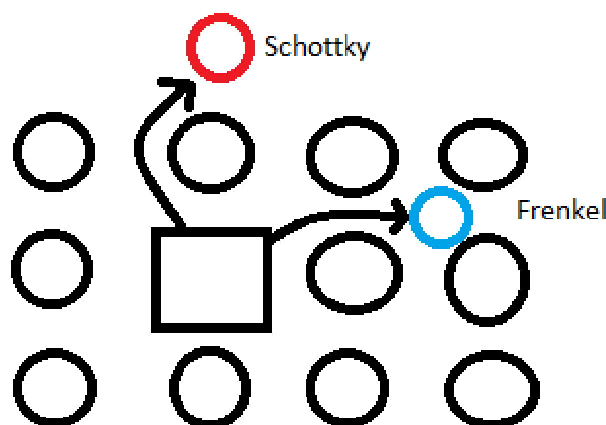

Figure 2.9: Schottky and Frenkel point defect in a crystal.

Extrinsic point defects are impurities like iron diffusing into the crystal lattice as interstitial impurities or complexes with iron-boron. This is discussed in a paper by Macdonald et al. [19], and also discussed in an accepted paper by Mehl et al. not published, based on work by Graff et al. [20].

2.3.2 Dislocations and grain boundaries

Dislocations are formed when shear stress moves through a lattice as a line imperfection. Several types are known, and two types will be mentioned here; edge and screw dislocations [17]. An edge dislocation can be thought of as a lattice of atoms where an upper part of the lattice has been inserted with an extra plane of atoms [17]. The dislocation is seen in figure 2.10.

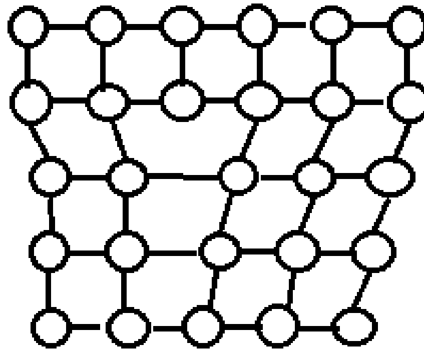

Figure 2.10: Edge dislocation, where the upper area has been inserted with a extra plan of atoms.

Screw dislocations is the junction where the slipped part of the crystal meets the unslipped part. In screw dislocations the boundary is parallel with the slip direction, instead of perpendicular as in edge dislocations. This is seen in the figure 2.11.

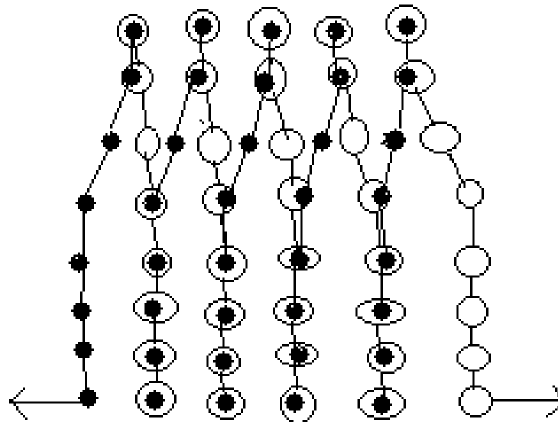

Figure 2.11: Screw dislocation. Boundary is parallel to the slipping plane where the dislocation occures.

In the work of Ekstrøm et al. [1], different grain boundary angles are discussed at the different seed crystal junctions. A grain boundary angle can consist of an array of dislocations. A grain boundary type is denoted a Σ type. A boundary like this is called a pure tilt boundary and describes a misorientation of two planes by a rotation θ around an axis, as given by figure 2.12 [17].

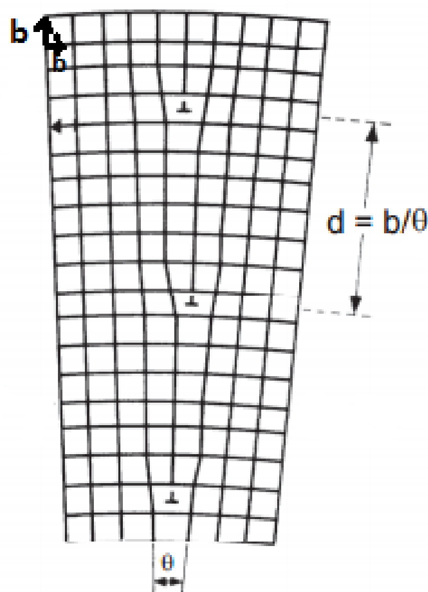

Figure 2.12: The figure shows a misorientation angle. An angle θ rotates around a plane axis and dislocations occure each length of $D = \frac{b}{\theta}$ [17]

.

Twinnings are crystallographic reflections of the ingot growth plan. In the work done by Ekstrøm et al. [1] this is discussed thoroughly.

2.3.3 Defect related luminescence

Defect related luminescence (DRL) is a name for photons with lower energy than the bandgap energy E_G of the investigated semiconductor. The DRL is often based on experiments that investigate photoluminescence (PL), which is light emission signals radiated from the bandgap or traps inside the forbidden bandgap [10, 21]. This occurs when charge carriers are excited by a light source. When the electron recombines with a vacant hole at the valence band level or in a trap state, a photon with a specified energy can radiate [12]. Work by Shockley et al. [16] and Hall et al. [15] was published in 1952. The radiation will be capured by a camera and seen as a PL emission signal. By cooling the test specimen with liquid nitrogen or helium freezes the phonon movement, the free charge carriers will seek to the state of smallest possible energy either near the band edges or trap states [8, 11]. This is seen as the sharp peaks of energy called the D-lines found by Drozdov et al. [8] in 1976, where energy levels are detected as the band gap $E_C - E_V$ or trap states $E_T - E_V$. The PL signals were found as a band to band related apex of 1.092 eV and four different apexes called D1, D2, D3 and D4 related to 0.812 eV, 0.875 eV, 0.934 eV and 1.000 eV, respectively [8]. When the Drozdov et al. [8] was published, it was

known that dislocations could be electrically active, while no information was published on the topic of D-lines related from dislocations in silicon [8].

The dislocation topic related to D-lines was confirmed by Sauer et al. some years later and the D1/D2 and D3/D4 DRL were found to be in pairs [22].

Now at present time and after decades of research the D1 PL emission signal has been thoroughly investigated. Work done by Pizzini et al. [23] suggests that D1 PL emission signal of 0.814 eV, with a converges energy at 0.807 eV, is found when dislocations are without oxygen. The work mentions the discovery of another PL emission signal called D5, with the energy of 0.846 eV. Pizzini et al. [23] suggests that D5 PL emission signal can be related to dislocations that are decorated with oxygen precipitates. Both of these statements published by Pizzini et al. [23] applies for Cz-Si crystals. Another topic in the study is the D2 PL emission signal which is also suggested to be related to dislocations with oxygen as a shoulder of D1. This is hypothesized when oxygen precipitation stages annealed longer than 8 hours [23].

In 2012 the work by Tajima et al. [24] suggests that D1-D2 PL emission signals originates from dislocations where oxygen precipitates are present. Note that the misorientation angle of small angle grain boundaries (SAGB) are 1-2° in these dislocations, in misorientation angles $< 1°$ oxygen was not found.

The D3-D4 PL emission signals have also been thoroughly investigated. There are widespread agreement that the D3-D4 PL emission signals are related to metallic impurities [11, 21]. Work done by Lausch et al. [21] states that D4 is related to iron precipitates and D3 is a phonon replica of D4. A new method of classification was in 2012 introduced by Lausch et al. [25] based on a model published by Kveder et al. [26] in 2001. A notation of Type A and Type B was used to systematize the D-line. The Type A classification was related to different traits corresponding to D3/D4 defects. The Type B classification was related to D1/D2 defects. Later in an accepted still in press work by Mehl et al., it is stated that D3-D4 PL emission signals originate from iron-boron complexes (FeB). In the same paper a PL emission signal of around 0.7 eV is discussed and can be related to interstitial iron (Fe_i). An earlier published paper by Kveder et al. [27] D3 and D4 PL emission signals have been related to stress induced by intraband defects near the valence and conduction band.

PL emission signals in room temperature have been investigated to confirm the investigations done with cooling [27, 28]. Work done by Tarasov et al. [28] observed a 0.8 eV emission signal and concluded that it was related to D1/D2 PL emission signal and could be related to oxygen precipitates.

2.4 Diffusion

Diffusion in silicon occurs when an uneven concentration either of vacancies or impurity atoms in a silicon crystal [17]. A flux from high concentration to low concentration will initiate. At the point where the gradient approaches zero the impurities or vacancies are equal distributed and equilibrium has been achieved. The diffusion flux J_N follows Fick's Law and is given by

$$J_N = -DgradN \tag{2.38}$$

where J_N is the number of atoms crossing a unit area in a unit time, D is the diffusion constant and $grad$ is the gradient. The negative sign can be interpreted as the direction of the flux from high to low concentration areas.

The chemical potential is the driving force, with its dependence on temperature given by

$$D = D_0 \exp(\frac{-E}{k_B T}) \tag{2.39}$$

where E is the energy activating the process, k_B is the boltzmann constant and T is the temperature, and D_0 is a reference diffusion constant.

2.5 Hyperspectral imaging

Hyperspectral imaging is a non-destructive method that has been used with success to investigate mc-Si solar cells [10, 21]. The strength of the method is the combination of spectroscopy and digital imaging. In a normal digital camera each pixel of the captured radiance acquires three spectral channels, which are corresponding to the primary colours red, green and blue. A hyperspectral camera acquires radiance up to several hundred spectral channels [29]. There are a widespread of applications to hyperspectral imaging other than investigations of solar cells, such as the agriculture, military and medicine [30–32].

It exists a number of metods which a hyperspectral camera can operate. In the current work the hyperspectral camera uses a technique called the pushbroom scanning mode [29]. The camera gains a spatial dimension by a spatial movement cross the scene in one direction. Light passes through the camera lens, capturing images one narrow spatial line from the scene at a time. Light passes through a slit focused by a focus mirror before a collimation process occur. Meaning the light rays are sendt as parallel rays before arriving at the sensor array. Each line is then split up into its spectral components. Each sensor has one spectral dimension and one spatial dimension. The two spatial dimensions and the one spectral dimension are put together in a 3D matrix called a hypercube.The dimensions forming the hypercube is seen in figure 2.13. This can be looked upon as a two dimensional image for each spectral channel [29]. In figure 2.14 the camera function is given. The reader is encouraged to look elswhere for more information [10, 29, 30].

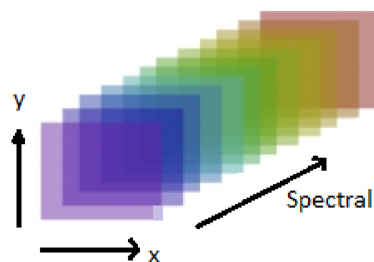

Figure 2.13: Dimensions in a hyper spectral image.

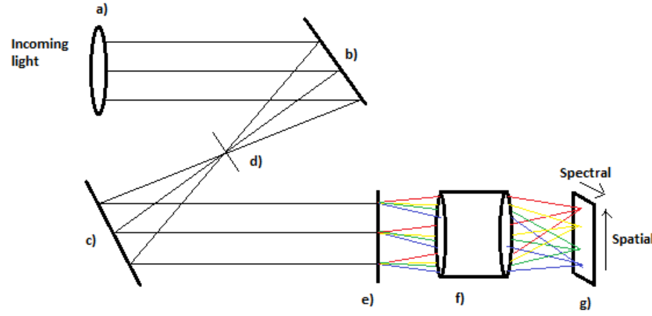

Figure 2.14: a) light passes through the camera lens before focused at b) through a slit d) before collimating c). A sensor array splits up the light into its components by a diffraction grating e) in the camera optics the components is focused f) and the corresponding spectrum is gathered in a detector array g).

2.6 Multivariate curve resolution

Multivariate curve resolution (MCR) is a statistically, analytical tool which has been used with success in collaboration with the hyperspectral imaging to extract relevant information from different types of solar cell samples [11, 21]. To achieve a successful extraction of information, a defined number of components are needed. In the current work this has been solved by the trial and error method. By defining different components each time, the number of components best suited was found. The MCR algorithm will use a bilinear model to convert the original image D into pure responses of the data variance as a row matrix C and column matrix S^T. The mathematics of the bilinear model are given by

$$D = CS^T + E \tag{2.40}$$

where D is the hypercube collected by spectroscopy, C is the column matrix with the concentrations profiles (sometimes named the score matrix), S^T is the row matrix with the pure spectra (sometimes called the loading matrix), and E is the matrix related to errors or noise.

The MCR algorithm also uses a least square method called Alternating least squares (ALS) [33]. The ALS method seeks convergence using an iteration to optimize the C and S^T to the original matrix D [33, 34]. To extract the information in D the hypercube is first unfolded into a two dimensional matrix and the MCR algorithm extracts the proposed number of components fitting the original hypercube [33]. It is necessary to choose the right constraints before MCR forms the C and S^T matrix. These constraints can be; non-negativity, unimodality, closure, triliniearity or selectivity. In the current work non-negative constraint is used because negative values have no physical meaning in this experiment. When constraints are chosen, MCR finds the best fitted concentrations matrix, C, and the pure spectra matrix, S^T, and visualize these as a score image and loadings plot, respectively. In the current experiment 17 components was defined as the best choice. The MCR algorithm will deliver error and flawed information like noise and pixel errors. Noise can be seen as oscillating waves over the entire spectrum, pixel errors on the other hand are sharp one pixel spikes suddenly erupting from the spectrum curve. The MCR process is given in figure 2.15. The strength of the MCR algorithm is its attribute to separate the pure component spectra corresponding to the emitting sources, even if they overlap

spectral and coincide spatially with each other [35]. Like the hyperspectral imaging the reader is encouraged to look elswhere for more information [33–35].

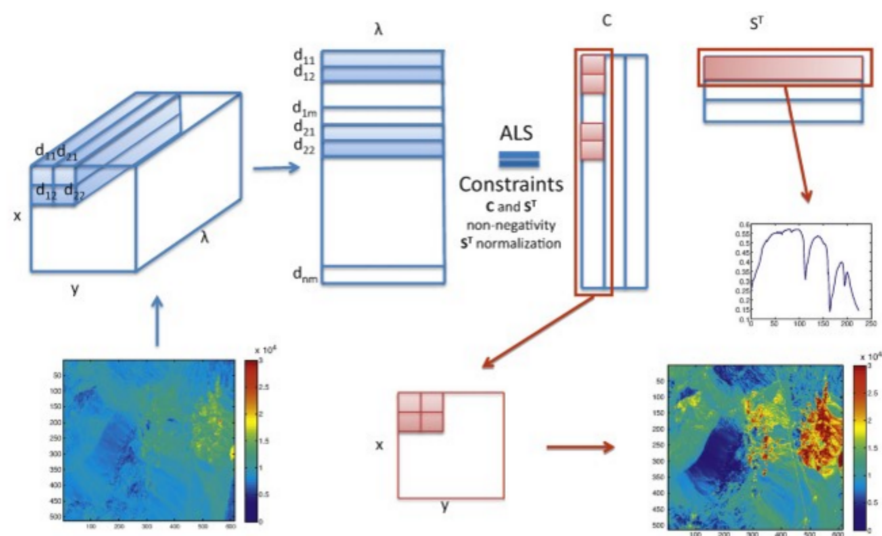

Figure 2.15: An image is loaded into the MCR algoritm, the hypercube D is unfolded from a 3D matrix to a 2D matrix, the ALS algorithm finds the score image from the C matrix and the loadings from the S^T matrix [34].

Chapter 3

Experimental and experimental setup

Figure 3.1 schematically shows the experiment setup used in the current work. A hyperspectral camera and a laser are connected to a rig running forward and backward on a track. To ensure the laser radiates with the same intensity over the complete wafer surface, it is adjusted to radiate a wider area than the width of the wafer. The velocity of the rig is controlled by an electric motor, which is governed by a computer program. The speed of the rig is calculated to 1.88 mm/s when 75 μm images were taken and 12.7 mm/s when 508 μm images were taken. The scanning length was set to 17.0 cm. Note that the wafer was 15.6 cm long, but in later processes the need of extra scanning length was necessary to subtract background noise from the raw image.

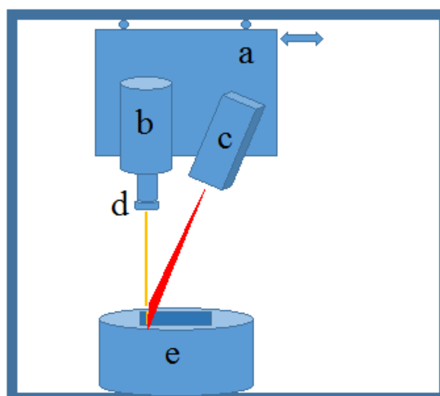

Figure 3.1: Schematic representation of the experimental setup. (a) is the rig sliding on tracks moving in two different directions, (b) is the hyper spectral camera capturing PL emission from the mono-like sample located on an aluminium surface, (c) is the 810 nm laser illuminating the wafer, (d) is the camera lens that can be rotated to increase focus and (e) is the cryogenic cooler storing the liquid nitrogen [21].

3.1 Mono-like silicon ingot and its wafers

Four 15.6 cm × 15.6 cm "as cut" mono-like silicon wafers were used in this experiment, where the wafers was cut from different locations. One was cut from near the ingot bottom at the height of 42.4 mm numbered A-108. Two wafers from the middle of the ingot, one at 53.3 mm numbered A-80 and one at 54 mm numbered A-78. Near the top of the ingot one wafer was cut at the height of 66.3 mm numbered A-45. This is given by figure 3.3. Note that the height of all four wafers is measured from the ingot bottom. The silicon ingot was a seed-assisted, 12 kg pilot scale mono-like silicon ingot with a total diameter of 250 mm and a height of 107 mm [1]. It was a boron doped p-type ingot with six equally oriented mono-crystalline slabs, where the seeds came from a Czochralski ingot. The slabs were placed at the bottom of SiO_2 crucible with Si_3N_4 coating, silicon feedstock was added and the melting process took place in a Crystalox DS 250 directional solidification furnace. As the solidification started the ingot was grown in the <110>direction. For more information about the mono-like silicon ingot preparation can be found elsewhere [1].

Figure 3.2: Figure show one of the mono-like wafers, A-78

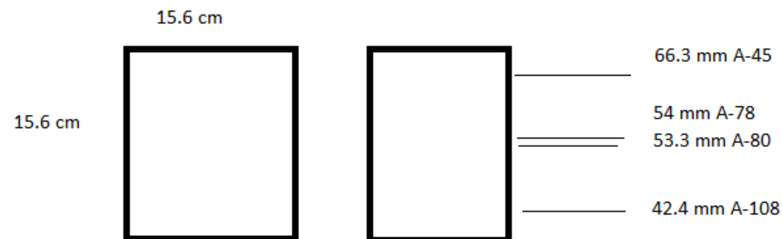

Figure 3.3: The dimensions of one mono-like wafer and the height each wafer was cut from.

3.2 Cryogenic container and thermometer

To freeze out phonons it was necessary to maintain low temperature throughout the experiment. A cryogenic holder was used to cool and maintain sufficent low temperature. The holder has walls and bottom in styrofoam and a set of cooling ribs inside the styrofoam. The liquid nitrogen was poured into the cooling rib setup. The cryogenic container was produced at NMBU by senior engineer Arne Svendsen. To increase the cooling effect, direct contact between the wafer and the metal top of the cooling system was important. At the top of the cryogenic cooler the wafer is placed. There on all four sides small holes are located. This achieved rapid reach of temperature equilibrium with the cooling system and wafer. The holes also delay frost build up on top of the cooled wafer. The experiment was conducted at temperatures of 88 ± 2 K. To monitor the wafer temperature a digital thermometer of the type TENMA 72-7712 T-type was attached to the upper surface of the cooling setup. The range of this thermometer was -250 to 400 degrees Celsius with a resolution of $0.1 \pm 0.005°$ Celsius.

3.3 Laser

The laser used in this experiment is a Lasiris Magnum II Laser manufactered by Coherent Inc, Portland, USA. The laser has a wavelength of 810 ± 1 nm, a maximum radiation effect of 6000 mW and a 30 degree fan angle. The experiment was conducted with a laser voltage of 4 V.

3.4 Hyperspectral camera and low-pass filter

The camera used in the experiments were an HgCdTe SWIR Specim from Spectral imaging Ltd Oulu Finland. This was a near infrared hyperspectral camera. Two dimensions were captured by the camera, one spatial, noted as x-axis with 320 pixels and one spectral λ. A second spatial dimension is obtained because of the movement by the rig, this spatial dimension is denoted y-axis. To capture the spectral dimension λ, 256 light sensors measure photon intensity. Together the 256 light sensors capture photons wavelengths from 1000 nm to 2500 nm, with nominal spectral resolution of 10 nm. This relates to photon energies of 1.3344 eV to 0.4899 eV. To translate the wavelengths into energy, a table of each sensor mean values were used. All the values are listed in Appendix B. The camera also had an adjustable lens, which could adjust the sharpness of the image to ensured optical accuracy. In the experiments 25 images per second were used with an exposure time of 20.0 ms and three pictures were taken of each wafer.

A 850 nm low pass filter was used in the experiment because of the second-order wave refraction at 1616 nm the camera would detect. The low pass filter shuts out shorter wavelengths than 850 nm. This is a necessary trait since frequency and wavelength are opposite proportional to each other. Meaning the lower frequencies than 850 nm passes through.

3.5 Data processing

A computer program, Specim DAQ solution software Ver. 3.62 was used to control the components of the rig in this experiment. The procedures such as exposure time, rig velocity, scanning length, retraction velocity, shutter time and so on were handled by the computer program. All images were saved in the .raw image format accompanied by a header file where image information was stored. The user could do a fast quality check of the image in the computer program ENVI. As mentioned in 3, a longer scanning length was used, the reason for this was to

subtract background noise. Another feature developed by the solar physics group was a method of using the median of three images. A Matlab code was developed by removing further noise from the score image. Matlab codes used in the current work originats from the work by Mehl [36] at NMBU. No new numerical analysis was made for this work. Matlab and MCR was used to extract information from the raw hyperspectral image and the MCR algorithm was executed with a non-negative constraint [33]. In the experiments Matlab R2015b (8.6.0.267246), Math Works Inc, USA and toolboxes for MCR analysis MIA and PLS-toolbox, Eigenvector Research Inc, USA were used.

Chapter 4

Results and discussions

4.1 Experimental results from MCR

In this section the results from the experiment with cooled wafers by MCR algorithm is shown. The same experiment was also conducted in room temperature. This experiment gave no results other than a small band to band emission and are left out of the current work.

4.1.1 MCR results of SPL of wafers A-108 through to A-45.

The four wafers were investigated with two different pixel resolutions. One type of dataset had 420×320×256 pixels with a 508 μm resolution. The other type of data set had 3000×320×256 pixels with a 75 μm resolution. The complexity of the dataset requires statistical tools like MCR to extract information. The MCR algorithm extracts separated pure spectra components as defined by the user.

The extraction of the information from the wafers was done by Matlab as shown in figure 4.1.A challenge is that some of the important information is not visualized, only one graph is seen in figure 4.1. After the experiments were finished, the data processing found PL emission signals at 0.812 eV, 0.875 eV, 0.934 eV, 1.000 eV and 1.092 eV. The 1.092 eV signal was recognized as the band to band (BB) signal. The other four PL emission signals are the known D1, D2, D3 and D4. At the A-108 wafer near the bottom of the Si ingot only the PL emission signal of D1, D2 and BB are found, with increased height, the rest of the DRL are introduced in the figure 4.1. The knee of the BB PL emission signal and can be related to a phonon replica of BB.

As seen figure 4.1 provides little information. To collect more information from the data sets, MCR has been incorporated. The MCR model extracts PL signals from each wafer and categorize them into neat and easy to understand graphs, as shown in the figure 4.2.

In figure 4.2, MCR with 17 components is used. The reason for this is the interesting PL signals are shown to best extent as single MCR components. When higher amount of components were used, the important D07 signal, discussed in 4.4, did not appear as expected. MCR investigations with fewer components jeopardized the experiment by not showing the interesting components distinctly. There is no doubt that for a MCR investigation with 17 components, the MCR algorithm will visualize uninteresting and even flawed components. These components were related to BB PL emission signal, pixel error and noise, and for the convenience of the reader removed from the figures in the current work. Both more and fewer component investigations are shown with figures of all 17 components in Appendix A.

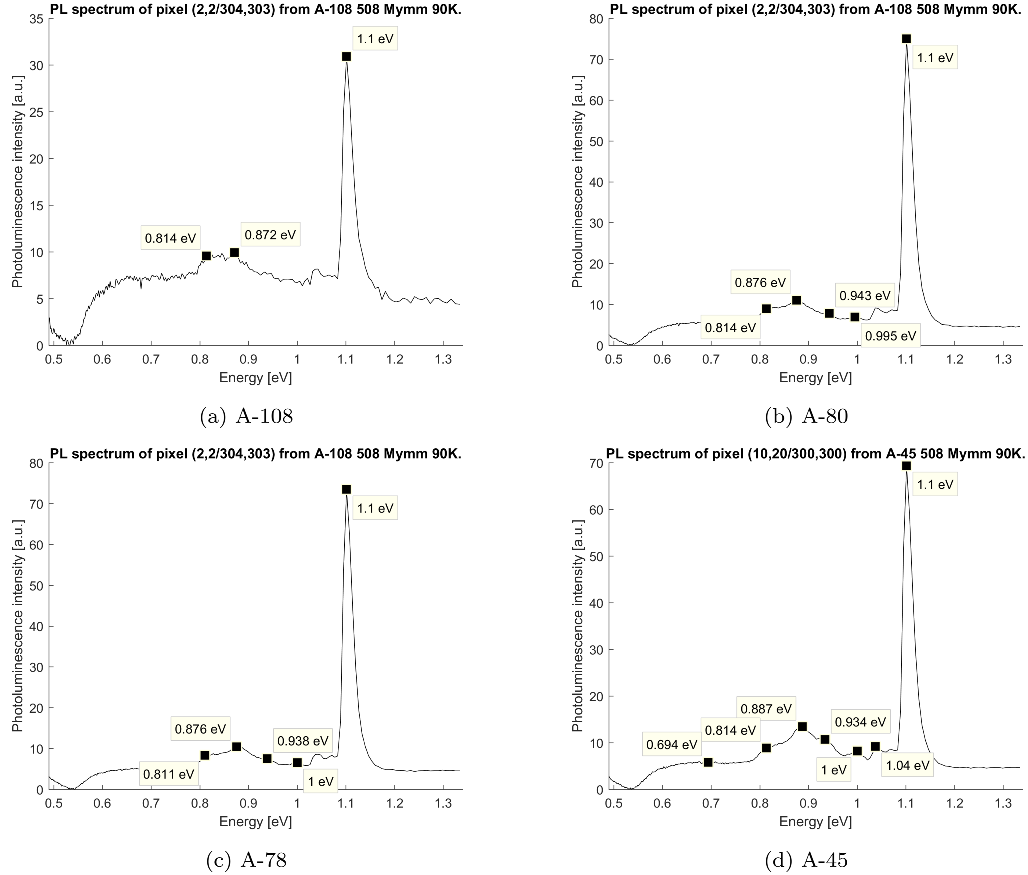

(a) A-108 (b) A-80

(c) A-78 (d) A-45

Figure 4.1: Integrated information in the datasets of the four different wafers by Matlab. Energy given in eV is shown on the X-axis and concentration on the Y-axis.

4.1.1.1 MCR A-108

In figure 4.2 a) PL emission signals from the A-108 wafer are shown. The MCR detects 3 components that are not BB or noise. The PL signals related to D1 and D2 are clearly showing with an extra signal of 0.835 eV. A small signal around 1.0 eV is also present subsequent to the D1 related component. Since the A-108 wafer is a near bottom wafer cut from 42.4 mm as seen in figure 3.3. It is expected to have numerous problems such as interstitial impurities and red zones. These defects can be a reason why there are not much signal in this wafer. This is discussed further in the section 4.1.2.

4.1.1.2 MCR A-80

Wafer A-80 is shown in figure 4.2 b), this wafer is in the middle of the ingot at 53.3 mm above the ingot bottom as seen in figure 3.3. MCR extracts 4 components that are useful. PL emission signals related to D1 and D2 are much like the signals in A-108, investigating further an increase in the 0.94 eV and 1.0 eV PL signal that seems to be a tail of the D1 PL signal. The D1 PL signal seems to be diminishing from the A-108 D1 PL signal, while the D2 signal is constant. A

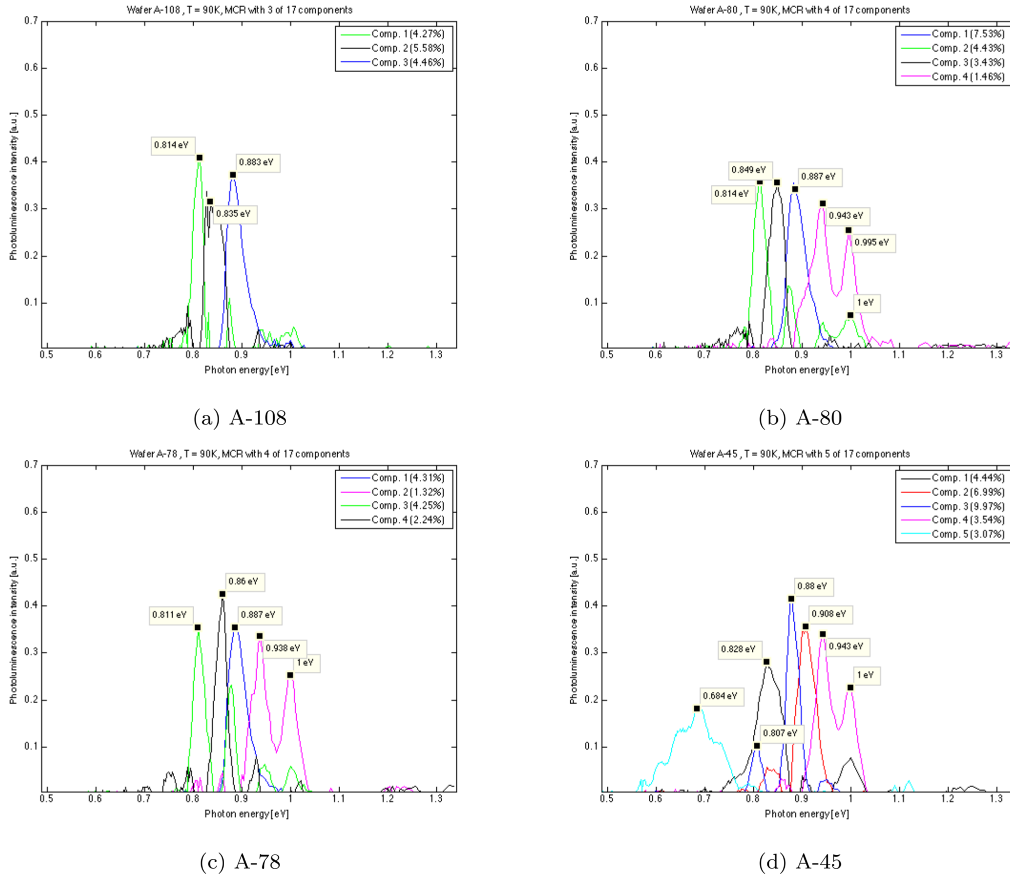

Figure 4.2: MCR load plots showing the growth of PL emission signals from the A-108 wafer near the bottom, A-80 and A-78 at the middle to the A-45 near the top of the mono-like silicon ingot. Energy given in eV is shown on the x-axis and concentration on the y-axis.

clear PL signal with two distinct apex at 0.943 eV and 0.998 eV related to D3 and D4 have been established alongside a new signal of 0.849 eV. The 0.849 eV signal was not mentioned in the work by Drozdov et al. [8], however, the emission signal was mentioned in a paper published by Pizzini et al. [23] with the name D5.

4.1.1.3 MCR A-78

As for the A-78 middle wafer in figure 4.2 c) there are only 0.64 mm difference in height from the A-80 wafer located at 54 mm over the ingot bottom. This implies that the MCR results should be similar and the MCR analysis confirms this. The PL signal related to D1 is following its behaviour in A-80 and is declining, while the D2 related PL signal is the same as for A-80. The new signal from A-80 is increasing in intensity and seems to have shifted in energy as well to 0.86 eV. A closer look to the D3/D4 component seems to find an increase in the D3 PL emission signal apex, while the D4 PL signal apex has around the same intensity. Note that at the middle of the ingot an increase in metallic precipitations from the crucible should be present and oxygen impurities should diminish.

4.1.1.4 MCR A-45

Closer to the top at 66.3 mm above the ingot bottom wafer A-45 is located. In the figure 4.2 the DRL signals are stronger than in the A-78 wafer with a higher DRL percentage, as shown in the legend. This means that the defect DRL signals are a larger part in the original image near the top than at the middle or bottom of the ingot. This could be explained by an increase in impurities with increased height.

The D1 related PL signal is faltering and is decreasing in strength. The shape of the graph indicates that the MCR algorithm has difficulties separating the D1 PL signal and the 0.86 eV PL signal and count them as one. This can be explained by a close spatial location of the two signals. The D2 related PL signal is the strongest compared to the other DRL signals in this wafer and have increased quite a bit in intensity with the elvated height of the ingot. The D3 and D4 related PL signal are similar to the A-78 signal with a higher D3 apex here than in A-78. Suddenly two completely new signals are establish with PL signal of 0.684 eV and 0.908 eV. These signals have not been seen before and can possibly be related to events happening at increased height in the ingot. The 0.684 eV PL signal have been seen before in other studies and it is mentioned in work done by Lausch et al. [21]. On the other hand the 0.908 eV PL emission signal has not yet been covered in scientific publications. Both of these PL signals will be discussed more thoroughly in the current work.

4.1.2 Section disccussion

In A-108 wafer the investigation found very little signal at all and MCR troubled with the extraction of relevant spectrums. Only 3 components out of 17 where logic, and this can be related to the small amount of signal in the A-108 wafer. If the signal had been stronger, more components would likely be shown. Another solution to this is that there are no other signals than D1 and D2 PL emission signals in the A-108 wafer.

The bottom of the ingot often have large oxygen impurities, as stated by Geerligs et al. [13]. If the D1 is related to oxygen, as stated by Pizzini et al. [23] then this may be related to the high intensity D1 PL emission signal in A-108. It is known that Cz-Si has oxygen impurities, using Cz-Si seed crystals these impurities can diffuse into the seed junction dislocations and be locked. The diffusion will increase in liquid, if a greater part of the seed crystal is melted oxygen diffusion is possible. Another possibility of an oxygen impurity source is the crucible bottom. As shown by figure 4.2, D1 PL signal decreases with increasing height of the ingot. An explanation for this may be that the oxygen level decreases with elevation. The oxygen impurities locked in the thin A-108 seed junction diffuses away from the dislocations as the dislocations gets wider. When the impurity concentration level decreases, the radiative recombination concentration level will also decrease. If the camera used in the experiment capture fewer emission signals from the radiative impurity photons, the intensity will decrease, compared as done when the impurity concentration is high. Note that if the segregation coefficient of oxygen is > 1, oxygen can congregate near the bottom of the ingot [13, 37]. This is a suggestion to why the D1 PL emission signal behaves as it does trough the ingot.

An interesting result extracted by MCR is the tail at the D1 PL signal component, seen in figure 4.2. This component has an apex around the 0.93 eV and 1.0 eV area. The intensity of this signal increases with the elevated height as the wafers were examined. The D1 component shoulder was mentioned in a paper by Lausch et al. [21]. In another paper by Savchouk et al. they mention the 0.9 eV apex is segregated and related to Si-H bonds in microcrystalline thin film [38]. The 1.0 eV tail from D1 PL related component has not been addressed yet. As seen in figure 4.2 d) there is also a tail on the 0.906 eV component peaking at 0.84 eV. Surface

recombination will produce large number of trap states [12] with different energies, however, this needs to be investigated further.

As for the growth in D2 PL emission signal with elevated ingot height the author has not clearly understood the topic. It seems that the process with D2 PL signal is opposite of the D1 PL signal. If there is an impurity causing the D2 signal, it seems to be trapped inside the dislocations or grain boundaries in the seed junctions. Unlike the D1 PL emission signal explanation, the D2 PL signal increases from the middle of the ingot as the solidification reaches elevated height. The impurity causing the D2 PL signal seems to diffuse to the junctions. In the paper from Pizzini et al. [23] it is suggested that the D2 PL emission signal is a shoulder of the D1 PL emission signal and discovered when oxygen is introduced to the Si ingot. Note that this occur only when oxygen precipitation stages annealed longer than 8 hours. Anneal time is not known in the examined Si ingot. If the D1 diminish because the number of oxygen impurities diminish, and the D2 PL emission signal also can be related to oxygen, the D2 signal should diminish as well, not grow with increasing height. Some other unknown factor must be present.

D3/D4 PL emission signals are growing throughout the ingot, however, it is not present in the A-108 ingot as a single componet, only as a tail of the D1 PL emission signal. In A-80 and A-78 the signals are present as a single component and further growth are negligible from A-78 to A-45, both in shape and intensity. If the D3/D4 PL emission signals are originating from metallic impurities, PL signals would increase closer to the top of the ingot. To reasons for this remark, the metallic segregation coefficient as iron (Fe) is typical < 1 and more metallic impurities will precipitate from the crucible wall [39]. Intuitively, metals will accumulate towards the top of the ingot. It seems logical that the D3/D4 PL emission signals comes from metallic impurities as other studies have indicated [11] [21]. Both of the last two papers suggests that D4 PL emission signal originates from a metallic impurity and D3 PL emission signal is a phonon replica. The explanation for this statement is that MCR treats D3 and D4 as the same component and therefore is close to the same defect. The interesting part is the intensity of D3 PL signal is higher than the D4 PL signal, at A-45 it is about 50% higher. In the paper from Flø et al. [11] this is explained by the discovery of a PL signal called Very Intense D3 (VID3) that MCR merges into one signal. In this investigation the search for VID3 has been unsuccessful.

In 2016 accepted paper, still in press by Mehl et al. another suggestion D3/D4 Pl emission signals is stated. The work suggests that D3/D4 PL signal originates from iron-boron complexes (FeB). This suggestion is based on work by Graff [20], where FeB has a trap state of $E_V + 0.1$ eV correlating with the D4 PL signal of 1.000 eV. Then D3 PL signal is a phonon replica with about 0.05-0.07 eV lower energy, peaked normally at 0.934 eV. In this investigation MCR treats the D3/D4 PL signal as one component, which can be related to the same spatial location of these two PL emission signals. Since the ingot is a p-type, boron doped, and the metallic impurities should increase with height a growth in D4 PL emission signal with the phonon replica of D3 seems logical.

As seen in figure 4.2 a signal with apex of 0.684 eV has been established. This signal will be discussed more thoroughly in a section 4.4.2.

4.2 Experimental Matlab results

In this section results from Matlab of the different PL emission s are shown in score images. In Appendix C the same PL emission signals are given. However, in Appendix C the intensity is locked to the A-45 BB intensity. The reason for this is to understand better how the different PL emission signals propagates through the ingot. The reader is encouraged to examine the results from the section 4.2.1 with the results in Appendix C.

4.2.1 Matlab results from SPL of wafers from A-108 through to A-45

By using Matlab the original 3D raw image of the 256 different PL signals obtained by the spectral photoluminescence (SPL) are processed. After data processing the interesting emission signals are extracted from the non-important emission signals. To do this a translator is needed to change spectrum data to energy data and is shown in Appendix B. The results from the SPL data extraction of the interesting emission signals are shown in this section as score images. Combining the score images with the loading plots shown in 4.1.1 a precise visualization is given of the emission signals.

Score images of each investigated D-line defect related luminescence from all four mono-like wafers have been compared to each other. In figure 4.3, 4.4, 4.6, 4.7, 4.8 and 4.9 the BB, D07, D1, D2, D3 and D4 PL emission signals is shown. The colour bar on the right side displays the intesity of the score image. The intensity is related to how many photons are detected by the hyperspectral camera from each pixels of the image. The intensities varies from wafer to wafer and are set to each emission signal intensity. This is done to visualize the difference in each emission signal throughout the Si ingot.

The BB gap in silicon is well known to be 1.092 eV [8]. After the experiment was conducted it was established that the wafer A-108 has low BB PL signal, as discussed in 4.1.2. The A-108 wafer has been cut from the lowest part of the ingot at 42.4 mm above bottom and should be affected by a large order of impurites. The BB PL signal from the four different wafers are shown by figure 4.3.

As seen in the colour bar the intensities of the concentrations are varying with increasing height the wafers are cut from. It can be easily noticed the different blue areas located above the seed junctions, which are comparable with the red zones mentioned by Ekstrøm et al. [1]. The blue areas are dead areas with defects and grain boundaries that should contain impurities that initiate traps in the forbidden band gap of each silicon wafer. The difference in blue areas around seed junctions will be investigated in section 4.3.

The weakest PL emission signal as stated by Drozdov [8] is the D1 defect with the PL emission signal of 0.812 eV. Later, in recent time different studies by Flø et al. [11] and Lausch et al. [21] mention another PL emission signal with even lower energy around 0.7 eV, called D07. The D07 emission signal and its growth through the ingot is shown in the figure 4.4.

The D07 PL signal is interesting because of two things. First, it seems that the signal is corresponding to the growth of the parasitic crystal forming from the crucible wall, mentioned in the paper by Ekstrøm et al. [1]. Second, the PL emission signal is scarce at the A-108 wafer, not found by MCR at this height. The signal increases in intensity with increasing height to a strong signal near the top wafer A-45.

With a little higher energy, at 0.812 eV the PL emission signal related to D1 is found as stated by Drozdov et al. [8]. When examining the wafers the D1 PL signal seems to be one of the strongest DRL signal. Since the defect related luminescence are found in the seed junctions a figure of the seed junctions is given in the figure 4.5. Score images show that the PL emission related D1 signal is richest around seed junction 2.3, with a small, but high density, D1 area in

junction 2.1. Although the PL signal with the largest area is junction 2.3, the 2.1 junction seems to experience stronger and denser growth. It is established from the images that the PL emission signal is strongest around the centre of the seed junctions. However, with the increasing height, the PL signal is more scattered. The D1 PL emission signal is shown in the figure 4.6. As shown in the figure, lesser concentrated areas is found with increased height of the ingot.

Score images show that the PL emission related D1 signal is richest around seed junction 2.3 with a small, but high density D1 area in junction 2.1. Although the PL signal with the largest area is junction 2.3, the 2.1 junction seems to experience stronger and denser growth. It is established from the images that the PL emission signal is strongest around the centre of the seed junctions. However, with the increasing height, the PL signal is more scattered. The D1 PL emission signal is shown in the figure 4.6. As shown in the figure a lesser concentrated areas is found with increased height of the ingot.

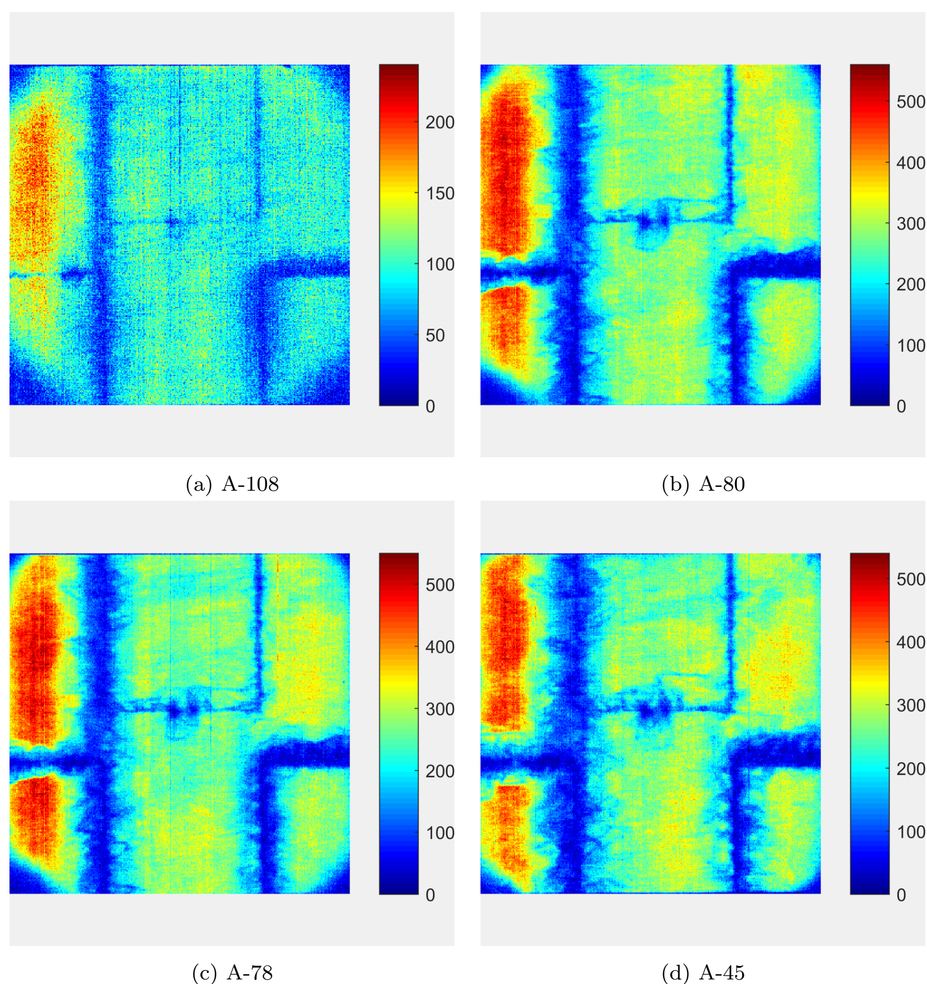

(a) A-108　　(b) A-80

(c) A-78　　(d) A-45

Figure 4.3: Score image of BB emission signal from the mono-like silicon ingot of wafer A-108 to A-45. The intensity is shown by the colour bar.

The PL emission signal with the energy of 0.875 eV is related to the defect D2 as stated by Drozdow [8]. After extracting the PL signal with related energy it is clear that this defect signal is the main defect signal at the seed junctions within the mono-like silicon ingot. As with D1, the D2 PL emission signal is concentrated in the centre of the seed junction. At the middle of the ingot the PL signal have small pixels with strong signal peaks around 1200 counted photons per pixel. Higher up in the ingot the strong peaks are diminished to around 800 counted photons per pixel, but the signal peaks flourish in the centre of seed junction 2.1 and 2.3 from the paper by Ekstrøm et al. [1]. The scatter effect is as with the D1 PL signal stronger with increasing height of the ingot. The extracted PL signal of D2 are shown in figure 4.7.

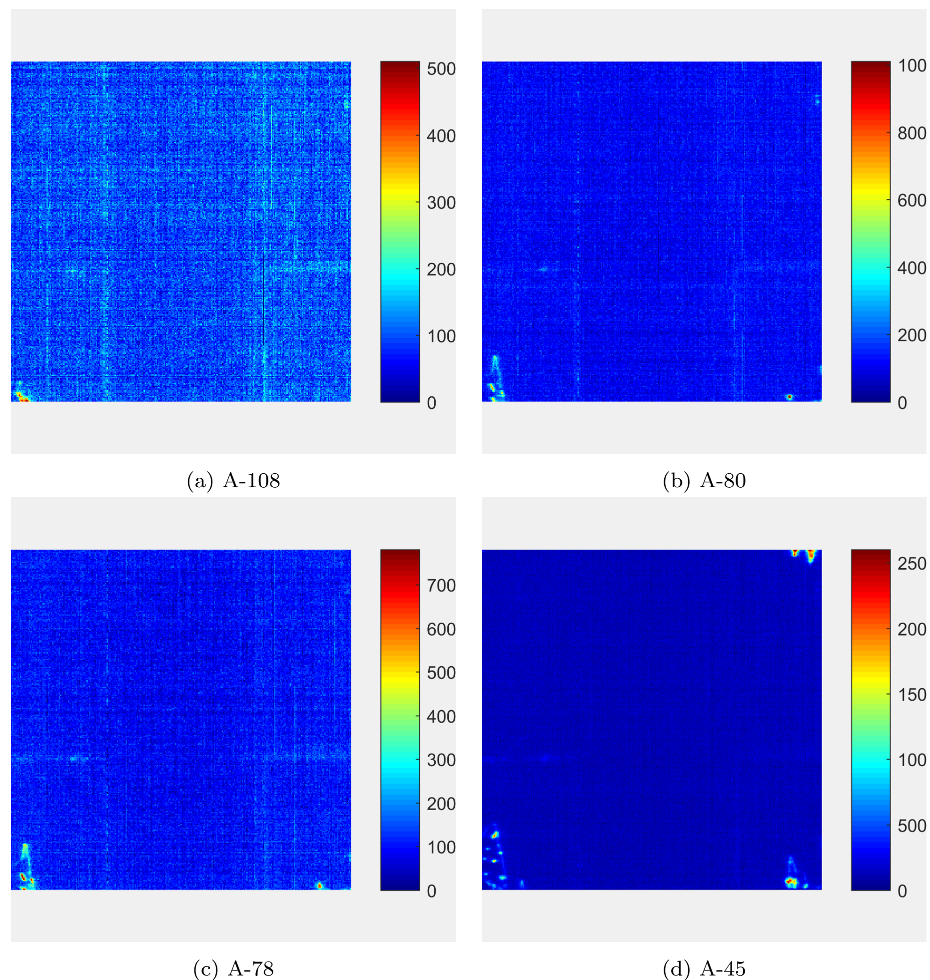

(a) A-108 (b) A-80

(c) A-78 (d) A-45

Figure 4.4: D07 PL emission signal from the mono-like silicon ingot of wafer A-108 to A-45. The intensity is shown by the colour bar.

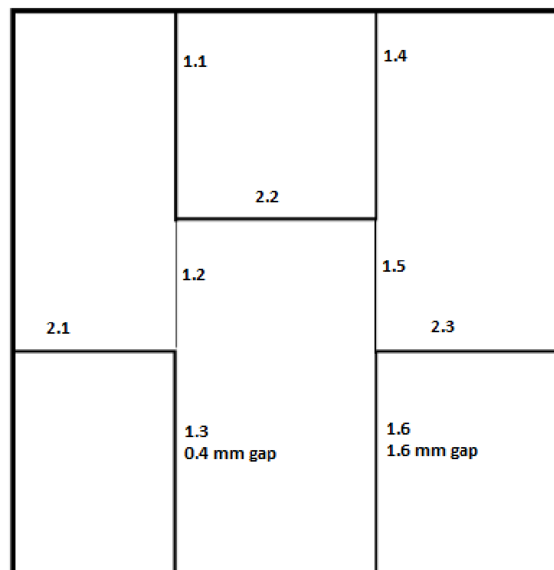

Figure 4.5: Seed junction explanation.

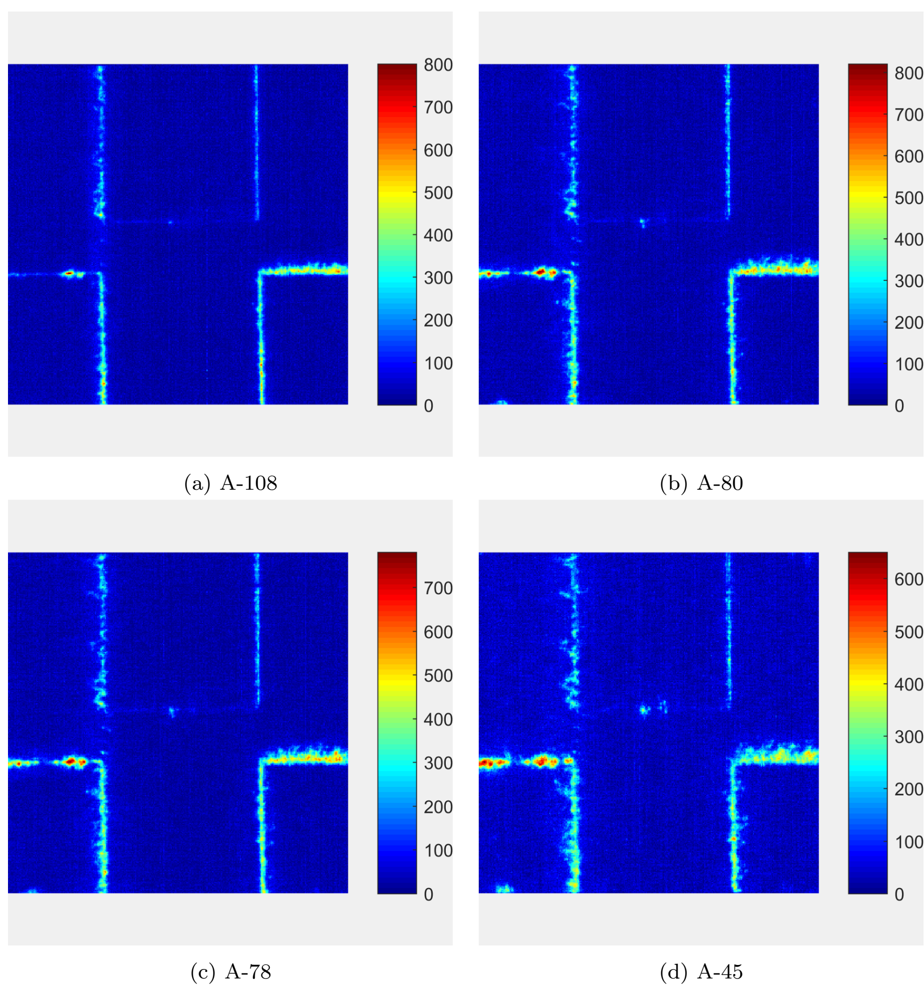

Figure 4.6: D1 PL emission signal from the mono-like silicon ingot of wafer A-108 to A-45. The intensity is shown by the colour bar.

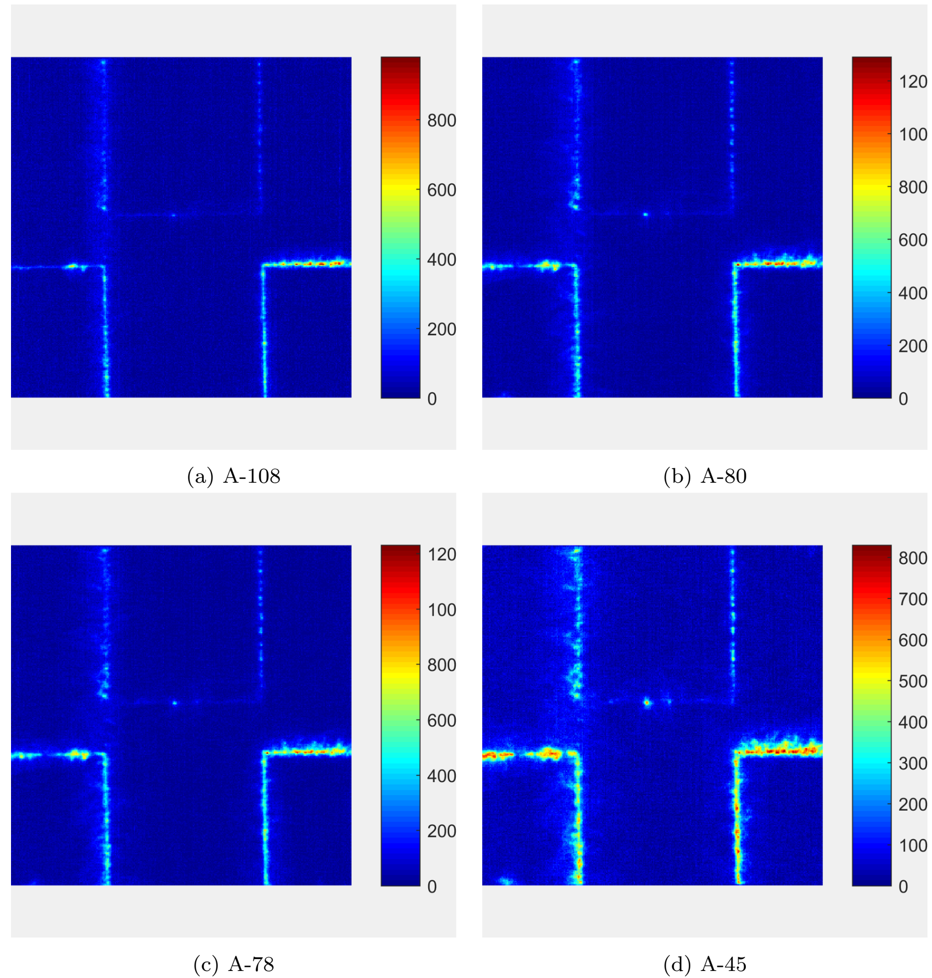

(a) A-108 (b) A-80

(c) A-78 (d) A-45

Figure 4.7: D2 PL emission signal from the mono-like silicon ingot of wafer A-108 to A-45. The intensity is shown by the colour bar.

With the PL emission signal of 0.934 eV, Drozdov et al. [8] named this signal the D3 emission signal. Examining all four images of the PL emission it is seen that the wafer A-108 is struggling with week emission signal. This is shown by examining the colour bar in figure 4.8. In the wafer A-108, D3 emission signal is concentrating around the centre of seed junction 2.3, this junction seems to be the most important seed junction and is discussed in section 4.3.4. In the other seed junctions, the D3 emission signal is weak or nearly non-existent. As the height of the ingot increases so is the signal strength. From somewhere before the middle of the ingot D3 PL emission signals is established in the seed junctions. Again it is a great difference in location of this signal, flourishing in seed junction 2.3 and non-existing in the 1.5 seed junction. The PL emission signal denoted VID3 with energy of 0.94 eV as seen in work by Flø et al. [11] is not found when checking with MCR plots.

The last PL emission signal found by Drozdov et al. [8], close to the BB signal was called D4. With an energy of 1.000 eV it is the strongest defect related signal (DRL). However, when examining figure 4.9 it is found with weak intensity. As with D3, the emission signal is gathering around the seed junction 2.3. At an elevated height in the ingot, seed junction 2.1 experience

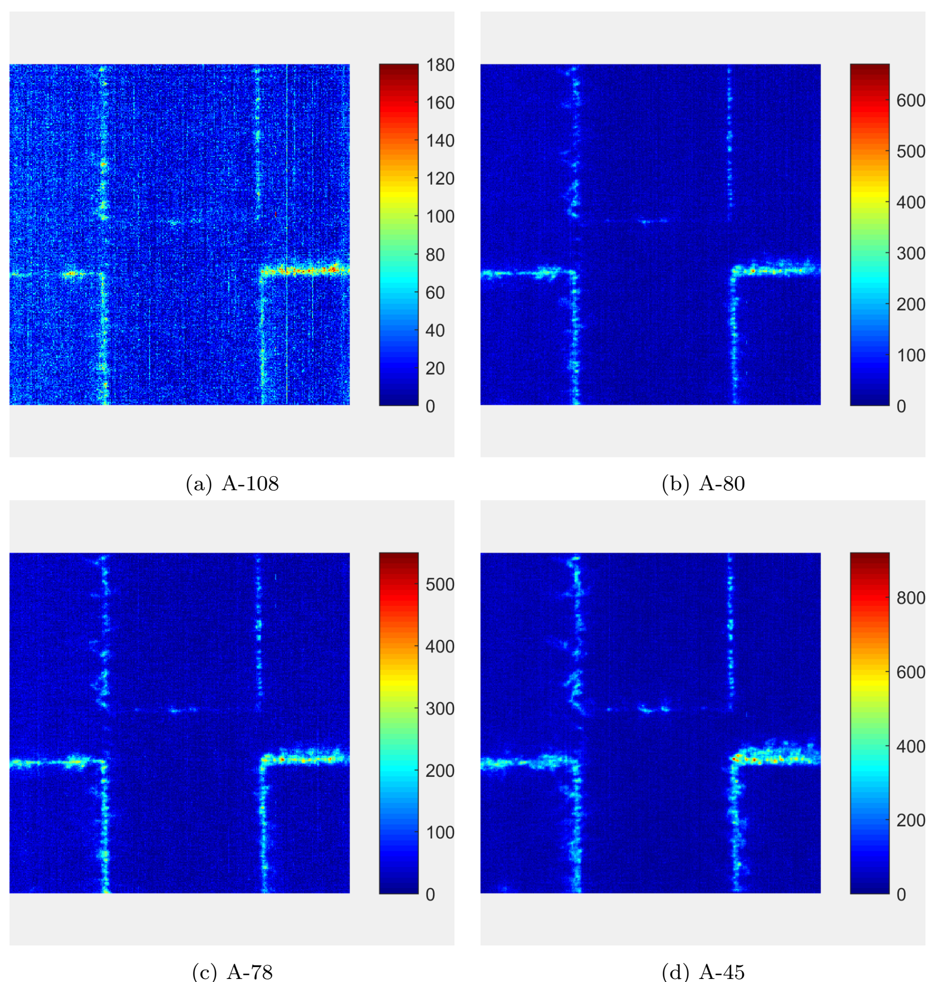

(a) A-108 (b) A-80

(c) A-78 (d) A-45

Figure 4.8: D3 PL emission signal from the mono-like silicon ingot of wafer A-108 to A-45. The intensity is shown by the colour bar.

some areas with increasing growth of the 1.000 eV PL signal. Like the D3, the D4 PL signal seems to grow into the silicon ingot with increasing ingot height.

4.2.2 Section discussion

In this experiment it was established that the intensity varies with wafers from different heights in the mono-like silicon ingot. Near the bottom, with wafer A-108, the signal intensity is weak, not only for the DRL signals, but for the BB alike. One exception is revealed, the D1 related signal has around the same intensity as D1 PL signal in A-80.

It is a well-known fact that red zones in silicon crystals are areas with electrons of low-lifetime span as mentioned by Nærland et al. [40]. Another study mentiones that low-lifetime signals at the bottom of a silicon ingot have relations to oxygen impurities precipitated from the crucible bottom [13]. The Cz-Si seed crystals are known to have more oxygen than mc-Si and as discussed in section 4.1.2 oxygen can be a factor.

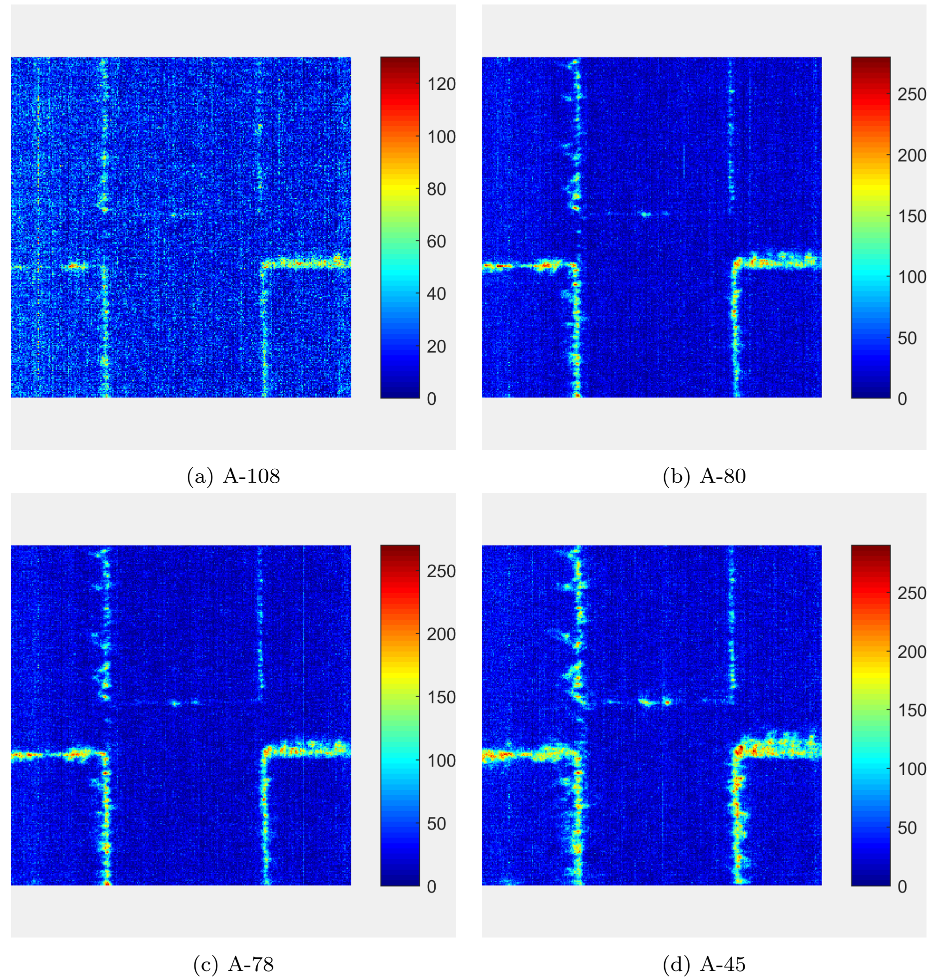

(a) A-108

(b) A-80

(c) A-78

(d) A-45

Figure 4.9: D4 PL emission signal from the mono-like silicon ingot of wafer A-108 to A-45. The intensity is shown by the colour bar.

In the middle of the ingot where A-80 and A-78 were cut from 53.3 mm and 54 mm respectly, the experiment established that the different signals are stronger there than near the bottom of the ingot. It seems that the possible oxygen related defects and red zone are diminishing with increasing height and give increased lifetime to the electrons as discussed in section 4.1.2. When investigating figure 4.4, it is clear that the parasitic crystals forming from the crucible wall are expanding deeper into the main silicon crystal as found by Ekstrøm et al. [1]. Nonetheless, it seems that the rogue crystals have not yet established themselves enough to do any real harm to the lifetime in the A-80 and A-78 wafer. A more accurate and comprehensive discussion around the D07 PL emission signal and its pairing with the rogue crystals is done in section 4.4.2.

Near the top of the silicon ingot a pattern is evolving. After increasing PL signal strength from bottom to middle of the ingot the BB PL signal are now diminishing. This can be explained by the enormous increase in D07 PL emission by over three times, as seen in the A-78 wafer which are the closest neighbour in this investigation. The rogue crystals have as seen in figure 4.4 grown into the main silicon ingot. Research is underway to establish if the D07 signal is

related to iron entering the ingot through rogue crystals from the crucible wall, again this will be discussed later. As for the D1 signal its intensity is halted and a decrease has occured through the complete ingot. Inspecting figure 4.6 it is clear that seed junction 2.1 is struggling with small high density defect related areas compared to the junction 2.3. On the other hand seed junction 2.3 have larger areas with more scattered D1 PL emission signal.

4.3 Investigation of the mono-seed junctions.

To the normal eye the four wafers examined in this experiment seems to be near mono crystal in appearance. In figure 4.10 a photograph of the A-78 wafer is shown alongside a figure of the seed junctions. Written next to the junction 1.3 and 1.6 are the manufactered gap width [1].

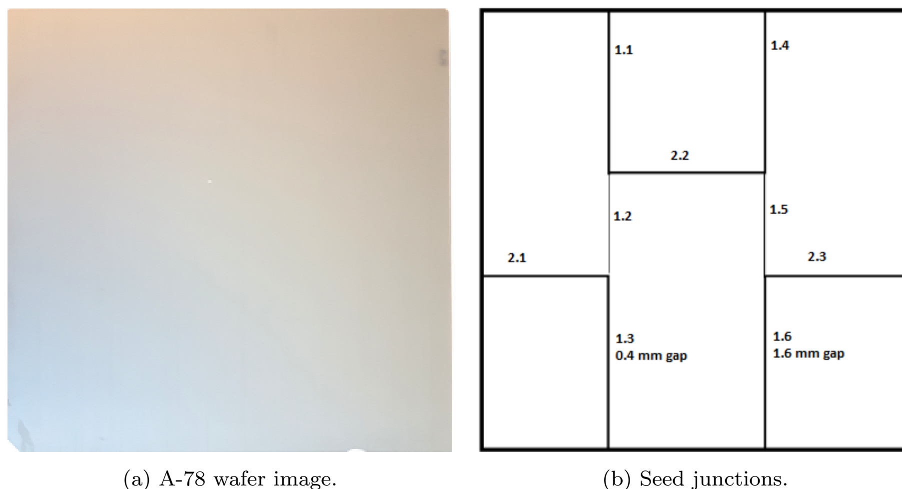

(a) A-78 wafer image. (b) Seed junctions.

Figure 4.10: A photograph of the A-78 wafer in a). In b) nine seed junctions numbered with gap width at junction 1.3 (0.4 mm) and 1.6 (1.6 mm).

With the photoluminescence (PL) emission signals the seed junctions between the mono-like silicon crystals are clearly shown as seen in figures in section 4.2.1. The work of Ekstrøm et al. [1] will be a main participant in this section. Tables with both DRL evolving through the ingot and a short summery of junction characteristics are shown in Appendix D. The establishment of the DRL through the silicon ingot will be investigated for the A-108, A-78 and A-45 wafer. Since the A-80 wafer is only 0.8 mm lower in the ingot than A-78, this wafer has not been thoroughly investigated.

4.3.1 A-108 seed junctions

Investigating the A-108 wafer with MCR resulted in D1 and D2 related PL emission signals. Closing in to the 1.1 seed junction, both MCR and Matlab investigation reveals PL signals related to D1 and D2. During the examination of the 1.1 junction a flaw in the MCR analysis was discovered. MCR is not trustworthy when used on small areas with weak signals. MCR extracts a signal of around 0.82 eV alongside multiple components in the near D2 area. As figure 4.11 shows, the analysis fails to give accurate information of the near D2 PL emission signal. Because of this investigation of the seed junctions at A-108 and A-78 wafer will be done with Matlab. Comparing the MCR load plot with Matlab code in figure 4.11 the combined D1 and

D2 related PL emission signal is found with a single apex of around 0.846 eV. The single peak in the middle of D1 and D2 emission signal can be related to close spatial location.

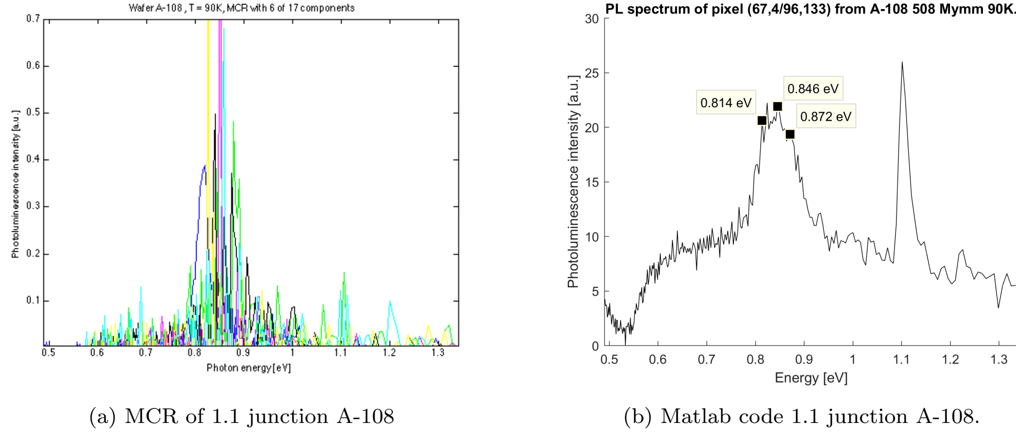

(a) MCR of 1.1 junction A-108

(b) Matlab code 1.1 junction A-108.

Figure 4.11: Both MCR and Matlab plots of junction 1.1 from A-108.

The behaviour of the seed junctions in the near bottom wafer A-108 are remarkable similar to each other. As shown in figure 4.12, 4.13 and 4.14, D1 and D2 PL emission signals are the two main components of each junction. It should be noticed that, as discussed in section 4.2.2 all of the PL emission signals in this wafer are weak, it maybe only the strongest DRL signals are captured by the camera.

Junction 1.1, 1.2, 1.3 and 2.1 share the same characteristics with a D1 and D2 related signal with a peak of 0.846 eV as seen in figure 4.12 and 4.14. This peak signal has been mentioned as D5 PL emission signal in a study by Pizzini et al. [23], thus it may be a superposition of the D1 and D2 PL signals. The indistinct flat peak can be related to the D1 and D2 PL signals being located close to each other. The 1.2 and 1.5 junctions are calm areas with not much DRL signals at all, as shown by the score figures in section 4.2.1. In fact, in 1.5 there is not much other PL signals other than band to band (BB). It seems that the preparation and laying the mono-like seeds up to each other have been successful. In junctions 1.4, 1.6 and 2.3 the D1 and D2 PL signals have clear and distinct apexes unlike in the 1.1-1.3 and 2.1 junctions, where the apexes are close and non-distinct. This may be related to the D1 and D2 PL emission signals being further from each other spatialy than in the junctions without distinct peaks.

The 1.3 and 1.6 seed junctions are unique in the way of intentionally being built with gaps, as given by Ekstroem et al. [1]. In the 1.3 junction, the gap is not wider than 0.4 mm and seems not to have any real harmful effect of the junction. Junction 1.3 share resemblance to junctions 1.1 and 2.1 with blunt apexes and same intensity. Junction 1.6 on the other hand, with a gap of 1.6 mm it should be enough room for the silicon melt to penetrate. If the silicon melt penetrates, the chance for clusters and dislocations to develop alongside small rogue crystals are obvious.

Figure 4.13 f) shows there are just the D1 and D2 PL signals established in the junction 1.6. It seems odd that the junction is relative calm and this will be discussed in section 4.3.4. A difference is the PL signal from D2 is stronger in intensity than D1 PL signal, which is shared only with the chaotic 2.3 junction as shown by the figure 4.14 f). This is the only location that has evolved D3 and D4 PL signals alongside the D1 and D2 PL signals. Why D3 and D4 have established themselves at this location instead of the 1.6 junction needs to be discussed in comparison with the paper from Ekstrøm et al. [1].

In the 2.1 and 2.2 junction it have developed a trait shared by these two junctions. From figure 4.3, the rosette is clearly seen by the blue areas with no BB emission signal. Investigation of the middle pixel in these rosettes are shown in figure 4.15.

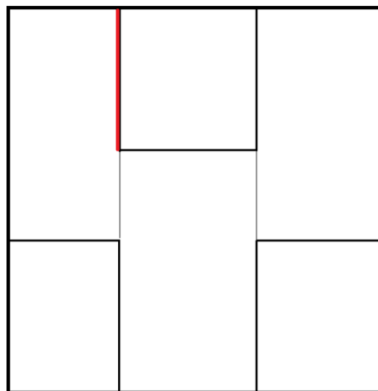

(a) Junction 1.1 A-108

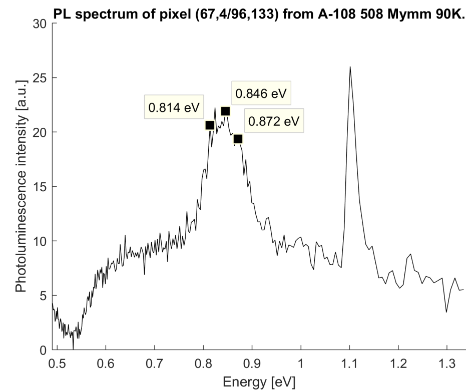

(b) Junction 1.1 A-108

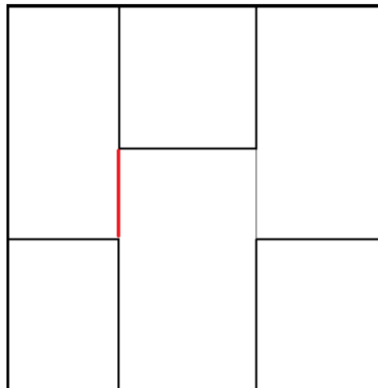

(c) Junction 1.2 A-108

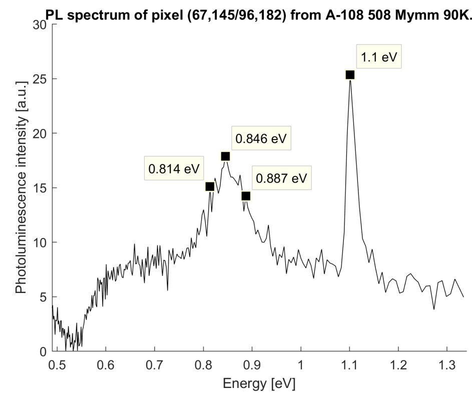

(d) Junction 1.2 A-108

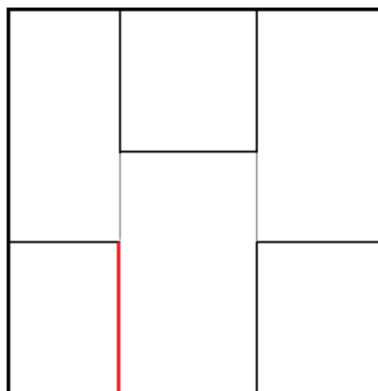

(e) Junction 1.3 A-108

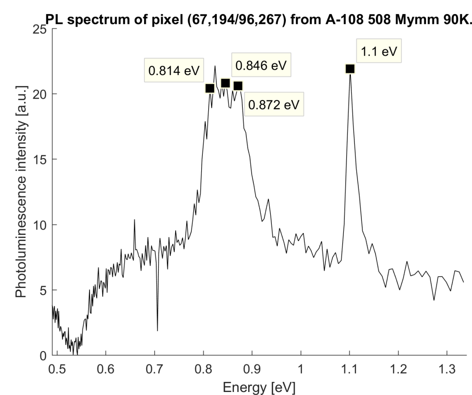

(f) Junction 1.3 A-108

Figure 4.12: 1.1-1.3 seed junctions in A-108, all figures have electronvolt on the x-axis and intensity on the y-axis.

The figure reveals the inside of the rosettes where D1 and D2 PL signals are found. Other than the rosettes, these two junctions are not similar. Junction 2.2 being calm, nearly without any DRL, and 2.1 being a more chaotic junction.

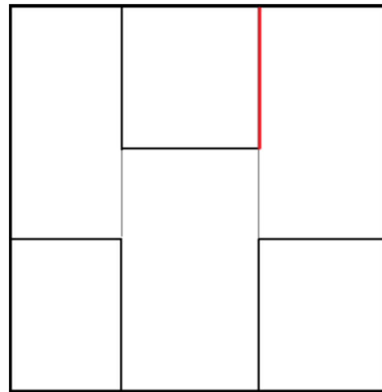

(a) Junction 1.4 A-108

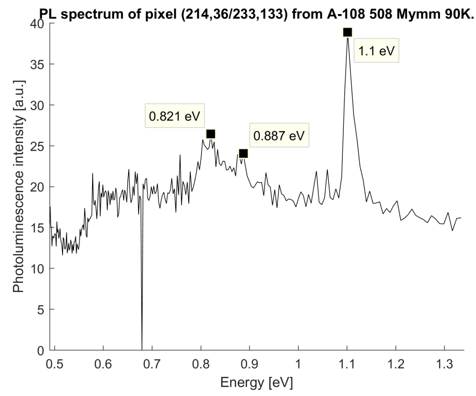

(b) Junction 1.4 A-108

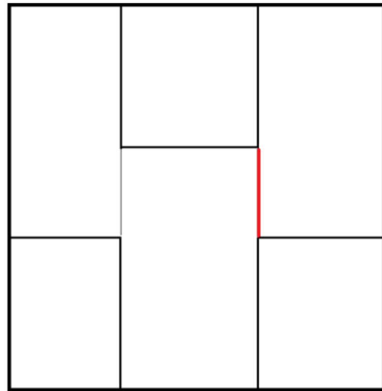

(c) Junction 1.5 A-108

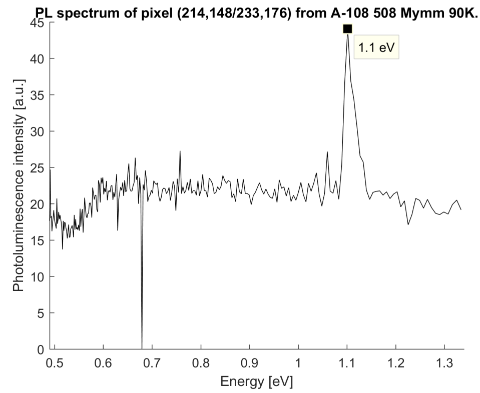

(d) Junction 1.5 A-108

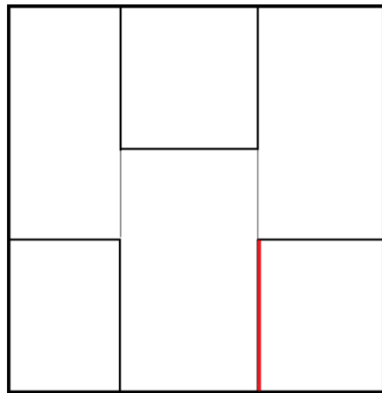

(e) Junction 1.6 A-108

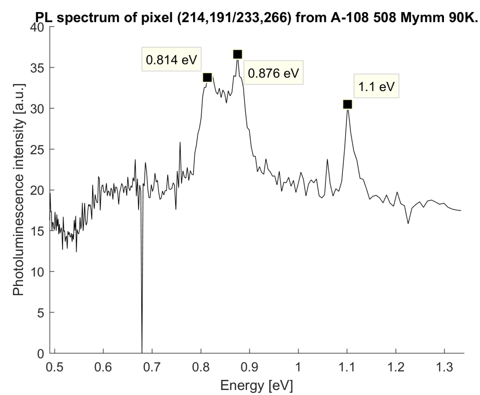

(f) Junction 1.6 A-108

Figure 4.13: 1.4-1.6 seed junctions in A-108, all figures have electronvolt on the x-axis and intensity on the y-axis.

Ekstrøm et al. [1] interpreted the rosettes as dislocations formed by the weight of the silicon feedstock.

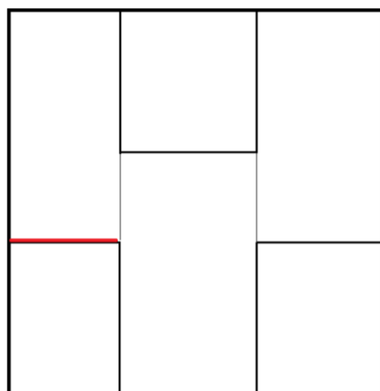

(a) Junction 2.1 A-108

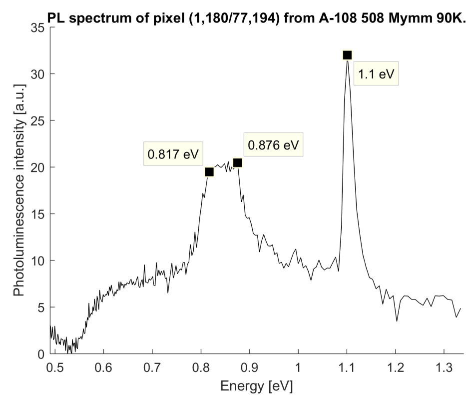

(b) Junction 2.1 A-108

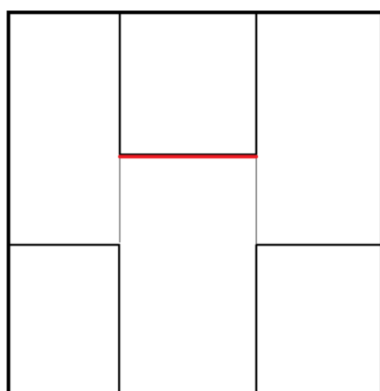

(c) Junction 2.2 A-108

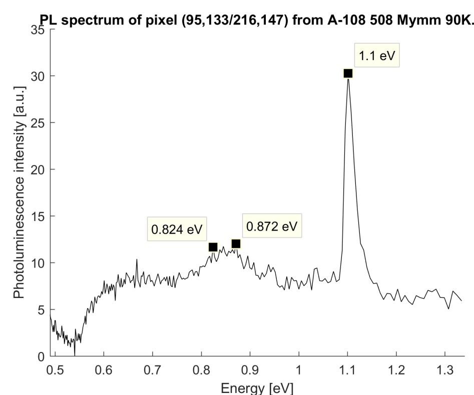

(d) Junction 2.2 A-108

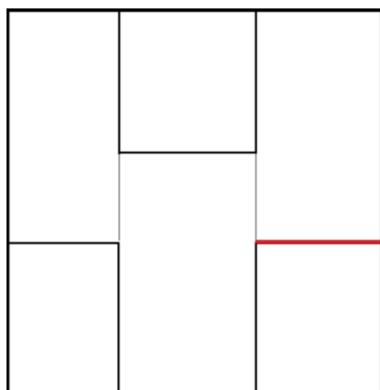

(e) Junction 2.3 A-108

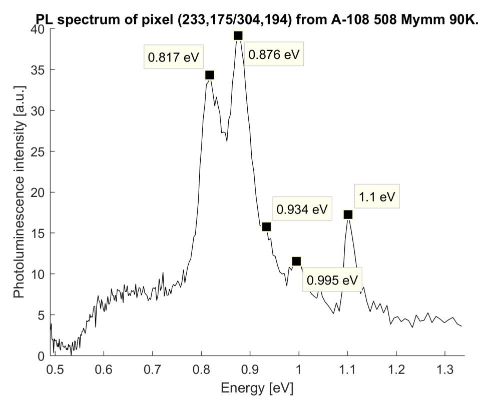

(f) Junction 2.3 A-108

Figure 4.14: 2.Y seed junctions in A-108, all figures have electronvolt on the x-axis and intensity on the y-axis.

The rosettes found in A-108 seem to trap D1 related impurities very well and is found to be

the largest reason of PL emission signal in the rosettes, with D2 PL emission signal as the second signal.

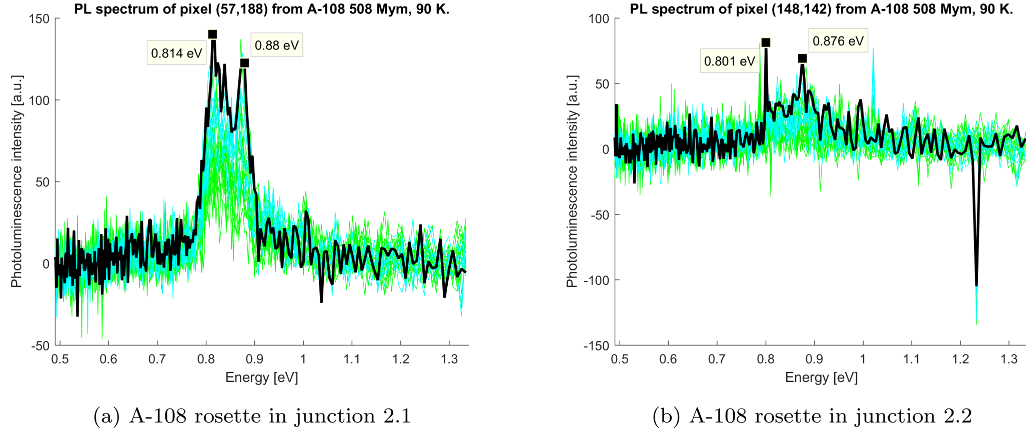

(a) A-108 rosette in junction 2.1

(b) A-108 rosette in junction 2.2

Figure 4.15: In seed junction 2.1 a rosette is discovered, figure a) showing spectrum at the center pixel in the rosette. In seed junction 2.2 there is another rosette and the spectrum in the center pixel are shown in figure b). In the pixelplot black curve is the chosen pixel, cyan curve is the neighbour pixels and the green curve is all the pixels that are two pixels away.

4.3.2 A-78 seed junctions

At the height of 54 mm, A-78 has been cut from the middle of the mono-like silicon ingot. As shown in the figure 4.16, 4.17 and 4.18 it is established that the A-78 wafer has other characteristics than the A-108.

Junction 1.1, 1.3, 1.6, 2.1 share most of the same traits. The D2 PL signal is increased in strength and at these junctions it is clearly stronger than the D1 PL signal. The D1 PL signal seems to have stopped growing and lingers around the same intensity as in A-108. An explanation to this could be that the impurity causing the D1 PL emission signal has for the most part entered the junction at a low height, while the impurity causing the D2 PL emission signal still is collected by the junctions as the main ingot solidifies. In these junctions the D3 PL emission signal has been established, this was not seen in the A-108 wafer, except junction 2.3. The signal is not more than a knee on the graph in all of these junctions, but it is clearly there. The D4 PL emission signal has grown in intensity to form a single peak in the figures, while maintaining a smaller intensity than the D3 PL signal.

The junction 1.2 does not seem to have changed in shape or intensity. It seems that the junction has not collected any more impurities with the growth of the silicon crystal. As for the 1.5 junction, it is clear that the two seeds are perfectly matched and almost none of the impurities have gathered here. A closer inspection, however, reveals a small peak of a new 0.904 eV signal. Another calm junction is the 2.2 with the rosettes as mentioned in section 4.3.1. This junction has nearly no differences from the A-108 wafer and that can be related to the rosettes. It seems the rosettes are the only thing that are collecting impurities in this junction and that leaves a small area where impurities are drawn to.

As seen in figure 4.14, the junction 2.3 was a chaotic location already filled with D1-D4 PL emission signals, here at the middle of the ingot as shown in figure 4.18 there have occured some changes. Again, it is established that the D1 related PL emission signal have stopped growing

and seems to linger just a little higher than in the A-108 wafer. This is the same development as in the 1.1, 1.3, 1.6 and 2.1 junctions for the D1 signal in the A-78 wafer.

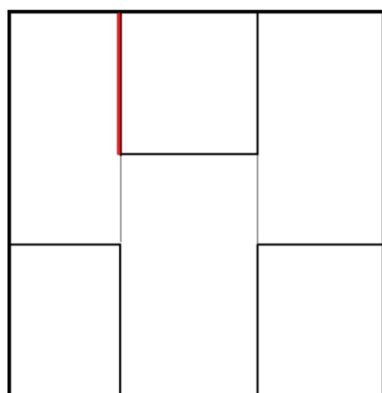

(a) Junction 1.1 A-78

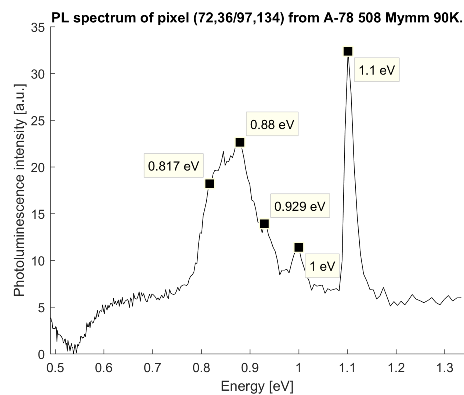

(b) Junction 1.1 A-78

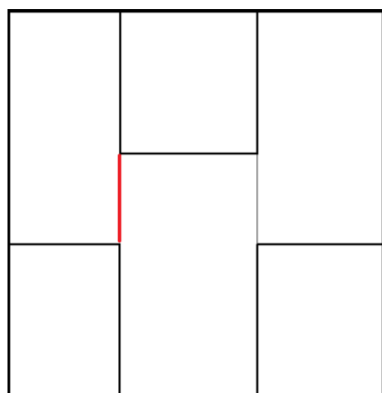

(c) Junction 1.2 A-78

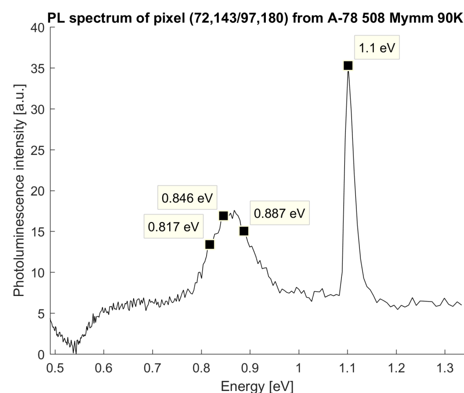

(d) Junction 1.2 A-78

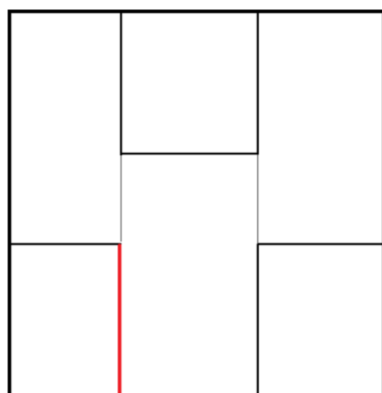

(e) Junction 1.3 A-78

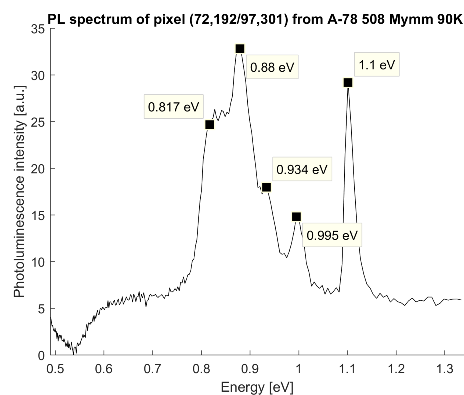

(f) Junction 1.3 A-78

Figure 4.16: 1.1-1.3 seed junctions in A-78, all figures have electronvolt on the x-axis and intensity on the y-axis.

It is also established that the D2 related PL emission signal has grown stronger, the same applies for both the D3 and D4 related PL emission signals. This behaviour of the D1 and D2 have been discussed in 4.1.2.

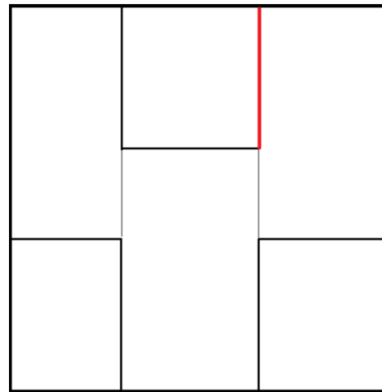

(a) Junction 1.4 A-78

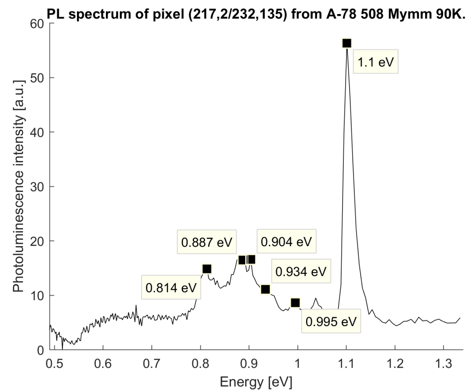

(b) Junction 1.4 A-78

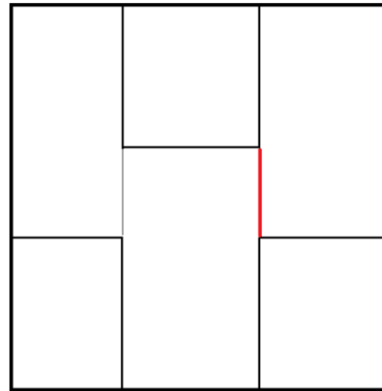

(c) Junction 1.5 A-78

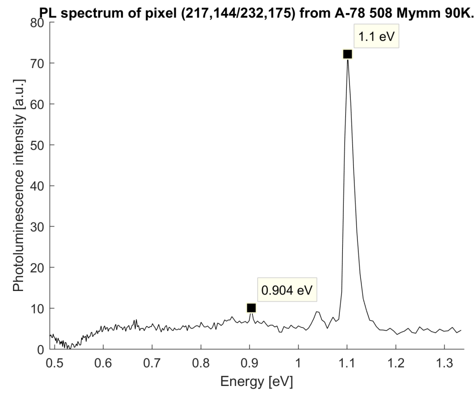

(d) Junction 1.5 A-78

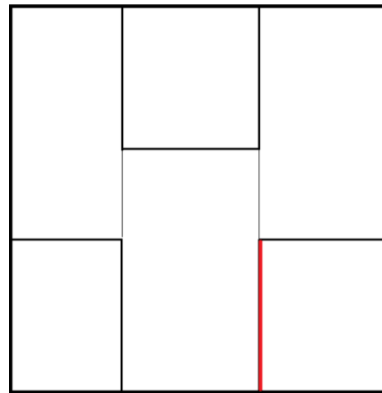

(e) Junction 1.6 A-78

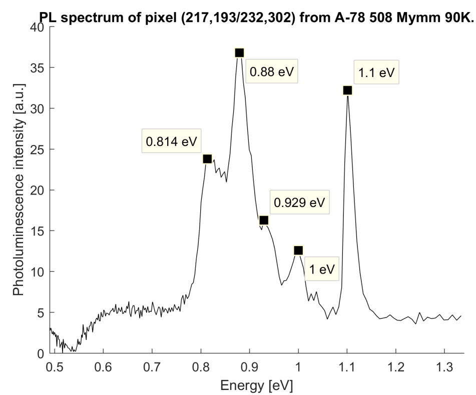

(f) Junction 1.6 A-78

Figure 4.17: 1.4-1.6 seed junctions in A-78, all figures have electronvolt on the x-axis and intensity on the y-axis.

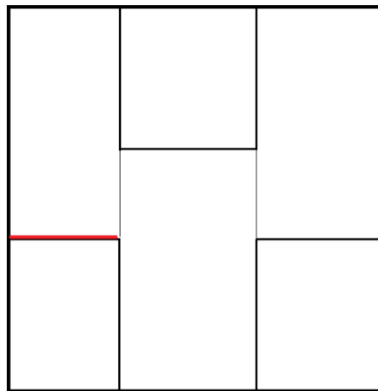

(a) Junction 2.1 A-78

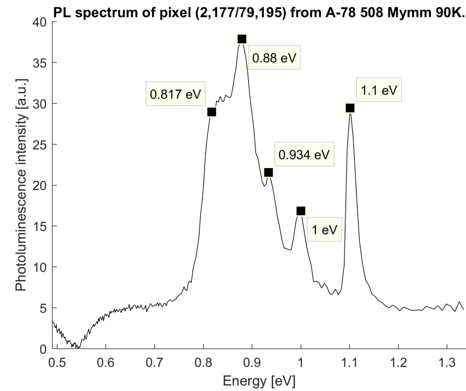

(b) Junction 2.1 A-78

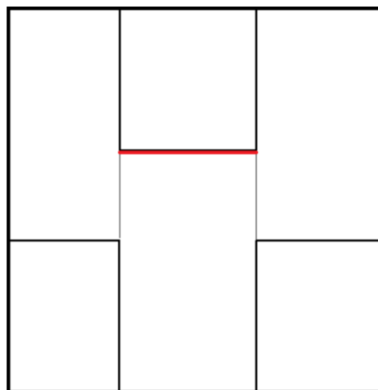

(c) Junction 2.2 A-78

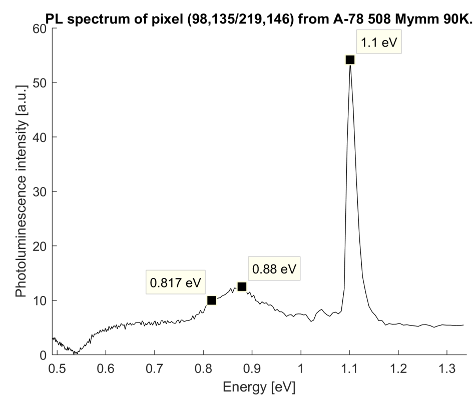

(d) Junction 2.2 A-78

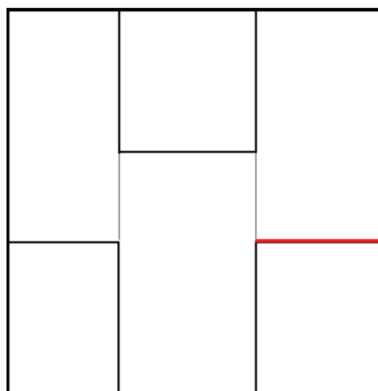

(e) Junction 2.3 A-78

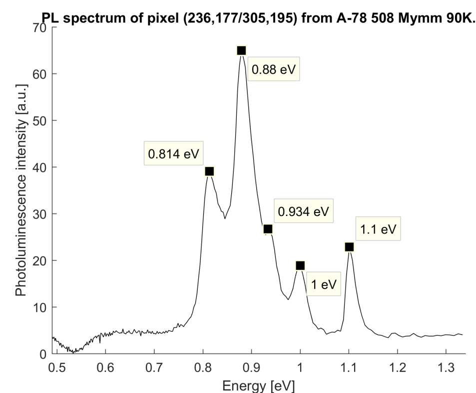

(f) Junction 2.3 A-78

Figure 4.18: 2.Y seed junctions in A-78, all figures have electronvolt on the x-axis and intensity on the y-axis.

Another calm location is the 1.4 junction, the intensity of the DRL signals from D1 and D2 are at the same level and separated from each other. It seems that these two defects are not so closely located to each other than in other junctions. A small knee in the graph of figure 4.16

b) is visualized and is recognized as the D3 PL signal. As with the D4 related PL signal, these two signals are hardly noticeable. On the other hand the new PL emission signal at 0.904 eV is established here as well as in the junction 1.5. It is interesting that a new PL signal, which is not mentioned in the literature, is forming with exactly the same energy in two different places.

An interesting behaviour of the D2 PL emission signal it seems to increase in strength, more than the normally stronger D1 PL emission signal as discussed in 4.1.2. When examining the rosettes in junction 2.1 and 2.2, it is established that this is correct here as well. In figure 4.19 the result of the investigation in junction 2.1 is revealed. There are two rosettes in this junction, the largest is shown in figure 4.19 a) and b) and the new smaller rosette in c). The characteristics of both rosettes are strong DRL, increased D2 PL signal than in A-108, a small reduction in intensity for the D1 PL signal and an introduction of the D3 and D4 PL signals.

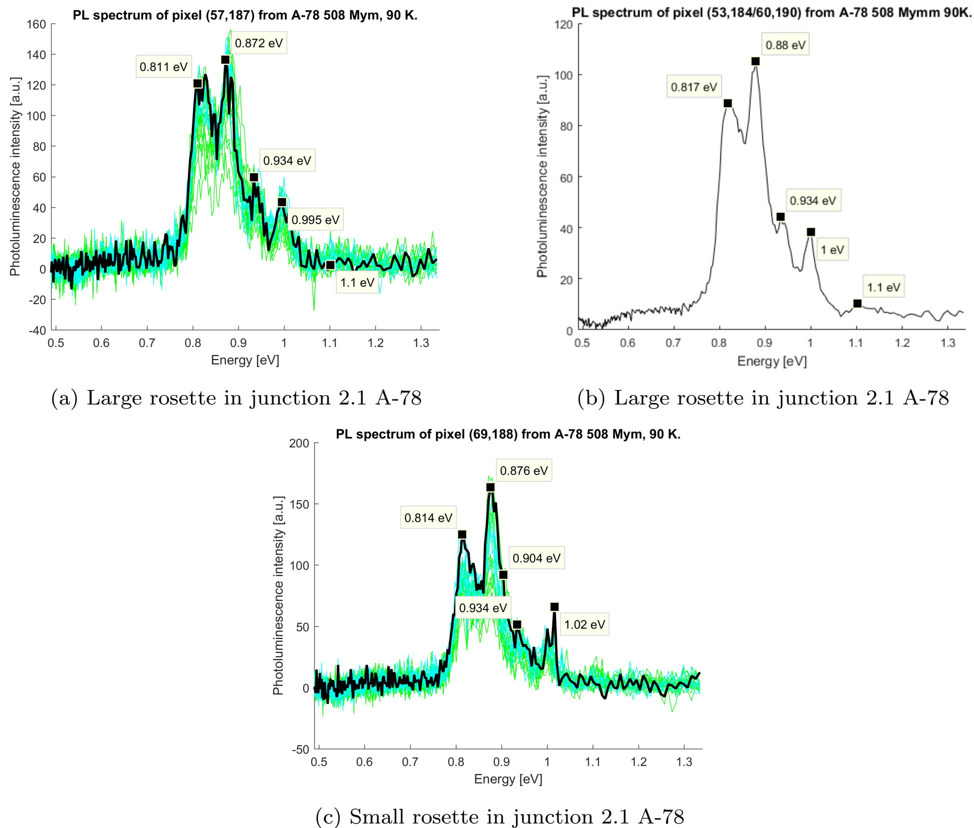

(a) Large rosette in junction 2.1 A-78

(b) Large rosette in junction 2.1 A-78

(c) Small rosette in junction 2.1 A-78

Figure 4.19: In seed junction 2.1 two rosette are evolving from A-108, figure a) showing spectrum at the center pixel in the rosettes and an integrated spectrum of the largest in b) and spectrum of the smallest rosette in c). In the pixel plot black curve is the chosen pixel, cyan curve is the neighbour pixels and the green curve is all the pixels that are two pixels away.

When examining the junction 2.2 rosettes, it could be easy to conclude that the D2 PL emission signal had increased with the height, would be found at this location. As shown in figure 4.20 this is not the fact. It is clear to see that the D2 PL signal is present in the rosette as a near single defect. D1, D3 and D4 PL emission signals are found, but are weak signals compared to the D2 PL signal. The new and much smaller rosette seen in figure 4.20 b) does

not have D2 PL signal at all, only D1 and D3 PL signals alongside the new 0.9 eV PL signal. This new rosette is quite small and should increase both in intensity and area as the main silicon ingot solidifies further. The different characteristics of the rosettes in 2.1 and 2.2 junctions need to be addressed and compared to the work of Ekstrøm et al. [1] on how junctions are generated.

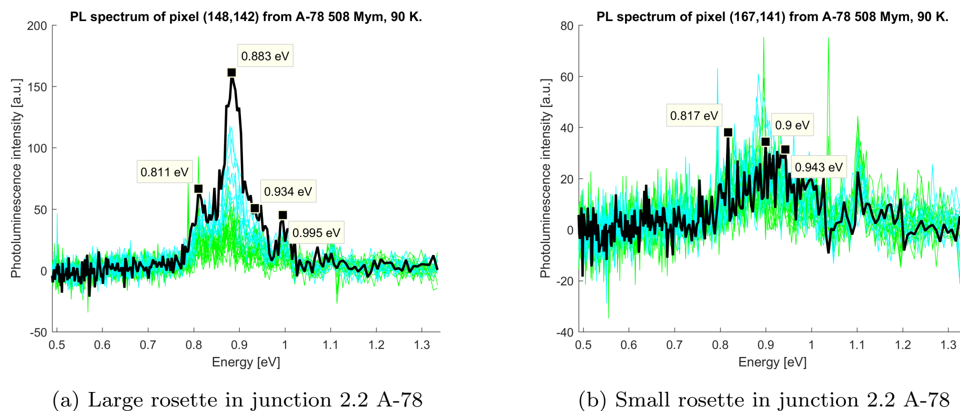

(a) Large rosette in junction 2.2 A-78

(b) Small rosette in junction 2.2 A-78

Figure 4.20: In seed junction 2.2 two rosettes are discovered, figure a) showing spectrum at the center pixel of the largest rosette to the left and b) center pixel of the smallest to the right. In the pixel plot black curve is the chosen pixel, cyan curve is the neighbour pixels and the green curve is all the pixels that are two pixels away.

4.3.3 A-45 seed junctions

In A-45 interesting behaviours are expected in the junctions, based on the results from A-108 and A-78. In figures 4.21-4.29 the results from all the A-45 junctions are given. Comparing Matlab with MCR analysis is done to submit a stronger case on the traits in each of the nine junctions. As in section 4.1.1, 17 components MCR algorithm is used and the relevant components are shown in the figures.

The seed junction 1.1 is found with all the known D1-D4 emission signals. A slight increase in the D2 emission signal is observed with a small shift in energy from 0.8 eV to 0.833 eV. The D1 PL emission signal has diminished even further from the A-78 wafer, as seen in other junctions in this wafer. D3/D4 PL emission signals have grown in intensity. D3 PL signal is at this junction grown stronger in intesity than the D1 PL signal.This is given in figure 4.21 and This is interestingly because of the impurity based discussion in section 4.1.2.

When investigating the 1.2 junction with Matlab it seems that the D1 PL signal has disappeared entirely. Comparing to the MCR analysis this statement seems to hold. The reduction of D1 has been seen through the ingot as the silicon solidifies with elevated height. D3 and D4 PL signals have been established in this junction as well as seen from both Matlab and MCR figure in 4.22, MCR treats this component as one like in section 4.1.1. MCR also extracts a signal at 0.849 eV, but it is difficult to interpret this as a PL signal of its own.

Junction 1.3 is an interesting junction because of the 0.4 mm gap made intentionally. Again, as seen throughout the solidification process in the ingot, the D2 PL signal increases while the D1 signal either halts or decreases as shown in figure 4.23. Comparing this result to the MCR analysis, it seems to be relatively accurate. The D3 and D4 PL signals are also here treated as one component, and it seems that this behaviour is general in the A-45 wafer. Interestingly, MCR extracts the 0.9 eV signal, which is the second largest DRL signal in this junction after D2.

This can be seen by the legend bar in figure 4.23, however, the signal has an increased energy and is seen at 0.919 eV.

In A-78 at junction 1.4, the new PL signal of 0.9 eV was seen as an equal to the D2 PL signal. At the A-45 wafer the 0.9 eV was found with increased intensity. As the 0.9 eV signal increases, the D1 PL emission signal has stopped growing. D3 and D4 PL signal have like the 0.9 eV component increased in intensity. This is given in the figure 4.24. Comparing to the MCR analysis, the 0.9 eV is a small component found as well. Interestingly the MCR analysis do not find any D1-D4 PL emission signals, whereas it found D3 and D4 PL emission signal at the similar 1.2 junction.

Junction 1.5 has to be a great success on the account of the preparation and placing of the mono-like seed crystals. As shown in figure 4.25, small amounts of D1 and D2 PL emission signals are present, close to the intensity as the rest of the signals near the zero intensity line.

The last of the 1.X junction is 1.6, here the interesting part, a gap of 1.6 mm was made placing the mono-like seed crystals. As for the rest of the junctions discussed the D1 PL emission signal is decreasing from the A-78 wafer.

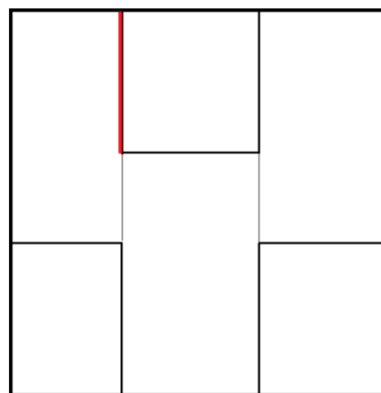

(a) Junction 1.1 A-45

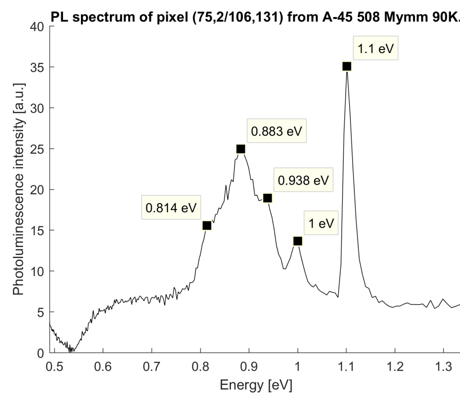

(b) Junction 1.1 A-45

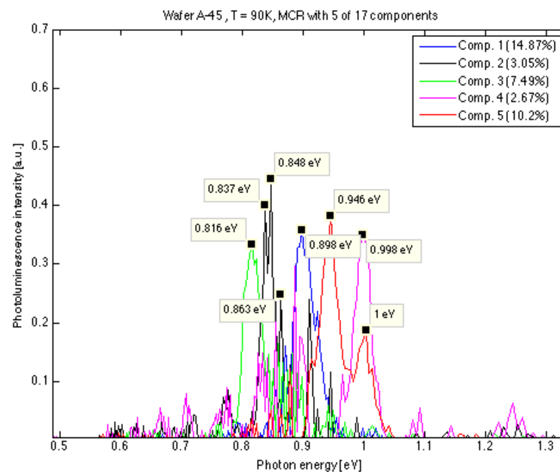

(c) Junction 1.1 A-45 MCR

Figure 4.21: Seed junction 1.1 at the A-45 wafer.

An interesting topic seems to be that the D2 PL emission signal also decreases while the new 0.9 eV emission signal is at a halt. Only D3/D4 PL emission signals are increasing. As stated by the work of from Ekstrøm et al. [1], the reason for the dislocations in this junction should be placed on rogue poly-crystals forming in the gap. No void is found from the junction against the crucible bottom, indicating silicon melt has penetrated all the way down to the bottom of the seed crystals. This on the other hand gave expectations that the D07 emision signal would form, but this has not been found. Investigating the MCR analysis in figure 4.26, the correlation with Matlab can be seen. An interesting fact is that the D3/D4 PL signals are once again treated as the same component.

The rosettes will now be addressed and investigated. As shown in figure 4.30 a), the D2 related PL emission signal is strongest, with a decrease in the D1 related PL signal, as seen many times in this and the A-78 wafer.

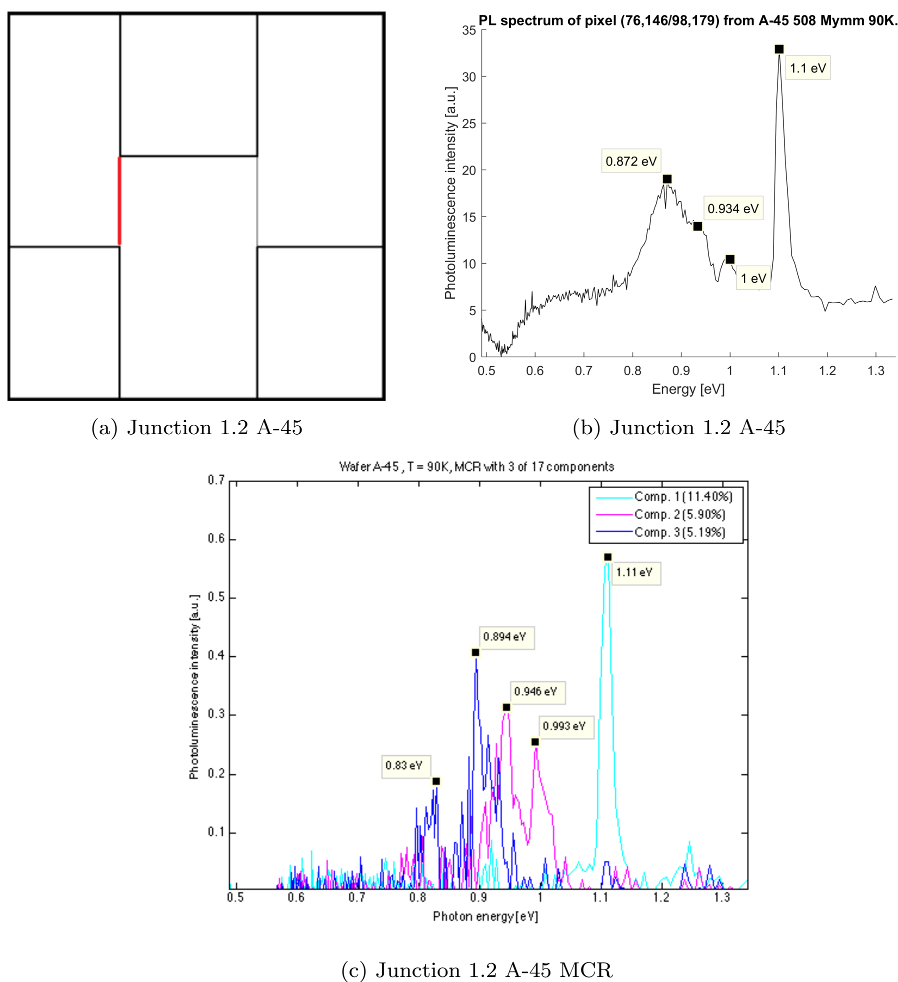

(a) Junction 1.2 A-45

(b) Junction 1.2 A-45

(c) Junction 1.2 A-45 MCR

Figure 4.22: Seed junction 1.2 at the A-45 wafer.

D3 and D4 related PL signals seem to have halted. In the pixel plot in figure 4.30 b), a near replica of the figure a) is seen. To the right of the large rosette, about 10 pixels on the x-axis, a

minor rosette formed, as seen in junction A-78. Examining this rosette in A-45 also results in a strong D2 with again decreasing D1 related PL signal.

It seems that the D2 PL signal can be the significant impurity when dislocations forms as a rosette in this junction. When investigating the rosettes in the 2.2 junction it is clear that the D2 PL signal is the main contributor to the DRL in the rosette, as seen in figure 4.31.

Junction 2.1 has similar traits as the junction 1.6 with a strong and increasing D2, D3/D4 and decreasing D1 PL emission signals, as shown in the figure 4.27. At the D2 PL signal apex the new PL signal of 0.9 eV is seen as a knee. In the MCR figure 4.27 a lot of components are extracted from 0.8-1.0 eV, which are difficult to relate to a single signal. In addition to D1-D4 related PL signal, the 0.84 eV, known as D5, and 0.9 eV PL emission signals are established. Junction 2.1 is a chaotic area and may be related to the rosettes or the non-elongating dislocations addressed in the work by Ekstrøm et al. [1].

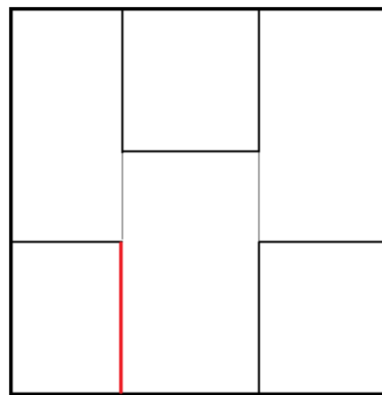

(a) Junction 1.3 A-45

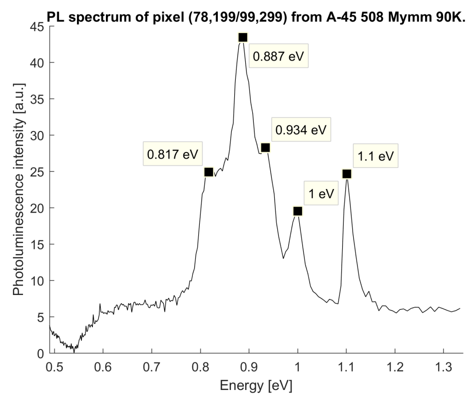

(b) Junction 1.3 A-45

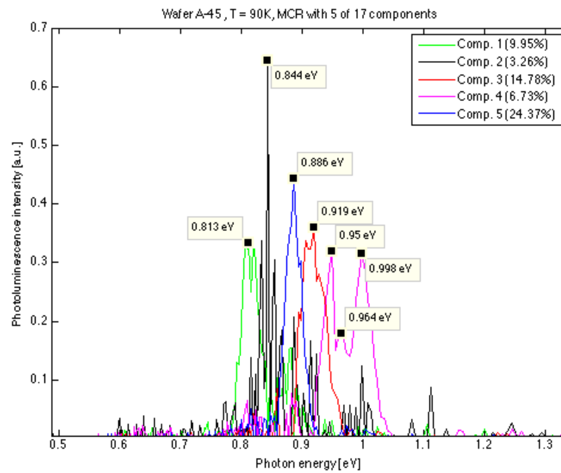

(c) Junction 1.3 A-45 MCR

Figure 4.23: Seed junction 1.3 at the A-45 wafer.

Another junction with rosettes is the junction 2.2, as mentioned when investigating the A-108 and A-78 wafer. Other than a slight increase in intensity of the DRL, and having D3 and D4

PL signals as small knees in figure 4.28, the junction has not evolved much from the A-78 wafer height. It can be discussed if the new 0.9 eV signal is found here hidden, twisting the apex toward a higher energy of 0.887 eV than the normal D2 PL signal at 0.875 eV. The results from the MCR give a clear PL signal of D3 and D4 and the strong component at 0.886 eV, which can be related to D2 PL emission signal or the new 0.9 eV signal.

Last investigated in the A-45 wafer is the junction 2.3. From the score images in section 4.2.1 this is one of the most chaotic junctions in the wafer. Surprisingly there are not much differences in the Matlab figures 4.18 f) and 4.29, other than an increased D3 PL signal now found as a knee higher up on the D2 peak. MCR analysis confirms the expectation of a chaotic junction with D1-D4 PL signals, showing two different signals, which can be related to the D3 defect. The 0.9 eV PL signal is also present and will be discussed later in the current work alongside the PL signal around 0.84 eV, referred to as D5. In the work by Pizzini et al. [23], the D5 PL signal is suggested to be related to dislocations with oxygen impurities. Another explanation is that the signal may be related to superposition by D1 and D2 PL signals.

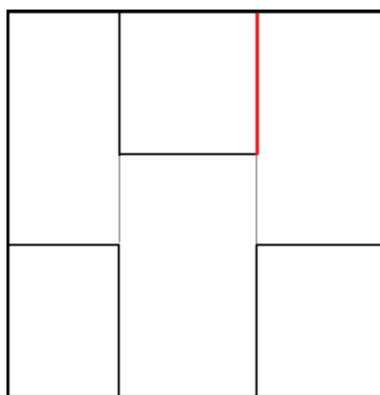

(a) Junction 1.4 A-45

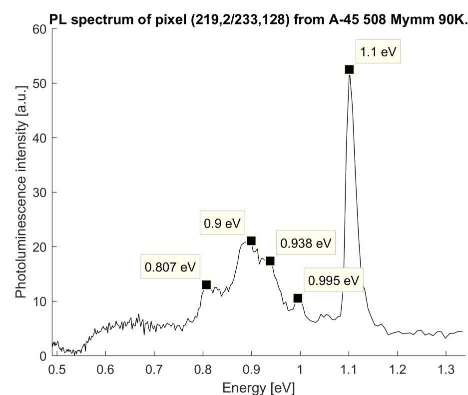

(b) Junction 1.4 A-45

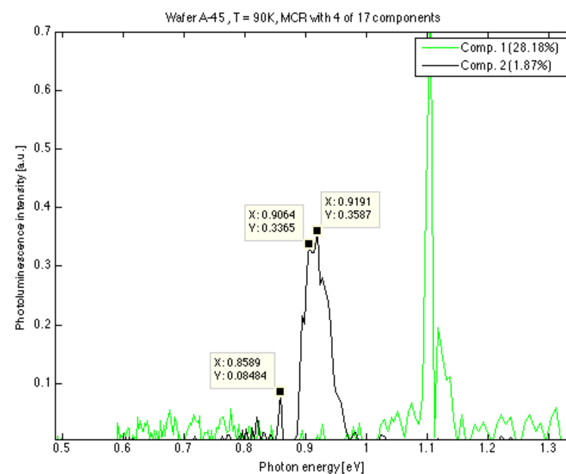

(c) Junction 1.4 A-45 MCR

Figure 4.24: Seed junction 1.4 at the A-45 wafer.

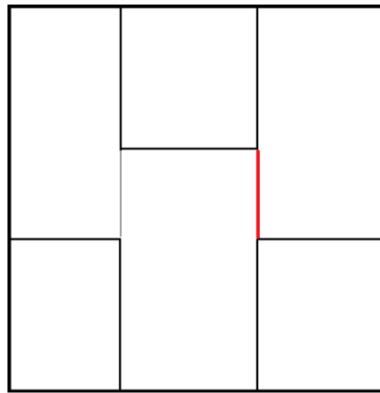

(a) Junction 1.5 A-45

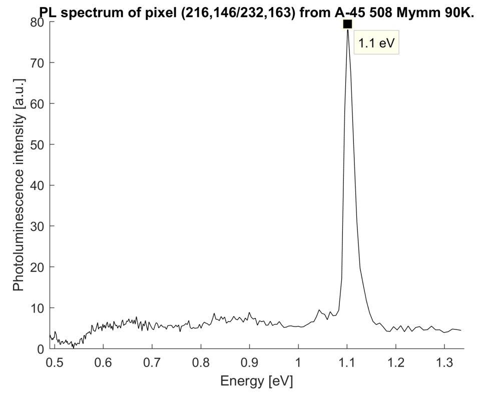

(b) Junction 1.5 A-45

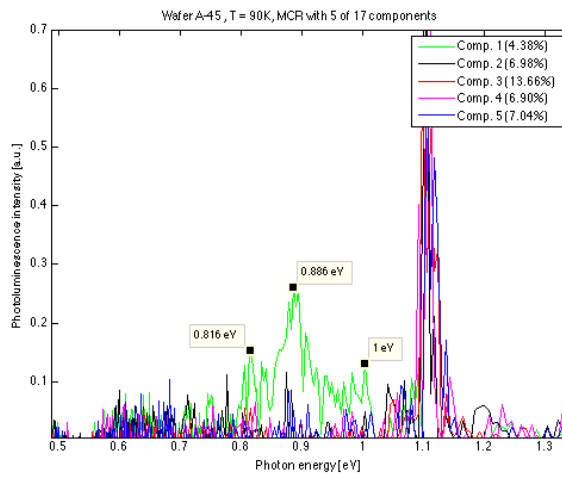

(c) Junction 1.5 A-45 MCR

Figure 4.25: Seed junction 1.5 at the A-45 wafer.

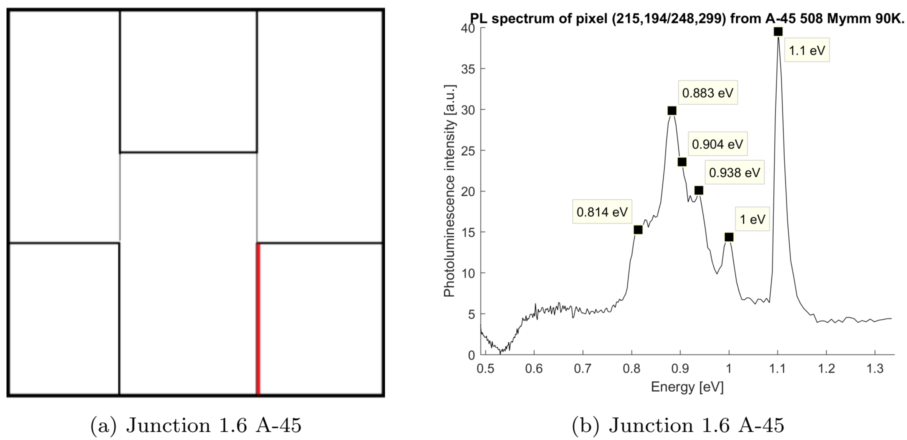

(a) Junction 1.6 A-45 (b) Junction 1.6 A-45

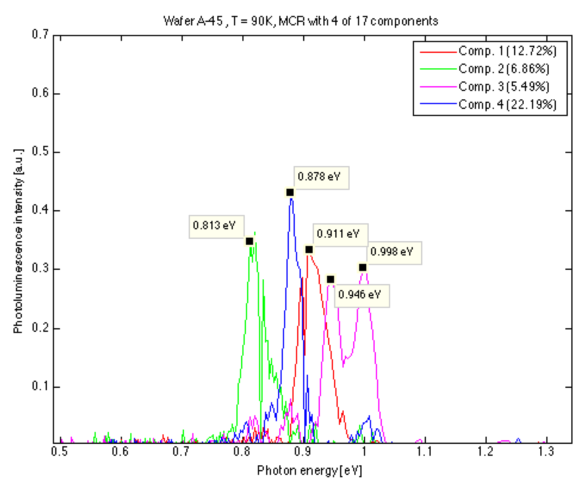

(c) Junction 1.6 A-45 MCR

Figure 4.26: Seed junction 1.6 at the A-45 wafer.

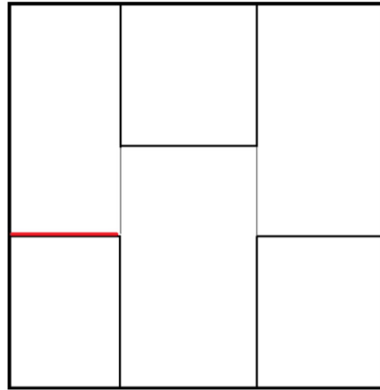

(a) Junction 2.1 A-45

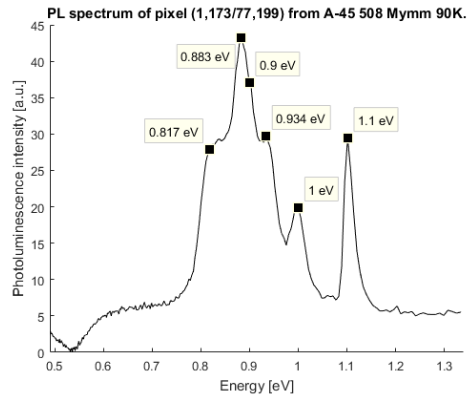

(b) Junction 2.1 A-45

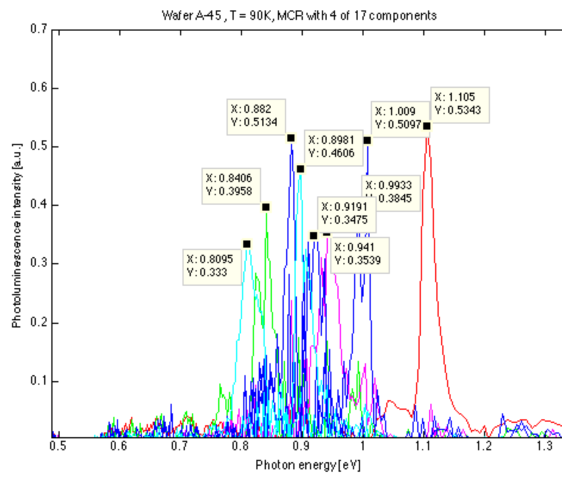

(c) Junction 2.1 A-45 MCR

Figure 4.27: Seed junction 2.1 at the A-45 wafer.

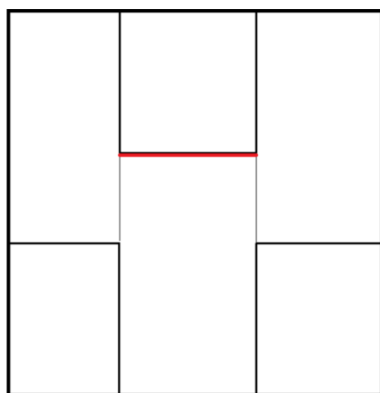

(a) Junction 2.2 A-45

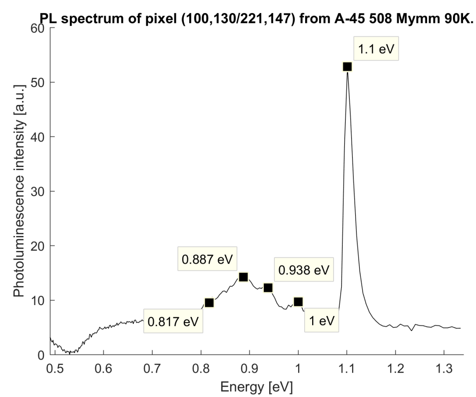

(b) Junction 2.2 A-45

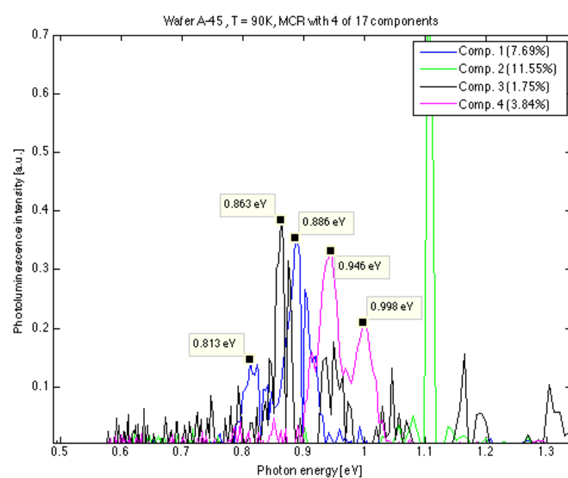

(c) Junction 2.2 A-45 MCR

Figure 4.28: Seed junction 2.2 at the A-45 wafer.

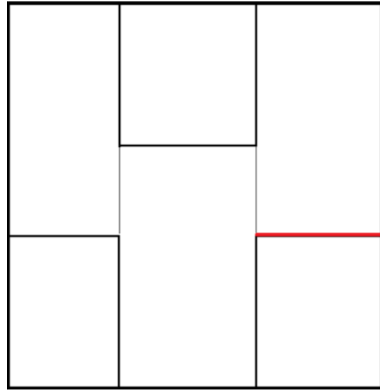

(a) Junction 2.1 A-45

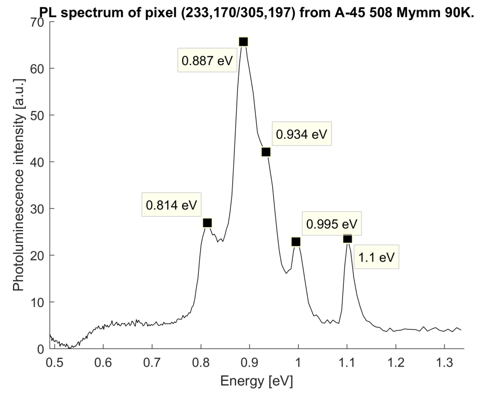

(b) Junction 2.1 A-45

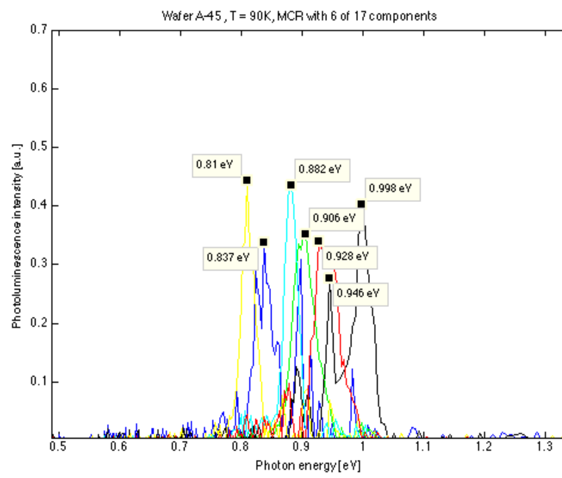

(c) Junction 2.1 A-45 MCR

Figure 4.29: Seed junction 2.3 at the A-45 wafer.

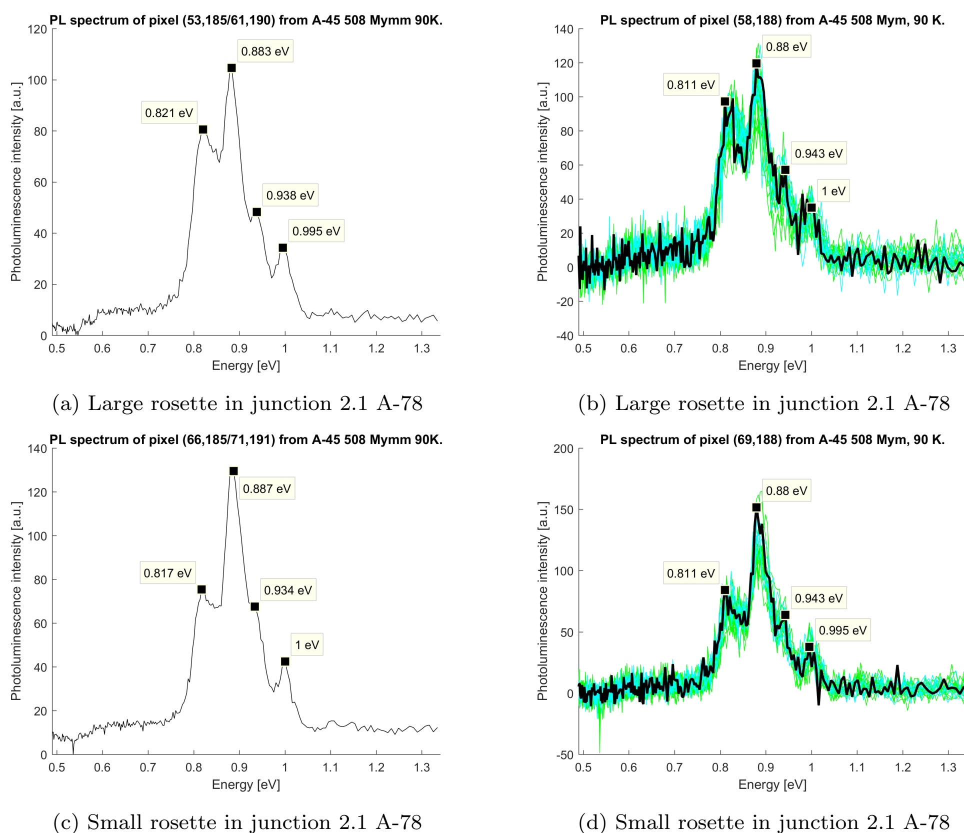

(a) Large rosette in junction 2.1 A-78

(b) Large rosette in junction 2.1 A-78

(c) Small rosette in junction 2.1 A-78

(d) Small rosette in junction 2.1 A-78

Figure 4.30: In seed junction 2.1 two rosette are evolving from A-108, figure a) showing a integrated spectrum over an area at the largest of the rosettes and a spectrum of center pixel spectrum at the largest in b). The same in c) and d), but for the smaller rosette. In the pixel plot black curve is the chosen pixel, cyan curve is the neighbour pixels and the green curve is all the pixels that are two pixels away.

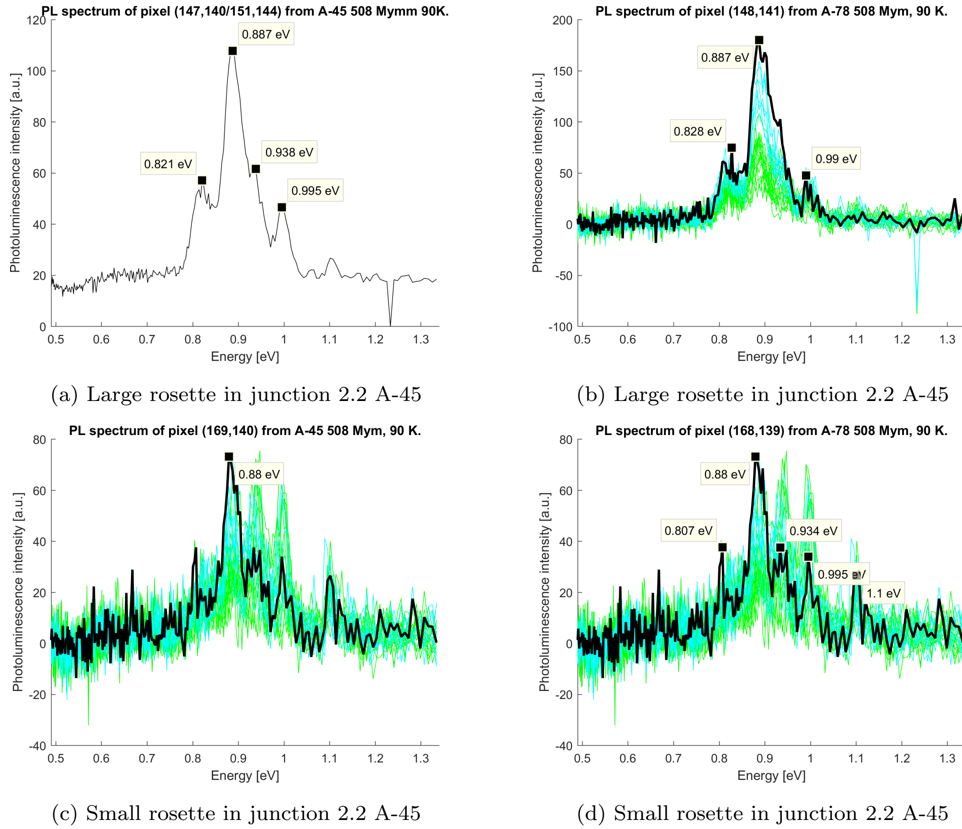

(a) Large rosette in junction 2.2 A-45

(b) Large rosette in junction 2.2 A-45

(c) Small rosette in junction 2.2 A-45

(d) Small rosette in junction 2.2 A-45

Figure 4.31: In seed junction 2.2 two rosette are evolving from A-108, figure a) showing a integrated spectrum over an area at the largest of the rosettes and a spectrum of center pixel spectrum at the largest in b). A spectrum of the center pixels in c) and d), covering the smaller rosette. In the pixel plot black curve is the chosen pixel, cyan curve is the neighbour pixels and the green curve is all the pixels that are two pixels away.

4.3.4 Section discussion

As seen in most of the integrated Matlab figures in this section, example 4.26, and 4.23. The emission signal graph drops to zero around 0.55 eV and then increases again. The signal should have stayed in around zero intensity until a emission signal was found. This can be related to a error in the preprocessing where background noise is subtracted by Matlab and this will be investigated further.

The D1 PL emission signal is found with a declining property through the ingot. D2 PL emission signal seems to be of the opposite trait, increasing with respect to elevated height. These two defect related signals have about the same concentration in A-108. This is discussed in section 4.1.2.

A signal with the energy of 0.846 eV is established in the 1.1, 1.2, 1.3 and possibly 2.1 junctions. This signal has been related to D5 defect in the work of Pizzini et al. [23], where it was suggested that the D5 PL emission signal can be related to dislocations decorated with oxygen. This signal is only present as the curve apex in the A-108 wafer when the D1 and D2

PL signals are close to each other in intensity. Based on this the 0.846 eV signal can be related to a superposition of D1 and D2 PL emission signal. A more thorough investigation is conducted in section 4.5.

In A-108 the PL emission signals of 1.3, 1.4 and 1.6 junction are given by figure 4.12 b) and c) and 4.13 f). The junctions are similar to each other with about equal D1 and D2 PL emission signals, however, in 1.6 the BB PL signal is lesser than the other two junctions. This can be related to the size of the gap, penetrateing melt and forming of mc-Si crystals. As seen in the work by Ekstrøm et al. [1], there is no void between the seed crystals, indicating that the melt has penetrated the junction. If mc-Si growth has occurred in 1.6 junction a D07 PL emission signal should be found here as well, however this signal is not found. An interesting fact is that junction 1.3 has a higher intensity of all D1-D4 PL emission signals than junction 1.6, even if the gap in this junction is 0.4 mm. This can be related to a axis tilt and misorientation angle discussed further in this chapter.

As mentioned by Ekstrøm et al. [1], rosettes did establish in junctions 2.1 and 2.2, caused by the weight of the silicon. Note that another rosette is mentioned located at in the junction 1.1, but the PL emission signal from that rosette has not been found in this experiment. At A-108, as seen in figure 4.15 a), the 2.1 rosette has been successful of trapping D1 related impurities and this corresponds well with the oxygen diffusion hypothesis. The minor rosette in figure 4.15 b) show some D2 PL signals. The rosettes attributes are comparable to the rest of the junction attributes with an increase in D2, D3 and D4 PL signals and a decrease in the D1 PL signal. In A-45, two rosettes are found in both 2.1 and 2.2 junctions.

At A-78 the new signal 0.904 eV is established in junctions 1.4 and 1.5, and also found in junctions 1.6 and 2.1 in the A-45 wafer. With a thorough examination, the signal was found throughout the A-45 wafer with a varing energy of ± 0.01 eV and will be discussed in section 4.5.

D3 and D4 PL emission signals have grown from nothing, into curves with segregated apexes in A-78 growing even further into the A-45 wafer. If D4 and D3 PL signals are related to iron impurities as stated by Lausch et al. [21], it is intuitive to think that the D4 and D3 will increase in intensity with elevated height. This topic have been discussed in section 4.1.2.

As established from the PL emission signal investigation, nine different junctions are seen. The PL signals from these junctions shows that each junction is different from each other. In junctions 1.2 and 1.5 the lifetime is high and BB PL signal are high, this can be related to the small misorientation angle of each junctions planes with $0.17°$ and $0.03°$, respectively, as given by Ekstrøm et al. [1]. Other than the rosettes forming in junction 2.2, which seems to lock impurities very well, this is also a calm junction with high-lifetime and BB PL emission. Here the X-axis misorientation angle is low, at $0.2°$.

Junction 1.3 and 1.6 should experience from a lot of dislocations. Ekstrøm et al. [1] mentions that 1.6 is the most chaotic junction of these two, however in PL emission it seems that junction 1.3 has more DRL. This is seen from figure 4.23 and 4.26. This contradicts the misorientation angle explanation, as discussed, to junctions 1.2 and 1.5, with the junction 1.3 at $0.56°$ misorientation angle and junction 1.6 with a $0.26°$ misorientation angle. An explanation can be that junction 1.3 has a much greater Z-axis misorientation than junction 1.6.

Junctions 1.1 and 1.4 have the same X-axis misorientation of $0.23°$ and $0.22°$, an interesting discovery from figure 4.21 and 4.24 is that the junction 1.1 have more DRL signals than 1.4 and a much lower BB PL emission signal. An explanation can be that junction 1.1 has a relatively high misorientation angle in both the X-axis and the Z-axis. The 1.4 junction on the other hand has a misorientation angle only in the Z-axis [1].

Junction 2.1 has a high misorientation angle of $0.55°$ in the Z-axis. While, the 2.3 junction has a low misorientation angle in Z-axis of $0.14°$, however the 2.3 junction have relatively high multiple misorientation angles from both X, Y, Z- axis, creating a chaotic junction, as seen in

figure 4.29. Junction 2.3 is by far the worst DRL related junction as seen by both the score images in section 4.2.1 and the loading plot seen in figure 4.29.

As been discussed junction 2.3 have misorientation angles in X, Y, Z-axis and then seen as a chaotic junction. An interesting observation is that junction 1.6 has the same characteristics. This contradicts the axis explanation, however, this can be explained by the gap itself in junction 1.6. The gap is so wide that the misorientation angle can be without effect. It can be that the main reason for DRL signals in this junction is the mc-Si solidification process itself. The explaniation why the multple misorientation angles are a problem can be explained in its simplicity, that there are more room for impurities to occupy.

At the end it must be mentioned that comparing the A-45 wafer junctions to the junctions used in the work of Ekstrøm et al. [1] can be incorrect. The reason is that the junctions have been studied in different heights, nonetheless, the reasoning should hold because of the small height differences and the difference in each junction property.

4.4 D07 PL emission signal

4.4.1 Establishment of rogue crystals from the crucible wall and D07 PL emission signal

The D07 PL emission signal has been mentioned before in a paper by Lausch et al. [21]. In this paper the D07 PL emission signal was found in small, distinguished and concentrated areas in a mc-Si solar cell. Since mono-like silicon wafers had not been investigated with SPL combined with MCR before, any results would be interesting. Even without the slightest idea of what to expect, the result still came with surprise. As seen in figure 4.32 a), the score image from Matlab show the establishment of three different and distinguished D07 PL emission signals.

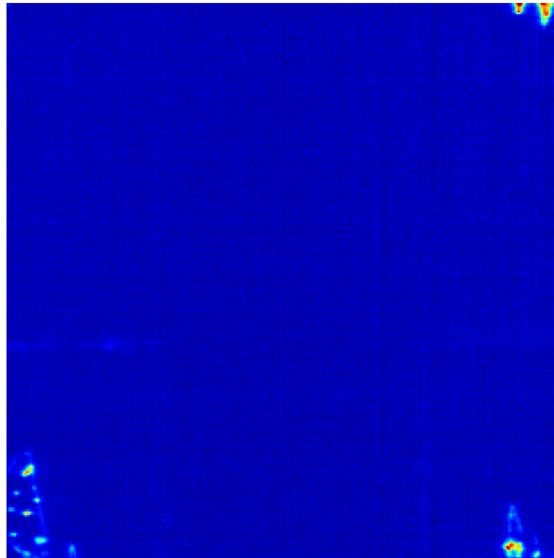

Figure 4.32: Score image from Matlab of the D07 related PL emission signal from rogue crystals 1 lower left corner.

In figure 4.33 a), a 75 μm score image of crystal 1 has been magnified 200 %.

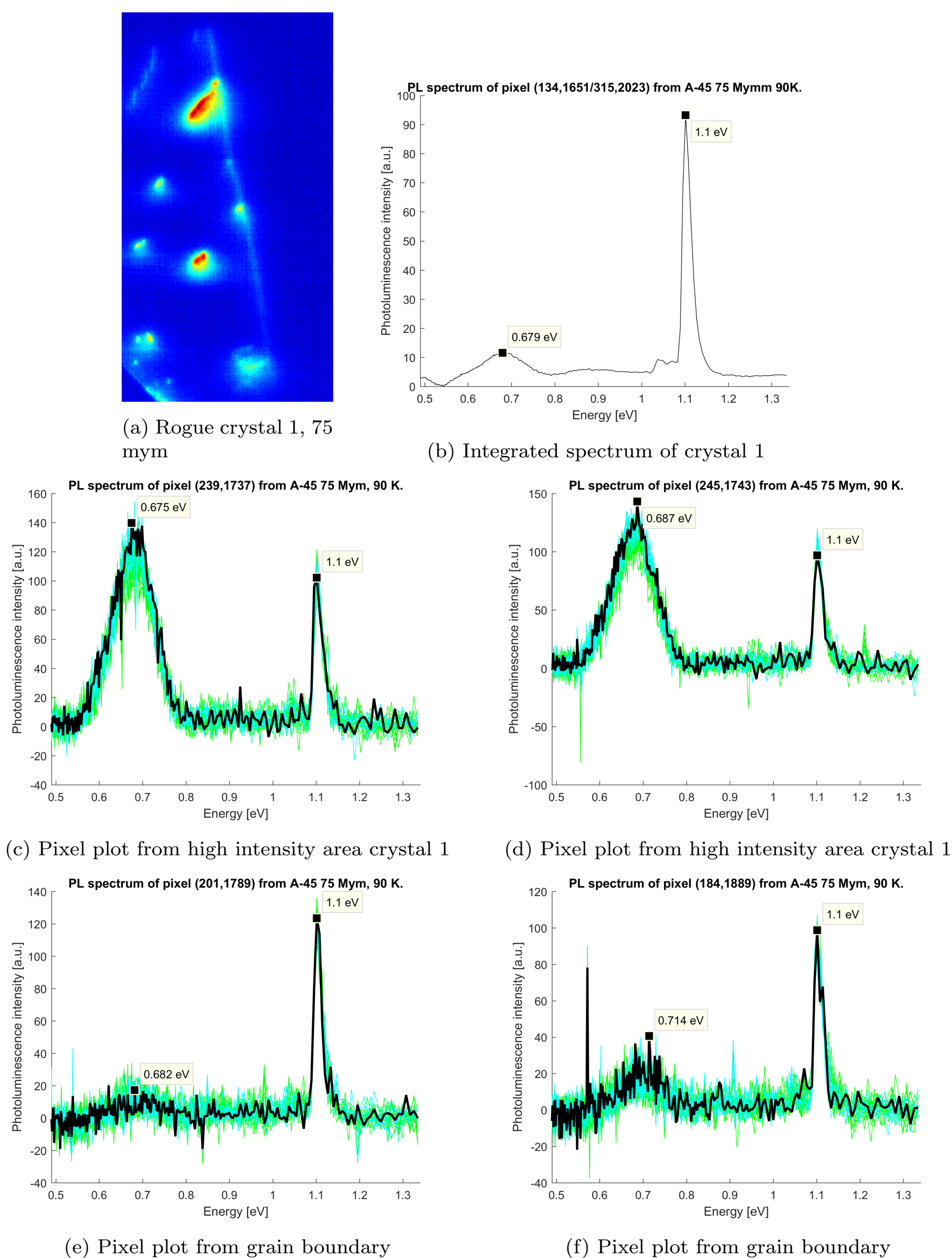

(a) Rogue crystal 1, 75 mym

(b) Integrated spectrum of crystal 1

(c) Pixel plot from high intensity area crystal 1

(d) Pixel plot from high intensity area crystal 1

(e) Pixel plot from grain boundary

(f) Pixel plot from grain boundary

Figure 4.33: Score image of rogue crystal 1 in a), integrated area plot in b), pixel plots of high intensity areas (red) in c) and d), pixel plot of the grain boundary between high intensity areas in e) and f).

At this pixel size, examining of crystal 1, 2 and 3 are relative easy. In 4.33 b), an integrated area plot is shown. The plot reveals no other defects than the D07 emission signal with apex at 0.679 eV, the BB PL signal and a BB phonon replica at 1.05 eV. Investigating the crystal further with pixel plots shown in figure 4.33 c) and d) taken from high intensity areas in red reveals again only the D07 PL emission signal. As seen in figure 4.33 a), the high intensity areas in red are surrounded by a low intensity grain boundaries. Pixel plot investigation from this area is seen in figure 4.33 e) and f), where only small amounts of D07 is found. The investigation have established no other DRL signals in rogue crystal 1.

The second rogue crystal is shown in figure 4.34 a) with the 75 μm resolution image magnified 200 %. This crystal does not have the same shape as crystal 1, with a more concentrated main structure and small fingers extends out of the crystal. Figure 4.34 b) is an area plot and shows as crystal 1 a clear D07 and BB PL emission signal, the phonon replica is seen at the BB ankle as well.

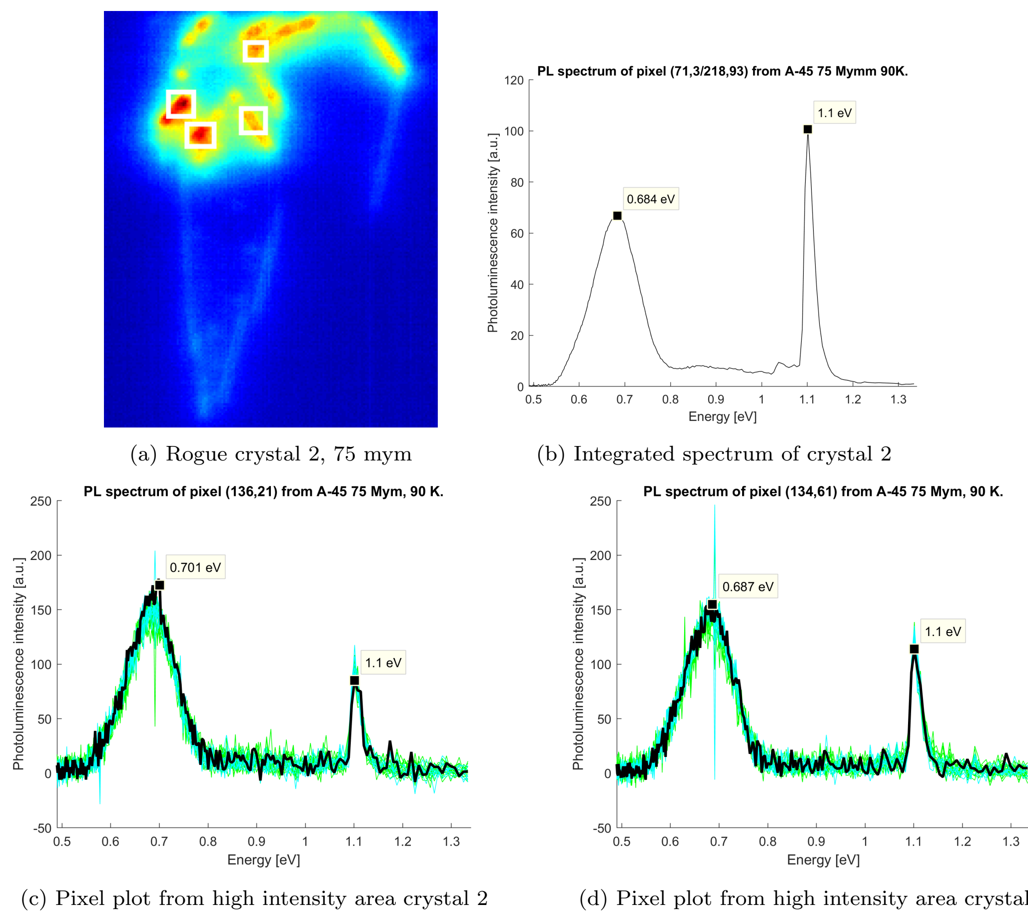

(a) Rogue crystal 2, 75 mym

(b) Integrated spectrum of crystal 2

(c) Pixel plot from high intensity area crystal 2

(d) Pixel plot from high intensity area crystal 2

Figure 4.34: Score image of rogue crystal 2 in a), integrated area (high intensity in red) plot in b), pixel plots of high intensity areas in c) and d).

In figure 4.34 c) and d) pixel plots are done to check the different fingers shown in figure 4.34 a), as seen before, only a high intensity D07 PL emission signal is found. As the rogue crystal 1, this crystal carries only a single D07 PL signal.

The last rogue crystal is located in the upper right corner of figure 4.32 a). The rogue crystal 3 seems to grow straight in from the side of the ingot with a penetration point into the wafer higher up than crystal 1 and 2. A score image of the crystal with 75 μm resolution is shown in figure 4.35 a), magnified 200 %.

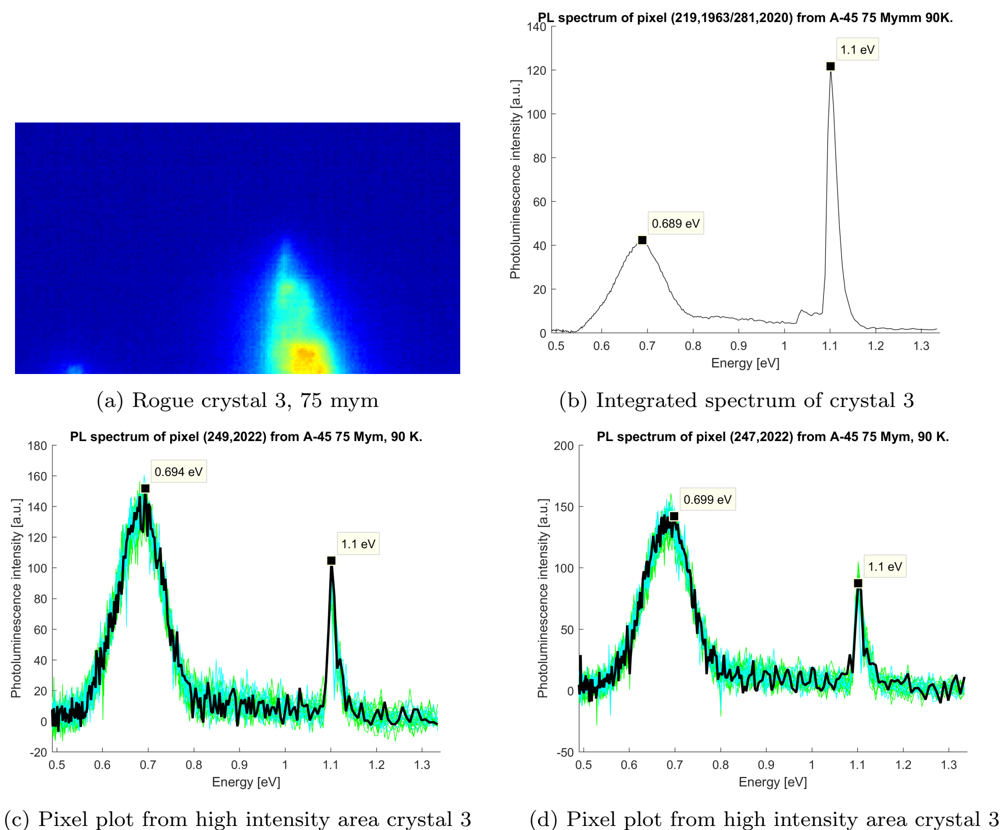

(a) Rogue crystal 3, 75 mym

(b) Integrated spectrum of crystal 3

(c) Pixel plot from high intensity area crystal 3

(d) Pixel plot from high intensity area crystal 3

Figure 4.35: Score image of rogue crystal 3 in a), integrated area plot in b), pixel plots of high intensity areas in c) and d).

Crystal 3 has been investigated by an area plot and pixel plot as the other rogue crystals, this is shown in figure 4.35 b), c) and d). The results confirm our assumptions and that crystal 3 has a clear, distinct D07 PL emission signal with no other DRL present. A slightly difference in the D07 signal is noticed.

The experiment has found no traces of other DRL signals in these rogue crystals, however, work by Ekstøm et al. [1] the possibility of rogue poly-crystals inside the 1.6 seed junction is discussed. The investigation from the A-45 1.6 junction is shown in figure 4.36 a) and b). Two pixel plots from different locations in the junction is shown. The results are shown from the figure is D1 and D2 related PL emission signals in both pixels, in one of the pixel some D3/D4 PL signals are also present. The graph shows only inconclusive and oscillating measurements in the 0.7 eV area.

Finally the A-108 needs to be examined in the 1.6 seed junction, an area plot integrated over the wafer except the rogue crystal seen in the score image from 4.4 a) is shown in figure 4.37 where small amounts of D1 and D2 PL signals are present. Checking the PL emission signal with

a pixel plot taken inside the 1.6 junction gap reveals D1 and D2 PL signals, no D07 PL signal is found.

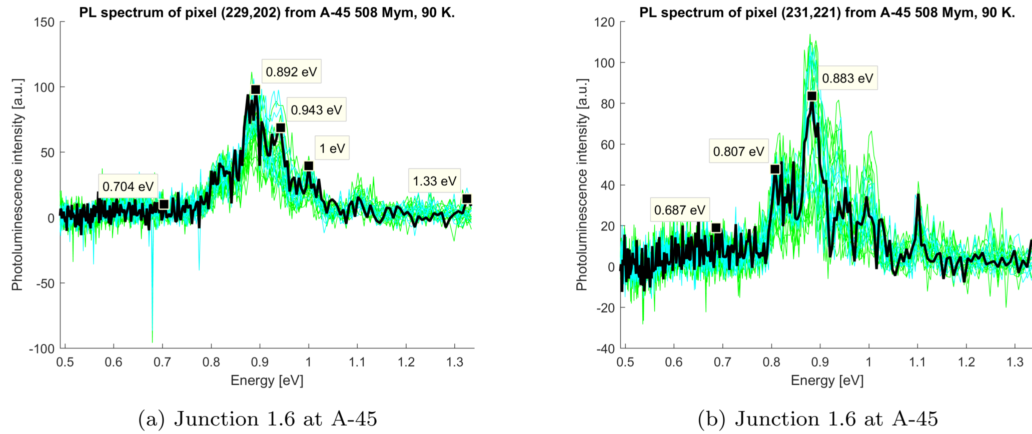

(a) Junction 1.6 at A-45

(b) Junction 1.6 at A-45

Figure 4.36: Pixel plots taken inside seed junction 1.6 searching for D07 of wafer A-45.

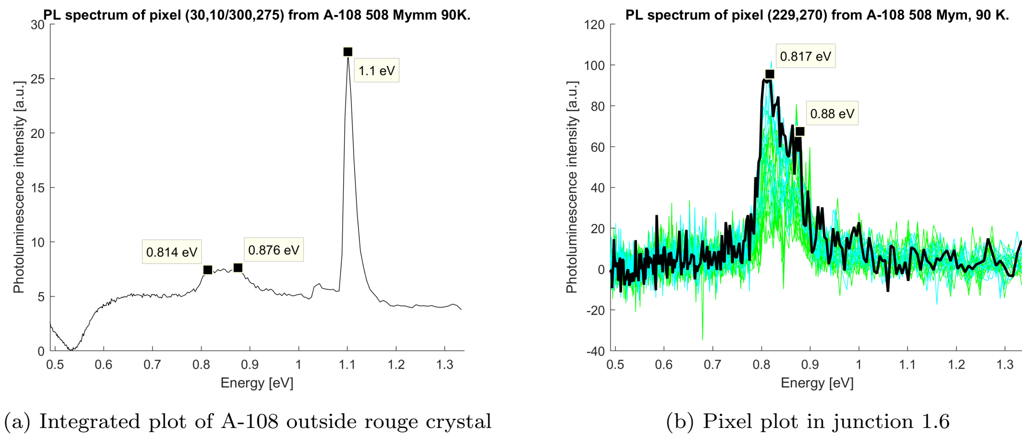

(a) Integrated plot of A-108 outside rouge crystal

(b) Pixel plot in junction 1.6

Figure 4.37: Integrated area plot of A-108 in a) and pixel plots taken inside seed junction 1.6 searching for D07 of wafer A-108 b).

A fourth rogue crystal penetrating the main wafer ingot from one side, as seen weakly in the bottom right corner in figure 4.38 a). The crystal has different characteristics then the other rogue crystals. Given by figure 4.38 b), multiple emission signals are found. Investing the rogue crystal further found that the D07 PL emission signal seems to be established in the crystal also. In figure 4.38 c), different weak emission signals with one pixel peaks are shown. It is difficult to extract a conclusion from this figure, however, it seems to support multiple signals.

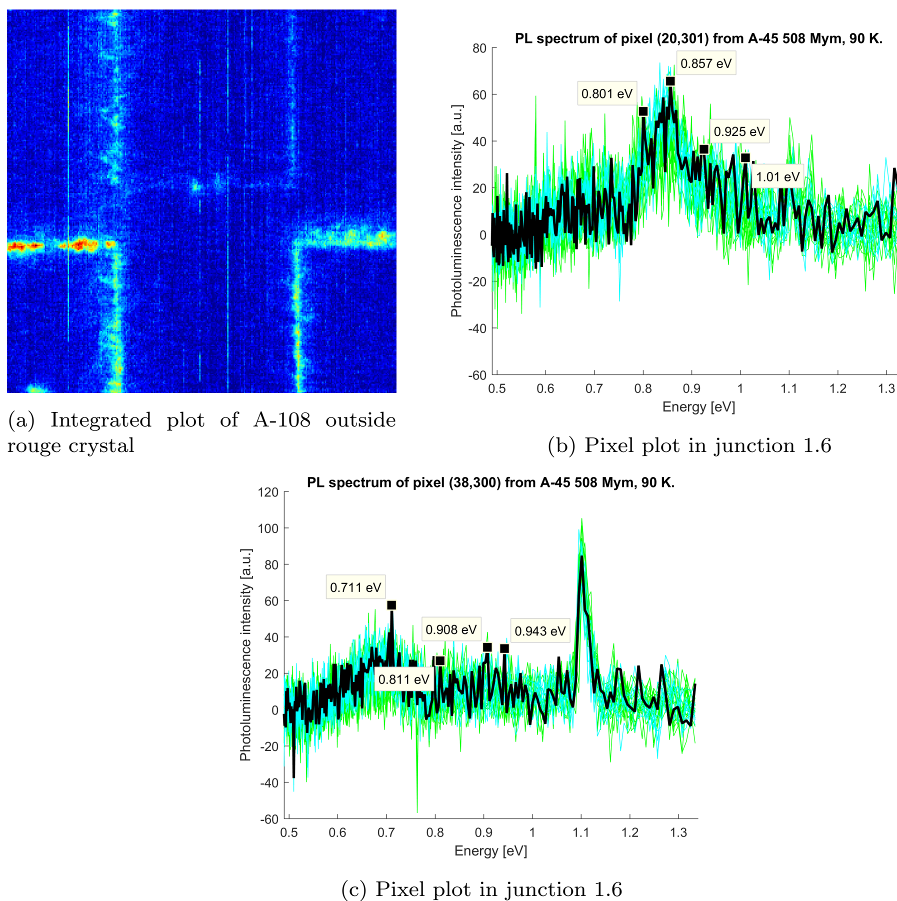

(a) Integrated plot of A-108 outside rouge crystal

(b) Pixel plot in junction 1.6

(c) Pixel plot in junction 1.6

Figure 4.38: Integrated area plot of A-108 in a) and pixel plots taken inside seed junction 1.6 searching for D07 of wafer A-108 b).

4.4.2 Section discussion

The PL emission signal with the energy of around 0.7 eV is an interesting signal to say at least. In the work by Lausch et al. [21] this signal was mentioned and found in small and segregated positions. In this experiment the D07 signal is found in three rogue crystals as a main emission signal, and in one as one of multiple signals. All of these rogue crystals seem to enter the main silicon crystal from the crucible wall. This can be related to the twinning's spoken of in the work by Ekstrøm et al. [1]. A paper still in press by Mehl et al., it is discussed the possibility D07 in p-type wafer to be related to interstitial iron (Fe_i) based on the work done by Graff [20]. In this paper electrical proporties of interstitial iron (Fe_i) creates a trap state of $E_T \approx E_V = 0.4 \pm 0.05$ eV. As mentioned before in section 4.3.4 the metallic impurities are readily available in the furnace. If iron precipitates would occure it is intuitive to think that Fe would be captured and locked in the dislocations forming within the rogue multicrystalline silicon.

A thing to debate is the idea that the D07 PL signal originates from (Fe_i) alone, or can the orientation of the grain boundaries be a part as well. Twinnings is known to grow in $\{111\}$ direction, they are the reflection of the Si crystal itself [1]. If the parasitic crystals forming on the crucible wall have grain boundaries with a higher dislocation number, Σ than the twinnings,

and are more activ, the D07 PL emission signal can be related to those crystals.

An interesting fact occurs when investigating the 1.6 seed junction thoroughly. Different mechanisms influencing the generation of dislocations in junction 1.6, was discussed in the work by Ekstrøm et al. [1]. It can be speculated in which degree this gap is big enough for producing rogue crystals, however, the D07 PL signal is not found in here or any other place at this junction in any of the wafers.

4.5 D5 and D09 PL emission signals

A PL emission signal of 0.904±0.01 eV has been found. The signal was seen in multiple MCR analysis, often in the A-45 wafer. The signal was at first thought of as a wave superposition of the D2 and D3 PL emission signals. That view was rejected after a closer examination of the junctions with the MCR analysing method. Pursuing the D09 PL emission signal with Matlab both with area plots and single pixel plots resulted in a number of D09 discoveries. In each junction a D09 signal was found as given by the figure 4.39.

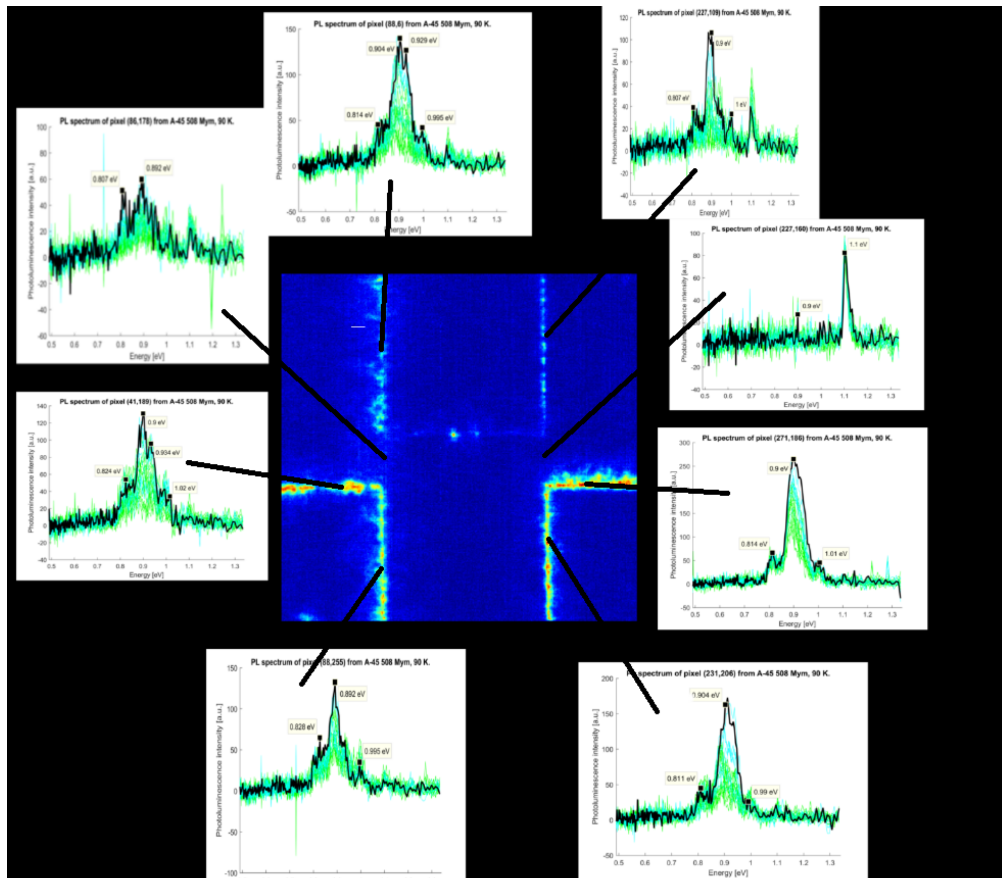

Figure 4.39: D09 signal and junctions in the A-45 wafer.

In figure 4.40 the D09 signal is extracted from the raw hyperspectral image. The signal seems to evolve from a D2 PL emission signal in A-108, to 0.887 eV signal in A-78, and in A-45 the

signal is at 0.896 eV. Note that this is one signal, in one pixel, at one junction. However, the rest of the investigation seem to confirm the results from 4.40.

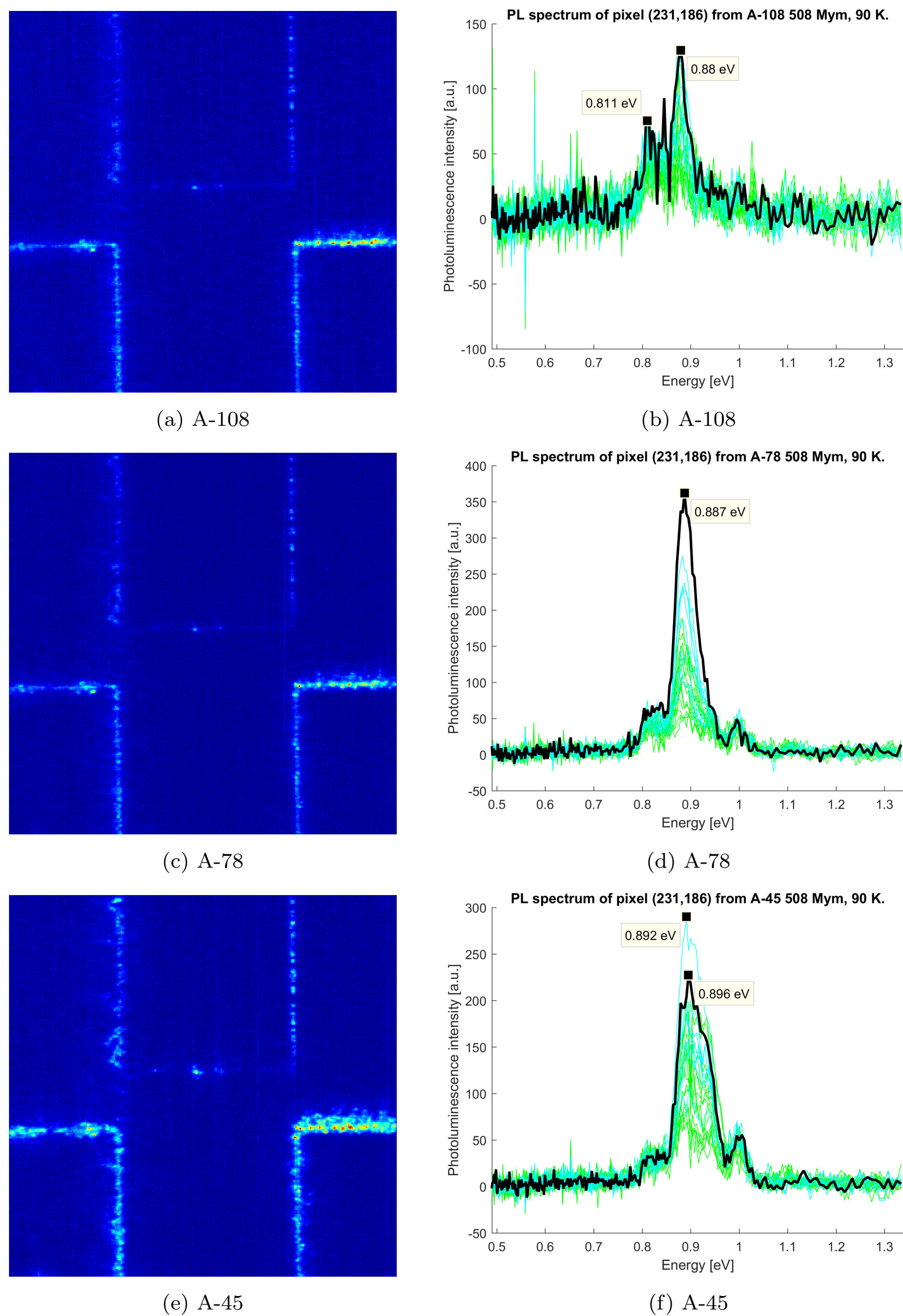

(a) A-108 (b) A-108

(c) A-78 (d) A-78

(e) A-45 (f) A-45

Figure 4.40: D09 PL emission signal evolving through the ingot.

The method to find D09 was to use MCR to find the PL emission signal component. Then

Matlab to integration over a pixel area, and the single pixel code. The same metod was used to search for the D5 component as given in figure 4.41.

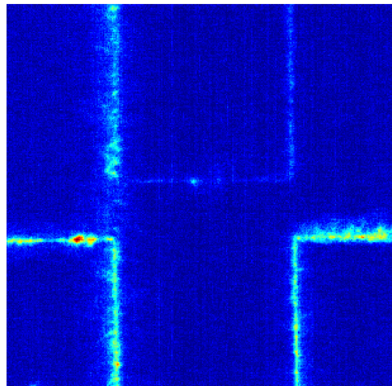

(a) A-108

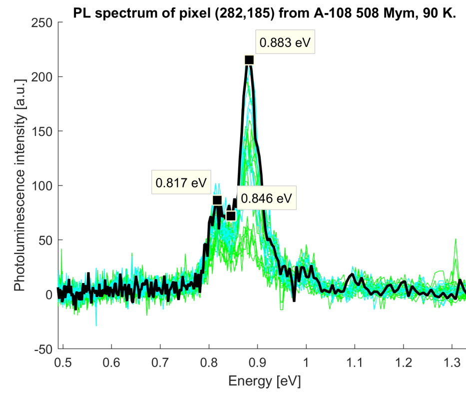

(b) A-108

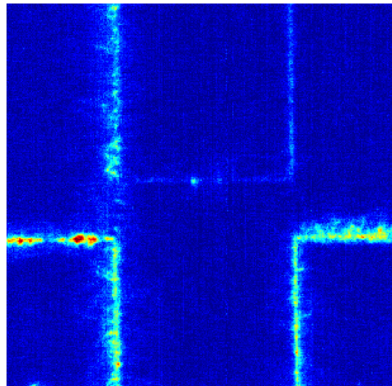

(c) A-78

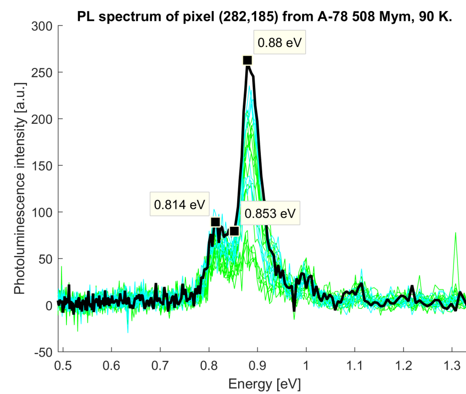

(d) A-78

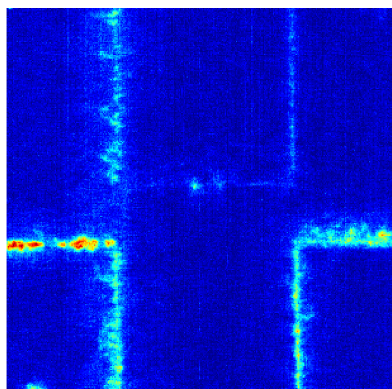

(e) A-45

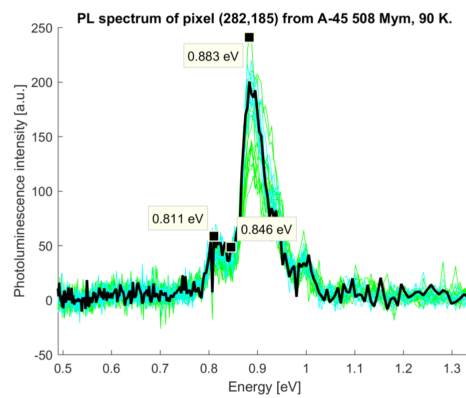

(f) A-45

Figure 4.41: D5 PL emission signal evolving through the ingot.

A remark has to be made, it seems that the D09 signal needs some time to manifest and it

was found most of all in the A-45 wafer. After some trial and error around a given junction the D09 signal seemed to be found with stronger intensity closer to the centre of the seed junction than just a few pixels away. As long as the seed junction center pixel is known the chance of finding D09 was great. In one junction on the other hand this did not apply. In seed junction 1.6 at the A-45 wafer the D09 PL emission signal had shifted from the centre line in the other vertical junctions 1.4 and 1.5. The signal was found one or two pixels away, this can be explained by the 1.6 mm gap in the junction.

Investigation of the D5 emission signal was conducted as the D09 emission signal. This emission signal is found as a shoulder of the much stronger D2 or D09 emission signal. The investigation has not found the signal as one peaked emission signal.

4.5.1 Section discussion

As the wafers were checked a signal of 0.904±0.01 eV was found in junction 1.4 in the wafer A-78. First the signal was taken for an artefact. When the MCR was used on a cropped image of the junctions alone the signal was found in more then one pixel. Investigating each junctions at more single pixels gave more secure results. The signal seemed to be located in the center or near the center pixel in most of the junctions. An exception was found when investigating the 1.6 junction, there the 0.9 eV signal shifted two or three pixels from the center. This can be related to the 1.6 mm gap introduced to the junction when seed crystals were placed.

It seems this signal is found at the location where two seed crystals lay against each other. It can be explained by silicon melt that solidify from both seed crystals. When these two different oriented grain boundaries layers grow into each other the signal occur. If the emission signal originates from impurity atoms, or from the dislocation itself, or from both is unknown and need further investigation. It is interesting that the signal has its strongest intensity in the center pixel of nearly each junction. Note, that this signal have not been debated before in the literature. This is also the first time SPL with MCR algorithm is used on a mono-like silicon wafer. It can be the mono-like attribute itself that is the reason behind this signal.

As for the D5 signal it is found as a shoulder of the D2 or D09 PL emission signal. It seems to loose intensity with increased height, like the D1 PL emission signal. It is stated by Pizzini et al. [23] that this two signal can be related to oxygen. Both signals should have the same behavior throughout the ingot. The results seem to confirm this.

4.6 Error found in MCR and laser intensity

4.6.1 Laser intensity

Throughout the experiment, difference in laser intensity was observed. One side of the wafer image has a higher intensity than the other side of the same image. A new experiment was done to see if the other side has the same intensity when illuminated by the laser. This was conducted by a 180 degrees rotation of the wafer, this action illuminated the other side by the same intensity. The result of the intensity difference are shown in figure 4.42.

The implications of this is that results from small, not illuminated areas will loose its information. The need of a exact laser is imperative for a excellent result in a research field like the SHR PL emission signal investigation.

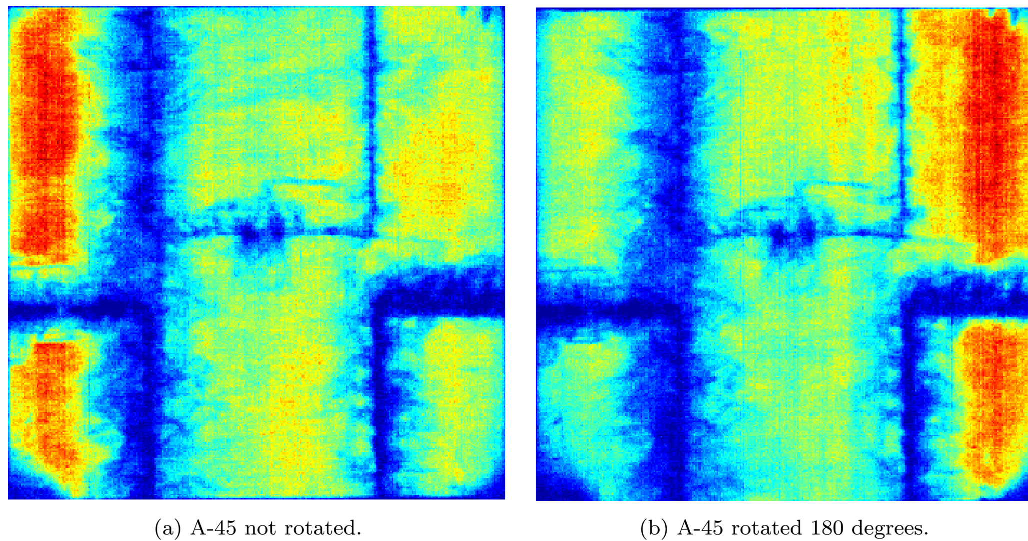

(a) A-45 not rotated. (b) A-45 rotated 180 degrees.

Figure 4.42: Intensity of A-45 wafer before rotation at a), A-45 wafer rotated 180 degrees in b).

4.6.2 Vacancy in MCR score image

When the laboratory part of the experiment was finished, the MCR algorithm was used to extract components in the raw image. After interesting areas were found, Matlab was used to extract even more information from the image. Under an investigation of the 2.3 junction MCR presented a score components with a particularly interesting attribute. D1 and D2 PL emission signals were found concentrated and near the center of the junction, while D3 and D4 were more scattered and diffuse as shown in figure 4.43. After some debate in the research group and closer investigation with Matlab this result was confirmed as a MCR error. While Matlab single pixel plot revealed often that DRL signals from D1-D4 are found in a single pixel, MCR did not manage to extract the information when the components were located in the same pixel.

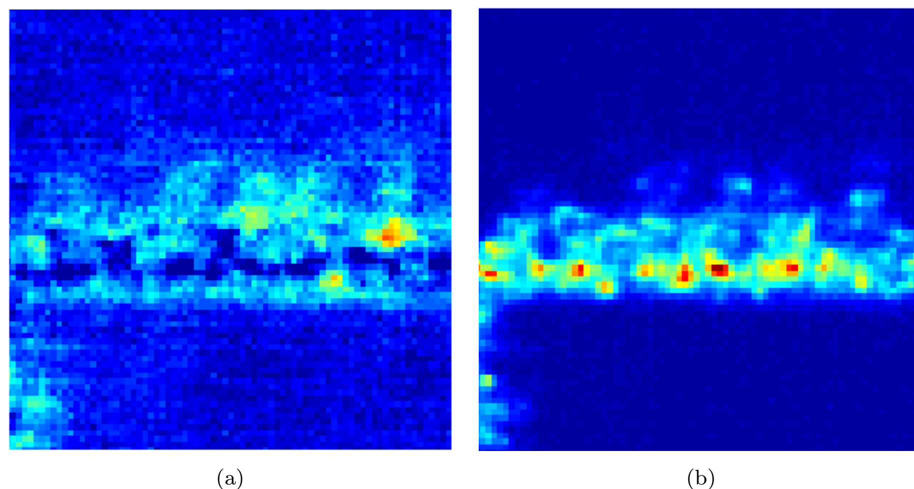

(a) (b)

Figure 4.43: In a) the D3/D4 PL emission signal is found, in b) the D1/D2 signal is found.

In the current work has not investigated why this error has occurred, further investigations are needed.

Chapter 5

Conclusion

This thesis can report several discoveries investigating four "as cut" wafers from a seed assisted mono-like silicon ingot. The results have been found with the combined strength of Hyperspectral imaging, Multivariate curve resolution and Matlab. Using MCR with 17 components, clear spectra of the interesting photoluminescence emission signals were found. The known D1-D4 PL emission signals were all found inside the seed junctions in each wafer, except the D07 PL emission signal. This PL signal was only found in the parasitic crystals growing in from the crucible wall to the main mono-like crystal.

In the near bottom wafer A-108, defect and band to band emission signals are weak and can be related to dead zones and a gathering of impurities. Near the top of the ingot, wafer A-45 was found with lower band to band intensity than its neighbour wafer. An explanation of this can be the dislocation active parasitic crystals are growing into the main wafer ingot. These parasitic crystals are suggested to have dislocations with interstitial iron (Fe_i) impurities.

The D1, D2 and D5 PL emission signals are suggested to be related to dislocation clusters with oxygen precipitates.

Only D1 and D2 PL emission signals have been found in the in A-108 wafer, except in junction 2.3. Here all D1-D4 PL emission signals are discovered. Why the 2.3 junction is so chaotic in the near bottom wafer needs to be studied further.

The D1 PL emission signal was found to be the defect related signal with clearly the highest intensity at the A-108 wafer. On the other hand, with increasing height the D1 PL emission signal is diminishing. An explanation can be that the D1 PL signal is related to oxygen that diffuses from the Czochralski crystal seeds at the bottom of the crucible into the seed junctions. As the oxygen gathers at the bottom of the ingot the PL signal will diminish with increased elevation. A tail of D1 component has been found located around 0.95 eV and 1.00 eV. In literature these PL emission signals has been related to hydrogen-Si bond in thin film silicon.

D2 PL emission signal is often related to as shoulder of the D1 PL signal. In this work it was established that the D2 PL emission signal is a single component and increases in intensity with an increasing elevation in the ingot. In some studies it is suggested that D2 PL emission signal is related to oxygen.with the D1 and D5 PL emission signals. Based on the oxygen segregation coefficient it is difficult to relate D2 PL emission signal to oxygen, and it seems to contredict the oxygen theory.

A signal denoted D5 in the literature is found in the seed junctions. This signal has been suggested to be a part of the D1 PL emission band with relations to dislocations with oxygen precipitates. The investigation can confirm the presence of the PL signal and when found it seems to be a shoulder of the D2 or the new D09 PL emission signal.

The D3/D4 PL emission signal are established in all wafers. In A-108 the discovery of D3/D4 PL emission signals are unique to the 2.3 seed junction. The growth of D3/D4 PL emission signals through the ingot with increasing height are clear and indisputable. This can be explained by the metallic impurities readily present in the crucible wall and can increase its precipitation with increased height. Based on this the D4 PL emission signal can be explained by the interaction of iron-boron in a FeB complex and the D3 can be related to the phonon replica.

The VID3 PL emission signal has not been found during the investigation.

Parasitic crystals are found to grow into the main ingot on multiple locations, each crystal has its own characteristic shape and appearance. Three crystals are found with one single defect related PL emission signal, this signal is the D07 signal. The fourth parasitic crystal contains multiple defect PL emission signals. This experiment has not investigated the grain boundaries and the issue should be examined further.

Comparing this investigation with the work done by Ekstrøm et al. [1] has discovered some similarities. A correlation of the low-lifetime areas and defect PL emission areas above the seed crystal junctions seems to be clear. The work by Ekstrøm et al. [1] discovered different tilt and misorientations in each seed junction. The investigation concluded that misorientations in the seed crystal junctions produced tilt around one or several axis had a major part in the bulk lifetime. The investigation preformed at the NMBU has established that low misorientation angle around the X-axis seems to produce none or weak defect related PL emission signals. Misorientation around the Z-axis seems to produce more defect related luminescence and misorientation around multiple axis seems to create chaotic junctions with high defect related luminescence. The explanation can be the number of vacancies ready for impurities are higher in multiple axis tilts than one axis tilt.

A PL emission signal of 0.9 ± 0.01 eV has been found in multiple seed junctions. The signal has been called the "D09" PL emission signal. It seems to be mainly centered of each seed junctions, further investigation on the topic should be conducted.

The conclusion is that the combined strength of SPL and MCR as a method to investigate mono-like has been used with success. The known D1-D4, D5 and D07 PL emission signals was found alongside a new PL emission signal at 0.9 ± 0.01 eV. The PL emission signals are not clearer than found in mc-Si wafers, however, the D07 signal has been found separated from the rest of the other DRL signals and this can be a helpful in further experiments. The different PL emission signals are found to vary a greatly throughout the ingot and logic answers can be made to explain the results based on known literature. Hyperspectral imaging and Multivariate curve resolution can strengthen and contribute to an increased quality of seed assisted mono-like wafers.

Chapter 6

Suggestions for future work

The outcome of this work could have been enhanced if more time was avalible, for instance a thesis conducted over two semesters. The results should have been compared to complementary research to gain a strong foundation to conduct future investigations directed at seed assited growth of mono-like silicon ingots.

The different mono crystal seed junctions show individual characteristics related to dislocations and PL emission signals. By combing this investigation with dislocation mapping and Electron backscatter diffraction (EBSD) each junction characteristics could be unravelled as much as possible. These complementary techniques could also be done on the parasitic crystals penetrating the main ingot. Since the results have discovered two types of penetrating crystals, one type with D07 PL emission signal only and one type with multiple defect related PL signals. A thorough examining of the grain boundaries and dislocation directions would be interesting.

Fourier transform infrared spectroscopy (FTIR) was meant to be a part of this investigation. I would be interesting to conduct an investigation on the oxygen levels in the seed junctions based on the diminishing D1 PL emission signal and the increasing D2 PL emission signal. If it is so that the Czochralski crystal seeds have high amounts of oxygen impurities, an investigation on difference in oxygen of the A-108 and A-45 wafer should be conducted.

Being a quantitative thesis, implementation of the mathematical theory related to the results have not been done. Implement mathematical theory would be useful of the general research of solar physics group at NMBU. The MCR equation is used to extract spectral components of the raw image, with no other. Mathematical theory was needed to explain the recombination and diffusion theory.

A problem occurred during the experimental part. The laser used in illuminating each wafer varies in intensity. The specimen is illuminated with higher intensity on one side. The laser should be either calibrated or switched to another more stable laser.

Another error is the integration code used by Matlab. It the background noise is not properly subtracted, the implication is that it is difficult to tell if the weak signals are present or not.

Bibliography

[1] KE Ekstrøm, G Stokkan, R Søndenå, H Dalaker, T Lehmann, L Arnberg, and M Di Sabatino. Structure and dislocation development in mono-like silicon. *physica status solidi (a)*, 212(10):2278–2288, 2015.

[2] C Julian Chen. *Physics of solar energy*. John Wiley & Sons, 2011.

[3] Dominique Sarti and Roland Einhaus. Silicon feedstock for the multi-crystalline photovoltaic industry. *Solar energy materials and solar cells*, 72(1):27–40, 2002.

[4] George Fiegl and Walter Torbet. Continuous replenishment of molten semiconductor in a czochralski-process, single-crystal-growing furnace, August 4 1981. US Patent 4,282,184.

[5] TF Li, HC Huang, HW Tsai, A Lan, C Chuck, and CW Lan. An enhanced cooling design in directional solidification for high quality multi-crystalline solar silicon. *Journal of Crystal Growth*, 340(1):202–208, 2012.

[6] Tatsuo Saga. Advances in crystalline silicon solar cell technology for industrial mass production. *NPG Asia Materials*, 2(3):96–102, 2010.

[7] Kozo Fujiwara, Yoshikazu Obinata, Toru Ujihara, Noritaka Usami, Gen Sazaki, and Kazuo Nakajima. Grain growth behaviors of polycrystalline silicon during melt growth processes. *Journal of crystal growth*, 266(4):441–448, 2004.

[8] NA Drozdov, AA Patrin, and VD Tkachev. Recombination radiation on dislocations in silicon. *Jetp Lett*, 23(11), 1976.

[9] Xin Gu, Xuegong Yu, Kuanxin Guo, Lin Chen, Dong Wang, and Deren Yang. Seed-assisted cast quasi-single crystalline silicon for photovoltaic application: towards high efficiency and low cost silicon solar cells. *Solar Energy Materials and Solar Cells*, 101:95–101, 2012.

[10] I Burud, AS Flø, and E Olsen. On the origin of inter band gap radiative emission in crystalline silicon. *AIP Advances*, 2(4):042135, 2012.

[11] A Flø, I Burud, K Kvaal, R Søndenå, and E Olsen. Distribution of radiative crystal imperfections through a silicon ingot. *Aip Advances*, 3(11):112120, 2013.

[12] K Jäger, O Isabella, A Smets, RACMM van Swaaij, and M Zeman. Solar energy. fundamentals, technology, and systems. *Delft University of Technology*, 2014.

[13] LJ Geerligs. *mc-Si: relation between ingot quality and cell efficiency.* Energy research Centre of the Netherlands ECN, 2002.

[14] Ismael Guerrero, Vicente Parra, Teresa Carballo, Andrés Black, Miguel Miranda, David Cancillo, Benito Moralejo, Juan Jiménez, Jean-François Lelièvre, and Carlos Cañizo. About the origin of low wafer performance and crystal defect generation on seed-cast growth of industrial mono-like silicon ingots. *Progress in Photovoltaics: Research and Applications*, 22(8):923–932, 2014.

[15] Re N Hall. Electron-hole recombination in germanium. *Physical Review*, 87(2):387, 1952.

[16] We Shockley and WT Read Jr. Statistics of the recombinations of holes and electrons. *Physical review*, 87(5):835, 1952.

[17] Charles Kittel. *Introduction to solid state physics.* Wiley, 2005.

[18] Peter Pichler. *Intrinsic point defects, impurities, and their diffusion in silicon.* Springer Science & Business Media, 2012.

[19] Daniel Macdonald, LJ Geerligs, et al. Recombination activity of interstitial iron and other transition metal point defects in p-and n-type crystalline silicon. 2004.

[20] Klaus Graff. *Metal impurities in silicon-device fabrication*, volume 24. Springer Science & Business Media, 2013.

[21] D Lausch, T Mehl, K Petter, A Svarstad Flø, I Burud, and E Olsen. Classification of crystal defects in multicrystalline silicon solar cells and wafer using spectrally and spatially resolved photoluminescence. *Journal of Applied Physics*, 119(5):054501, 2016.

[22] R Sauer, J Weber, J Stolz, ER Weber, K-H Küsters, and H Alexander. Dislocation-related photoluminescence in silicon. *Applied Physics A*, 36(1):1–13, 1985.

[23] S Pizzini, M Acciarri, E Leoni, and A Le Donne. About the d 1 and d 2 dislocation luminescence and its correlation with oxygen segregation. *physica status solidi(b)*, 222(1):141–150, 2000.

[24] Michio Tajima, Yasuaki Iwata, Futoshi Okayama, Hiroyuki Toyota, Hisashi Onodera, and Takashi Sekiguchi. Deep-level photoluminescence due to dislocations and oxygen precipitates in multicrystalline si. *Journal of Applied Physics*, 111(11):113523, 2012.

[25] D Lausch, K Petter, R Bakowskie, J Bauer, O Breitenstein, and C Hagendorf. Classification and investigation of recombination-active defect structures in multicrystalline silicon solar cells. In *Proc. 27th Eur. Photovoltaic Solar Energy Conf. Exhib*, pages 723–728, 2012.

[26] V Kveder, M Kittler, and W Schröter. Recombination activity of contaminated dislocations in silicon: A model describing electron-beam-induced current contrast behavior. *Physical Review B*, 63(11):115208, 2001.

[27] Vitaly V Kveder, EA Steinman, SA Shevchenko, and HG Grimmeiss. Dislocation-related electroluminescence at room temperature in plastically deformed silicon. *Physical Review B*, 51(16):10520, 1995.

[28] I Tarasov, S Ostapenko, C Haessler, and E-U Reisner. Spatially resolved defect diagnostics in multicrystalline silicon for solar cells. *Materials Science and Engineering: B*, 71(1):51–55, 2000.

[29] NEO. Hypex: What is hyper spectral imaging? visited 05.05.2016. `http://www.hyspex.no/hyperspectral_imaging/`, may 2016.

[30] Stuart Phinn, Chris Roelfsema, Arnold Dekker, Vittoro Brando, and Janet Anstee. Mapping seagrass species, cover and biomass in shallow waters: An assessment of satellite multi-spectral and airborne hyper-spectral imaging systems in moreton bay (australia). *Remote Sensing of Environment*, 112(8):3413–3425, 2008.

[31] Nahum Gat, Suresh Subramanian, Jacob Barhen, and Nikzad Toomarian. Spectral imaging applications: remote sensing, environmental monitoring, medicine, military operations, factory automation, and manufacturing. In *25th Annual AIPR Workshop on Emerging Applications of Computer Vision*, pages 63–77. International Society for Optics and Photonics, 1997.

[32] Lise L Randeberg, Janne-Lise Hegstad, Lukasz Paluchowski, Matija Milanič, and Brita S Pukstad. Hyperspectral characterization of an in vitro wound model. In *SPIE BiOS*, pages 892607–892607. International Society for Optics and Photonics, 2014.

[33] Joaquim Jaumot, Raimundo Gargallo, Anna de Juan, and Roma Tauler. A graphical user-friendly interface for mcr-als: a new tool for multivariate curve resolution in matlab. *Chemometrics and Intelligent Laboratory Systems*, 76(1):101–110, 2005.

[34] Xin Zhang and Romà Tauler. Application of multivariate curve resolution alternating least squares (mcr-als) to remote sensing hyperspectral imaging. *Analytica chimica acta*, 762:25–38, 2013.

[35] David M Haaland, Jerilyn A Timlin, Michael B Sinclair, Mark H Van Benthem, M Juanita Martinez, Anthony D Aragon, and Margaret Werner-Washburne. Multivariate curve resolution for hyperspectral image analysis: applications to microarray technology. In *Biomedical Optics 2003*, pages 55–66. International Society for Optics and Photonics, 2003.

[36] Torbjørn Mehl. Karakterisering av multikrystallinske solceller ved bruk av hyperspektral avbildning. 2014.

[37] Robert Hull. *Properties of crystalline silicon.* Number 20. IET, 1999.

[38] AU Savchouk, S Ostapenko, G Nowak, J Lagowski, and L Jastrzebski. Band-tail photoluminescence in polycrystalline silicon thin films. *Applied physics letters*, 67(1):82–84, 1995.

[39] Deepak A Ramappa and Worth B Henley. Diffusion of iron in silicon dioxide. *Journal of the Electrochemical Society*, 146(10):3773–3777, 1999.

[40] Tine Uberg Nærland, Lars Arnberg, and Arve Holt. Origin of the low carrier lifetime edge zone in multicrystalline pv silicon. *Progress in Photovoltaics: Research and Applications*, 17(5):289–296, 2009.

[41] AA Istratov, H Hieslmair, and ER Weber. Iron and its complexes in silicon. *Applied Physics A*, 69(1):13–44, 1999.

Appendix A

MCR loads with all 17 components, 20 components and 5 components

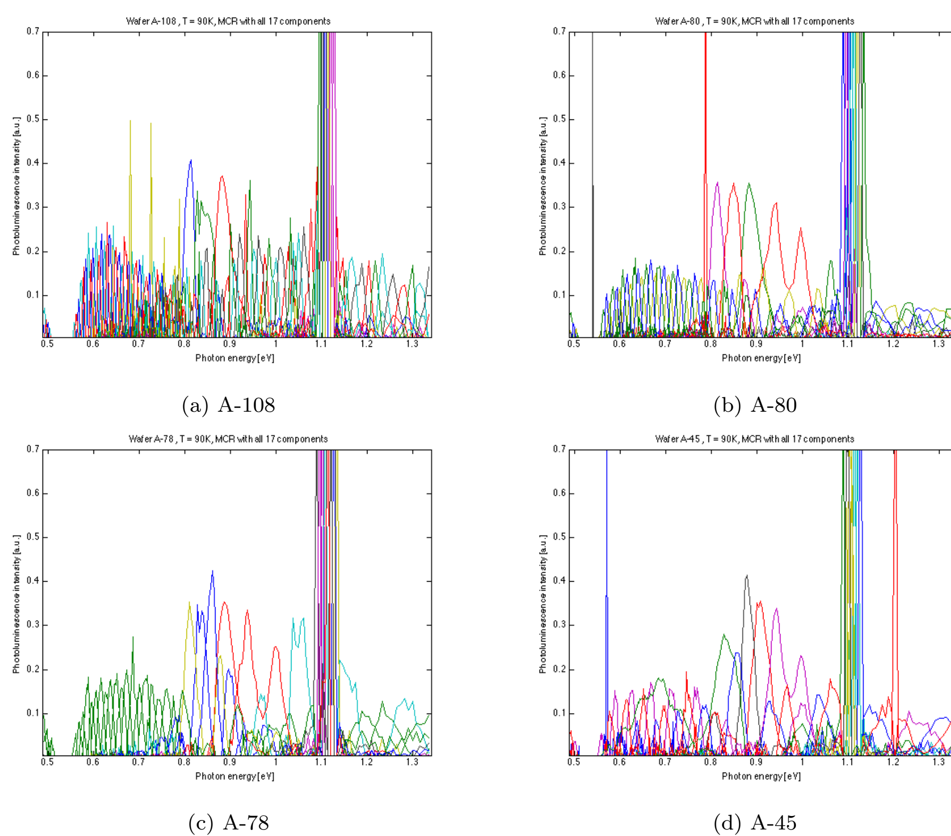

(a) A-108 (b) A-80

(c) A-78 (d) A-45

Figure A.1: All 17 components from MCR from the A-108 to A-45 wafer.

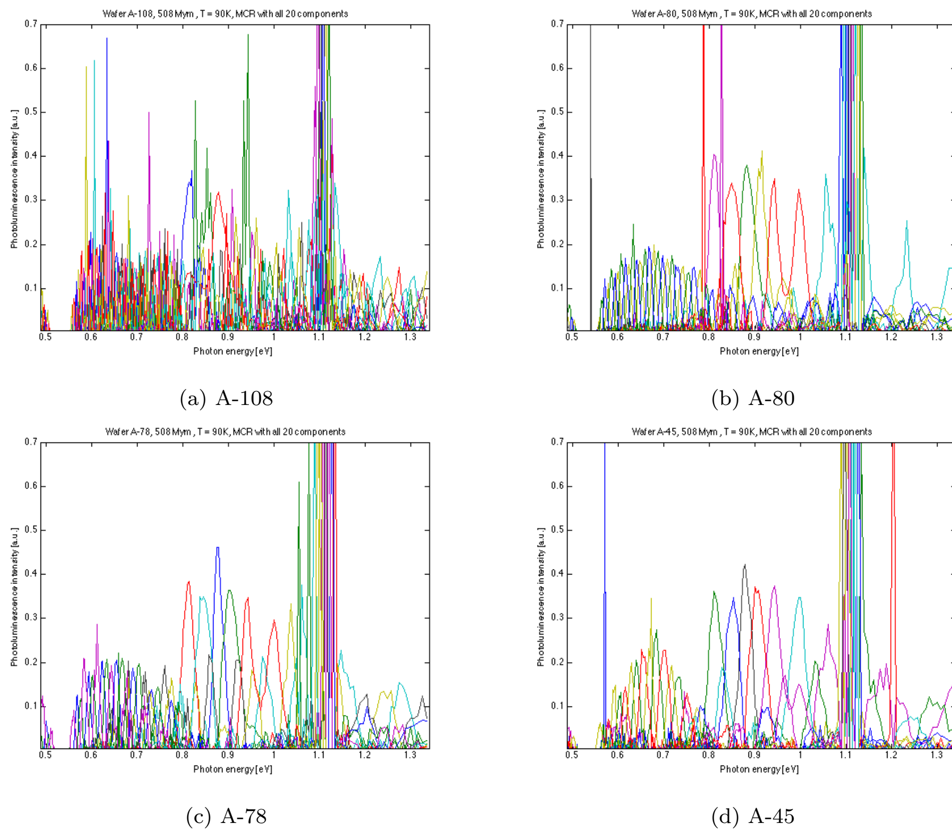

(a) A-108

(b) A-80

(c) A-78

(d) A-45

Figure A.2: All 20 components from MCR from the A-108 to A-45 wafer.

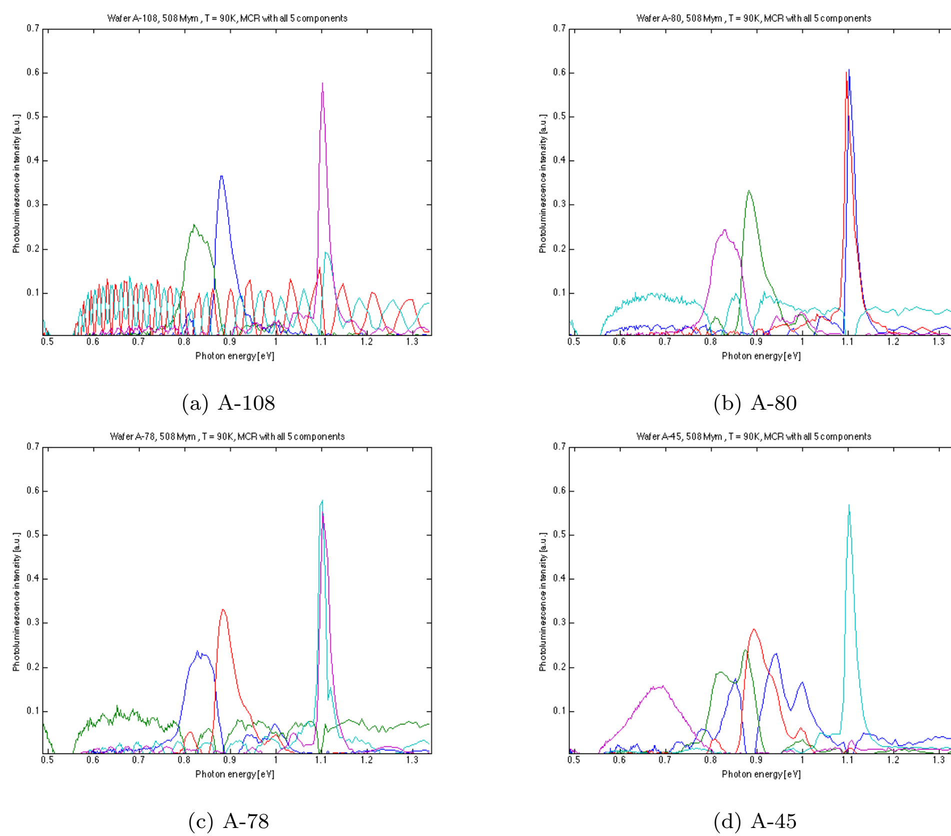

(a) A-108

(b) A-80

(c) A-78

(d) A-45

Figure A.3: All 5 components from MCR from the A-108 to A-45 wafer.

Appendix B

Translation from image spectrum to electronvolt

Table B.1: Spectrum to energy

Sensor	Energy [eV]	Sensor	Energy [eV]	Sensor	Energy [eV]
1	1,33444041	31	1,10787219	61	0,94737713
2	1,32539626	32	1,10164106	62	0,94283123
3	1,31647387	33	1,0954893	63	0,93832875
4	1,30767082	34	1,0893963	64	0,93386907
5	1,2989847	35	1,08338017	65	0,92944461
6	1,29041322	36	1,07742075	66	0,92506878
7	1,28196738	37	1,0715358	67	0,92073396
8	1,27361829	38	1,06570563	68	0,91643957
9	1,26537724	39	1,05994762	69	0,91219177
10	1,25724216	40	1,0542515	70	0,90797651
11	1,2492236	41	1,04861627	71	0,90380004
12	1,24129424	42	1,04303219	72	0,89966181
13	1,23347719	43	1,03751595	73	0,8955613
14	1,22574585	44	1,03205774	74	0,89150441
15	1,2181228	45	1,02665667	75	0,88747776
16	1,21058216	46	1,02131184	76	0,88349362
17	1,20314598	47	1,01602236	77	0,87953884
18	1,19580059	48	1,0107874	78	0,8756255
19	1,18853296	49	1,00561426	79	0,8717407
20	1,18136439	50	1,00048573	80	0,86789629
21	1,17428178	51	0,99540924	81	0,86407962
22	1,16728358	52	0,99038401	82	0,86030234
23	1,1603683	53	0,98541709	83	0,85655795
24	1,15353448	54	0,98049199	84	0,852846
25	1,14678068	55	0,97561588	85	0,84916027
26	1,1401055	56	0,97079563	86	0,84551203
27	1,13350758	57	0,96601525	87	0,841895
28	1,12698559	58	0,96128917	88	0,83830879
29	1,12053823	59	0,95660911	89	0,834753
30	1,11417422	60	0,95196708	90	0,83122724

Table B.2: Spectrum to energy

Sensor	Energy [eV]	Sensor	Energy [eV]	Sensor	Energy [eV]
91	0,82773667	121	0,73510885	151	0,66127372
92	0,82426982	122	0,73237754	152	0,65906971
93	0,82083188	123	0,72967074	153	0,65688034
94	0,8174225	124	0,72697962	154	0,65470547
95	0,81404668	125	0,7243125	155	0,65254495
96	0,81069332	126	0,72166489	156	0,65039865
97	0,80736747	127	0,71903656	157	0,6482698
98	0,80407402	128	0,71642731	158	0,64615148
99	0,80080215	129	0,71383692	159	0,64404696
100	0,79756193	130	0,7112652	160	0,64195943
101	0,79434783	131	0,70871194	161	0,63988209
102	0,79115449	132	0,70617695	162	0,63782142
103	0,78799172	133	0,70366003	163	0,63577073
104	0,78485414	134	0,70116098	164	0,63373642
105	0,78173651	135	0,69867963	165	0,63171187
106	0,77864845	136	0,69621577	166	0,62970341
107	0,77558469	137	0,69377311	167	0,62770768
108	0,77254494	138	0,69134368	168	0,6257214
109	0,76952893	139	0,6889312	169	0,62375079
110	0,76653638	140	0,68653931	170	0,62179256
111	0,76356701	141	0,68416019	171	0,61984658
112	0,76062056	142	0,68180125	172	0,61791275
113	0,75769675	143	0,67945852	173	0,61599094
114	0,75479994	144	0,67712814	174	0,61408105
115	0,75192063	145	0,67481736	175	0,61218297
116	0,74906321	146	0,6725223	176	0,61029659
117	0,74623191	147	0,67023917	177	0,60842179
118	0,74341748	148	0,66797509	178	0,60656145
119	0,74062419	149	0,66572626	179	0,6047095
120	0,73785621	150	0,66349252	180	0,60286882

Table B.3: Spectrum to energy

Sensor	Energy [eV]	Sensor	Energy [eV]	Sensor	Energy [eV]
181	0,60104223	211	0,55096984	241	0,50868858
182	0,59922378	212	0,54944624	242	0,50739165
183	0,59741917	213	0,54793104	243	0,50610131
184	0,59562254	214	0,54642418	244	0,50481958
185	0,59383953	215	0,54492558	245	0,50354227
186	0,59206434	216	0,54343518	246	0,50227142
187	0,59030254	217	0,54195291	247	0,50100899
188	0,58855119	218	0,5404787	248	0,49975087
189	0,58680742	219	0,53901249	249	0,49850106
190	0,58507672	220	0,53755422	250	0,49725749
191	0,5833562	221	0,53610381	251	0,49601812
192	0,58164577	222	0,53466352	252	0,49478689
193	0,57994533	223	0,53322865	253	0,49356175
194	0,57825481	224	0,53180374	254	0,49234267
195	0,57657412	225	0,53038416	255	0,49112765
196	0,57490317	226	0,52897214	256	0,48992055
197	0,57324188	227	0,52756986		
198	0,57159016	228	0,526175		
199	0,56995055	229	0,52478527		
200	0,56831772	230	0,52340507		
201	0,56669421	231	0,52203211		
202	0,56508253	232	0,52066415		
203	0,56347743	233	0,51930552		
204	0,56188142	234	0,51795396		
205	0,56029696	235	0,51660941		
206	0,5587189	236	0,51527183		
207	0,5571522	237	0,51394116		
208	0,55559426	238	0,51261734		
209	0,55404254	239	0,51130032		
210	0,55250192	240	0,50999006		

Appendix C

A-108 to A-45 score images with locked A-45 BB intensity

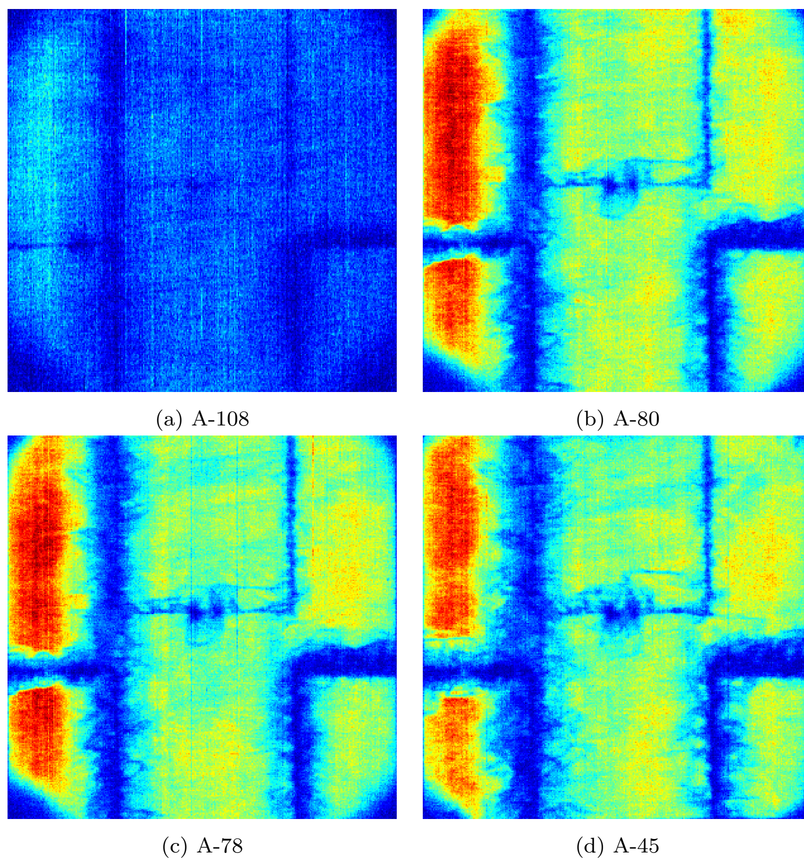

(a) A-108 (b) A-80

(c) A-78 (d) A-45

Figure C.1: BB PL emission signal from the mono-like silicon ingot of wafer A-108 to A-45 with equal intensities.

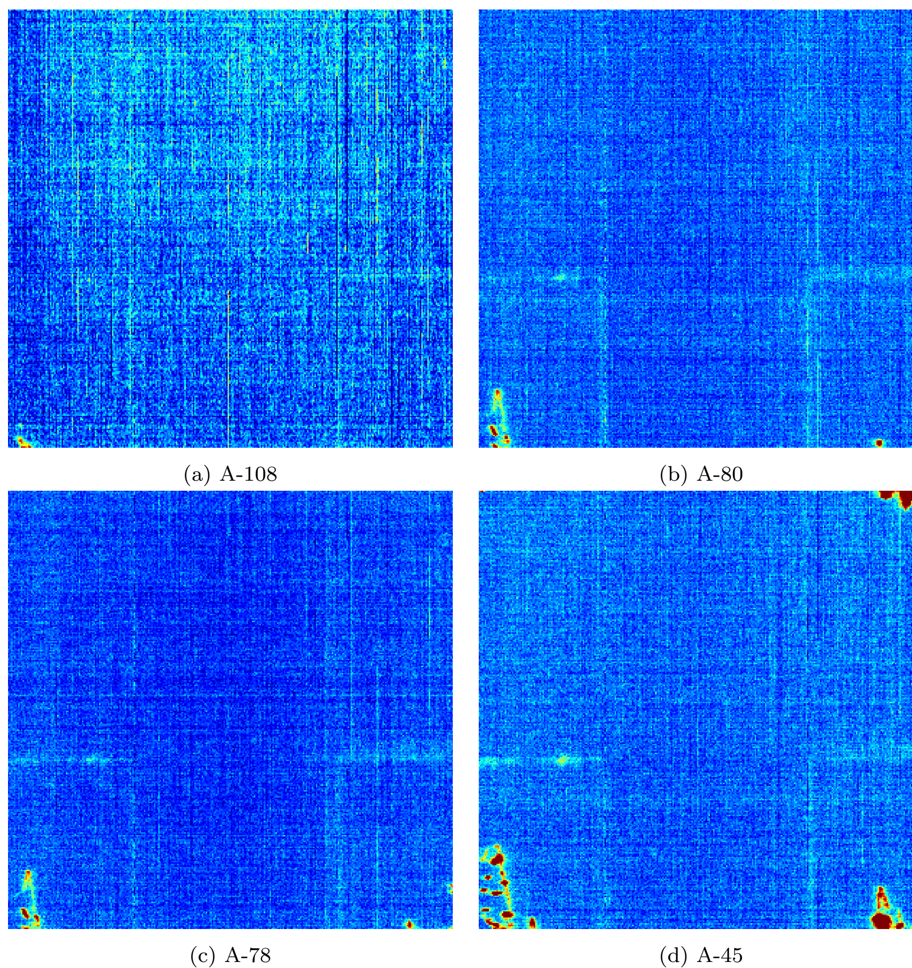

(a) A-108 (b) A-80

(c) A-78 (d) A-45

Figure C.2: D07 PL emission signal from the mono-like silicon ingot of wafer A-108 to A-45 with equal intensities.

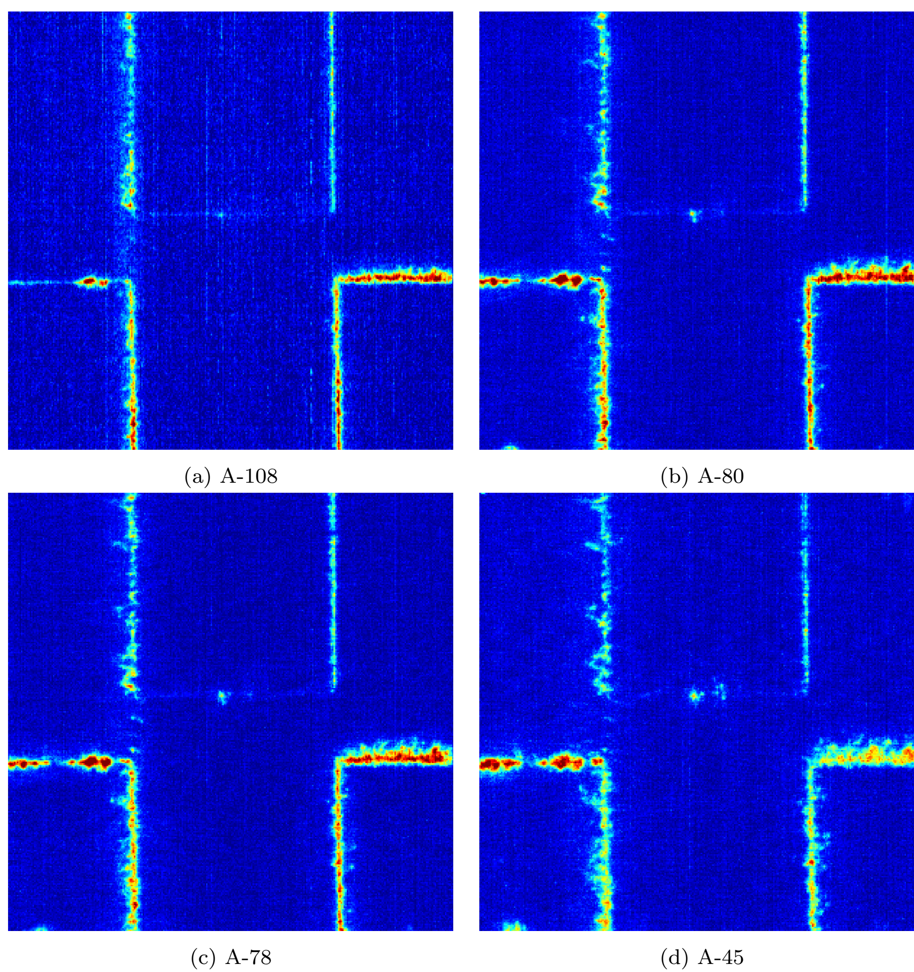

(a) A-108 (b) A-80

(c) A-78 (d) A-45

Figure C.3: D1 PL emission signal from the mono-like silicon ingot of wafer A-108 to A-45 with equal intensities.

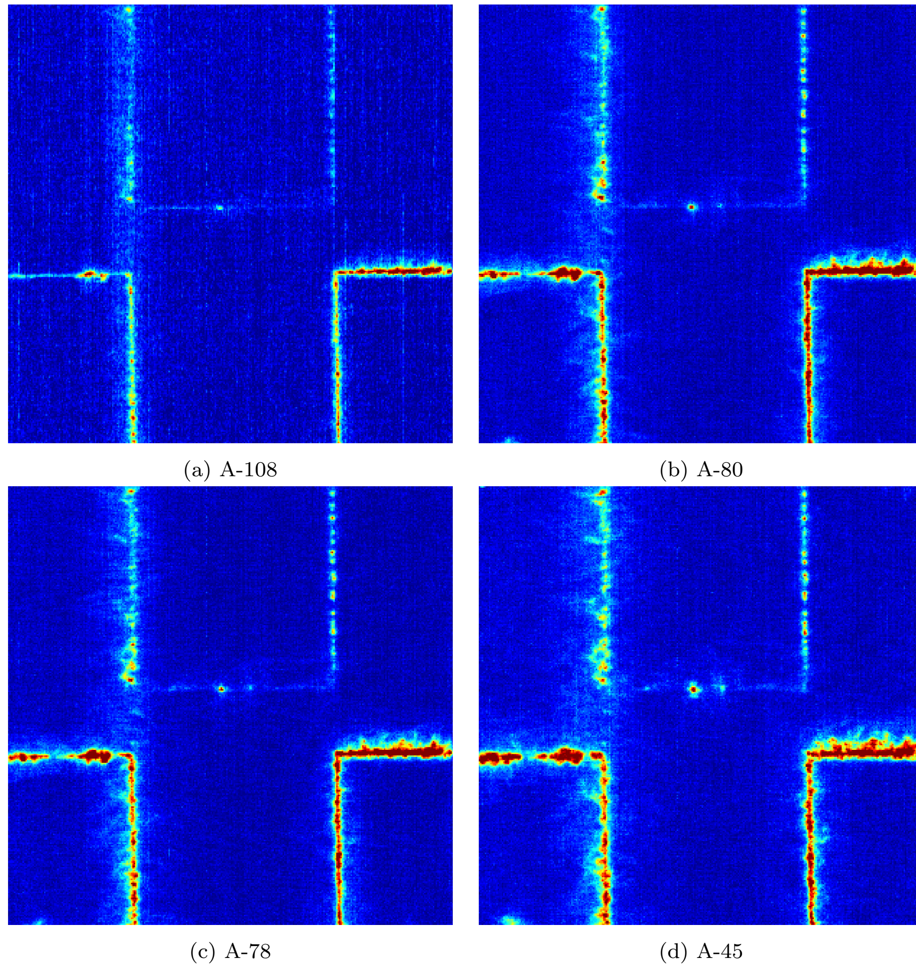

(a) A-108 (b) A-80

(c) A-78 (d) A-45

Figure C.4: D2 PL emission signal from the mono-like silicon ingot of wafer A-108 to A-45 with equal intensities.

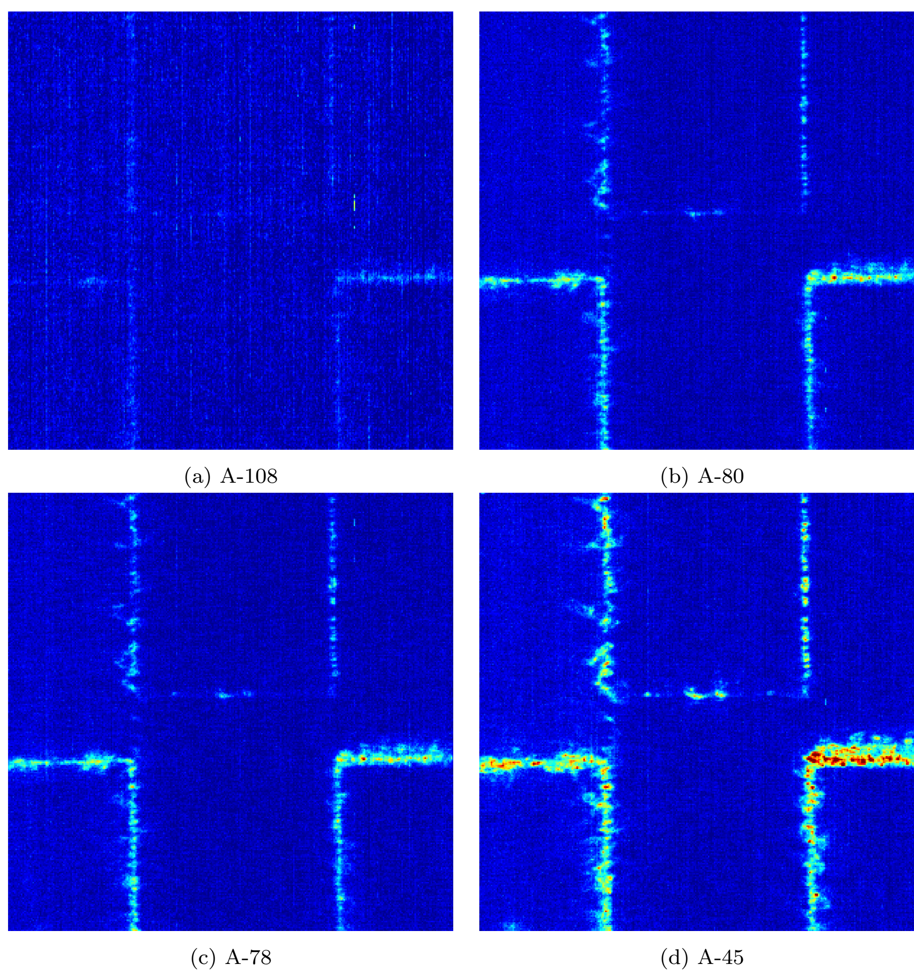

Figure C.5: D3 PL emission signal from the mono-like silicon ingot of wafer A-108 to A-45 with equal intensities.

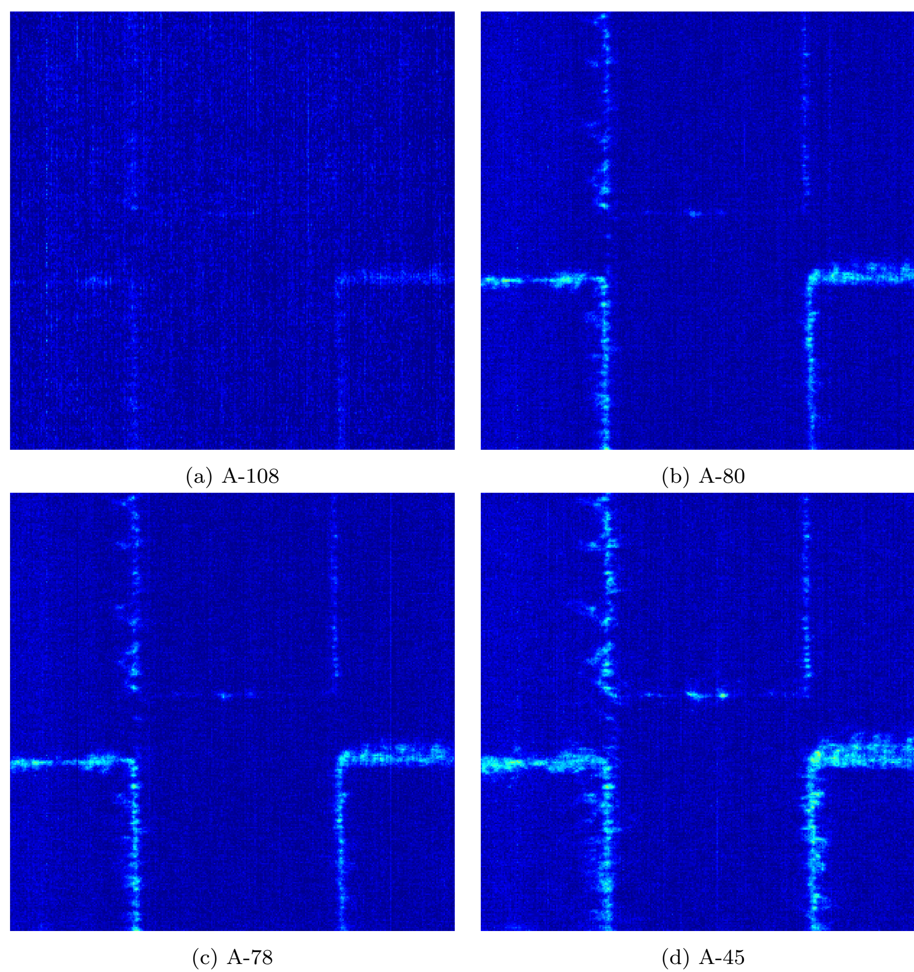

(a) A-108

(b) A-80

(c) A-78

(d) A-45

Figure C.6: D4 PL emission signal from the mono-like silicon ingot of wafer A-108 to A-45 with equal intensities.

Appendix D

Tables of DRL evolving through the mono-like silicon crystal and NTNU junction characteristics.

Table D.1: Detected PL emission signal develops in each seed junctions from wafer A-108 to wafer A-45.

Wafer junction	PL emission signal		
	D07 (about 0.7 eV)	D1 (0.812 eV)	D1.5 (about 0.84 eV)
A108 junction 1.1	Not found	Found	Not found
A108 junction 1.2	Not found	Possible	Not found
A108 junction 1.3	Not found	Found	Found
A108 junction 1.4	Not found	Found	Not found
A108 junction 1.5	Not found	Not found	Not found
A108 junction 1.6	Not found	Found	Found
A108 junction 2.1	Not found	Found	Possible
A108 junction 2.2	Not found	Found	Not found
A108 junction 2.3	Not found	Found	Found
A45 junction 1.1	Not found	Found	Found
A45 junction 1.2	Not found	Weak signal	Weak signal
A45 junction 1.3	Not found	Found	Found
A45 junction 1.4	Not found	Weak signal	Not found
A45 junction 1.5	Not found	Found	Not found
A45 junction 1.6	Not found	Found	Not found
A45 junction 2.1	Not found	Found	Found
A45 junction 2.2	Not found	Found	Not found
A45 junction 2.3	Not found	Found	Possible

Table D.2: Detected PL emission signal develops in each seed junctions from wafer A-108 to wafer A-45.

Wafer junction	PL emission signal			
	D2 (0.875 eV)	D2.5 (about 0.9 eV)	D3 (0.934 eV)	D4 (1.000 eV)
A108 junction 1.1	Not found	Not found	Not found	Not found
A108 junction 1.2	Possible	Possible	Not found	Not found
A108 junction 1.3	Found	Not found	Not found	Not found
A108 junction 1.4	Found	Not found	Not found	Not found
A108 junction 1.5	Not found	Not found	Not found	Not found
A108 junction 1.6	Found	Not found	Not found	Not found
A108 junction 2.1	Found	Not found	Not found	Not found
A108 junction 2.2	Found	Not found	Not found	Not found
A108 junction 2.3	Found	Found	Not found	Not found
A45 junction 1.1	Found	Found	Found	Found
A45 junction 1.2	Weak signal	Weak signal	Found	Found
A45 junction 1.3	Found	Found	Found	Found
A45 junction 1.4	Not found	Found	Found	Weak signal
A45 junction 1.5	Found	Not found	Not found	Found
A45 junction 1.6	Found	Found	Found	Found
A45 junction 2.1	Found	Found	Found	Found
A45 junction 2.2	Found	Found	Found	Found
A45 junction 2.3	Found	Found	Found	Found

Table D.3: Detected PL emission signal develops in each seed junctions from wafer A-108 to wafer A-45.

Wafer location	PL emission signal	
	D07 (about 0.7 eV)	D1-D4
A108 paracitic crystal from crucible wall	Found	Not found
A45 paracitic crystal from crucible wall	Found	Not found

Table D.4: A brief summary of Ekstroem and Stokkan paper [1] of each junction.

Junction number	Seed junction description
Junction 1.1	Boundary planes of 110/110. Mean width 3.7 mm, Laue measurements. Dislocations align in V-shape cascades with angle of 48 degrees to the growth direction . Dislocations arranging in ¡111¿ direction, elongating along a singel ¡111¿ direction. Large dislocation clusters, elongating with a 54.7 degree angle to the boundary plane. Stress dislocation rosette, tight junction, the weight of feedstock causes rosette.
Junction 1.2	Large dislocation clusters. Mean width 3.7 mm, Laue measurements. Low tilt value 0.17 degrees mainly around a single X-axis .
Junction 1.3	Large dislocation clusters . Mean width 6.8 mm, Laue measurements. 0.4 mm gap with linearity of SAGB, dislocation mainly related to misorientation between two seeds .
Junction 1.4	Boundary planes of 110/110. Mean width 1.0 mm, Laue measurements. Dislocations align in V-shape cascades with angle of 48 degrees to the growth direction . Very little dislocations, therefore no clear alignments, apart from the SAGB. Consists of Linear SAGB surrounded by small clusters. High misorientation, limited generation, tilt mainly around a single Z-axis. Straightness of SAGB, low complexity of the junction, enable low energy configurations along the boundary plane.
Junction 1.5	No dislocations at all. Mean width 0.0 mm, Laue measurements. Misorientation angle 0.03 degrees, very little low-lifetime areas.

Table D.5: A brief summary of Ekstroem and Stokkan paper [1] of each junction.

Junction 1.6	Large dislocation clusters, small misorientation. Mean width 1.6 mm, Laue measurements. 1.6 mm gap, chaotic, no void near crucible bottom. Considerable dislocation generation with several processes can be involved. Rogue crystals are most obvious with melt impingement.
Junction 2.1	Cluster do not elongate in the ¡111¿ direction more localized, maybe stress from precipitates or contact points. Mean width 7.2 mm, Laue measurements. Can generate additional dislocation, may interfere with delocalized dislocations, preventing alignment in periodic elongating arrays seen else where. Possible reason: relation to inital dislocation generation close to seed interface.
Junction 2.2	High misorientation, limited generation can be related to tilt around a single Z-axis. Mean width 0.5 mm, Laue measurements. Two rosettes in the seed interface and are most likely stress concentrators.
Junction 2.3	Clusters elongates in the ¡110¿ direction, but dislocations contained inside the clusters also elongate in the ¡111¿ direction. Mean width 9.1 mm, Laue measurements. ¡111¿ is not seen in verticalcut. Tilting around multiple axes.
Parasitic crystal	Twinning starting at 53 mm, 28 mm above seed interface Twinning occurs in the 111-facet plane

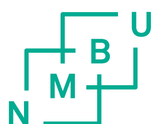

Norges miljø- og biovitenskapelig universitet
Noregs miljø- og biovitskapelege universitet
Norwegian University of Life Sciences

Postboks 5003
NO-1432 Ås
Norway